Block copolymer template-directed synthesis of well-ordered metallic nanostructures

Vuković, Ivana

Block Copolymer Template-Directed Synthesis of Well-Ordered Metallic Nanostructures

Ivana Vuković

Block Copolymer Template-Directed Synthesis of Well-Ordered Metallic Nanostructures

Ivana Vuković
PhD thesis
University of Groningen

Zernike Institute PhD thesis series 2013-05
ISSN: 1570-1530
ISBN (printed): 978-90-367-6022-5
ISBN (electronic): 978-90-367-6023-2

The reasearch presented in this thesis was performed in the Polymer Chemistry group of the Zernike Institute for Advanced Materials at the University of Groningen, The Netherlands. This work was funded by the Zernike Institute for Advanced Materials.

Cover design by Nikola Davidović
Printed by Wöhrmann Print Service B. V., Zutphen, the Netherlands

university of groningen / faculty of mathematics and natural sciences / zernike institute for advanced materials

RIJKSUNIVERSITEIT GRONINGEN

Block Copolymer Template-Directed Synthesis of Well-Ordered Metallic Nanostructures

Proefschrift

ter verkrijging van het doctoraat in de
Wiskunde en Natuurwetenschappen
aan de Rijksuniversiteit Groningen
op gezag van de
Rector Magnificus, dr. E. Sterken,
in het openbaar te verdedigen op
vrijdag 3 mei 2013
om 16.15 uur

door

Ivana Vuković

geboren op 31 december 1984
te Sarajevo, Bosnië en Herzegovina

Promotores:	Prof. dr. G. ten Brinke Prof. dr. K. Loos
Beoordelingscommissie:	Prof. dr. K. Jeremić Prof. dr. A. Böker Prof. dr. J. Ruokolainen

Contents

Chapter 1

Introduction

Part of this chapter was published in:
Polymer 2013, DOI: 10.1016/j.polymer.2013.03.013

1.1 Nanostructured materials

Nanostructured materials have, by definition, at least one dimension in the range from 1 to 100 nm. In comparison to macroscopic systems, nanomaterials have advanced properties arising from their nanoscale dimensions. Zero-dimensional (0D) nanostructures, nanoparticles, are widely applied in biology and medicine for probing of DNA structures,[1] MRI contrast enhancement,[2] tissue engineering,[3, 4], cancer therapy,[5] *etc.* Furthermore, they find application in food packaging and food safety,[6] as catalysts with enhanced performance,[7] for hydrogen storage,[8, 9] data storage,[10] *etc.* One-dimensional (1D) nanostructures (*e.g.*, wires, rods, tubes) are expected to play an important role as both interconnects and functional units in fabricating electronic, optoelectronic, electrochemical, and electromechanical nanodevices.[11, 12] Several methods have been used to fabricate 1D nanostructures including template-directed synthesis, self-assembly of 0D nanostructures, size reduction of 1D microstructures, electrospinning, and others. For example, Park *et al.* demonstrated the preparation of metallic line patterns using functional block copolymer templates.[13] Polystyrene-*block*-poly(2-vinylpyridine) (PS-*b*-P2VP) and poly(2-vinylpyridine)-*block*-poly(methyl methacrylate) (P2VP-*b*-PMMA) block copolymers were spin-coated onto Ag-coated silicon substrate and annealed under solvent vapor to achieve the desired surface morphology. Subsequently, porous block copolymers were obtained by either reconstruction of the P2VP block in ethanol or removal of the PMMA block by UV irradiation followed by rinsing with acetic acid. Finally, silver line patterns were generated using electrochemical etching or direct metal evaporation and lift-off processes. 2D nanostructures, like thin films, can be grown by vapor-phase (sputtering, chemical vapor deposition, atomic layer deposition, *etc.*) or liquid-phase deposition (electrochemical deposition, Langmuir–Blodgett films, self-assembled monolayers, *etc.*).[14-16] Finally, 3D nanostructures represent the ultimate form factor for a number of materials. However, their creation is a rather delicate task.[17] The available top-down approaches are extremely challenging: lithography techniques allow precise patterning, but can only be implemented in an inherently 2D manner, while the available 3D microscale techniques cannot be easily translated to the nanoscale. Currently, the attention is focused on bottom-up

approaches that are usually based on self-assembling processes often similar to those occurring in nature.
This thesis focuses on 3D nanostructured metals. The first chapter describes the established methods for metal nanofoam preparation and their limitations in terms of ordering at the nanoscale. Then, the application of block copolymers and block copolymer based systems as precursors to metallic nanostructures is discussed and the possibilities to overcome the aforementioned limitations with examples of block copolymer template-directed synthesis of metal nanofoams are suggested. The first chapter ends with an overview of the experimental work presented in this thesis and a brief outlook on the future trends in this research area.

1.2 Metal nanofoams: properties and preparation methods

A nanoporous metal foam is defined as a three-dimensional structure comprised of interconnected metallic features with a porosity greater than 50 vol % and in which sub-micron pores significantly contribute to the specific surface area of the foam.[18] Metal nanofoams have, on the one hand, properties characteristic of metals such as electrical and thermal conductivity, catalytic activity and ductility/malleability whilst on the other hand also displays properties characteristic of nanostructured materials such as high surface area, ultralow density and high strength-to-weight ratio. Due to this unique combination of properties, metal nanofoams appear as candidates for a number of technological applications. Several examples are described in the following paragraphs.
Hydrogen is an environmentally friendly energy carrier and its storage is one of the key challenges in the hydrogen economy. It can be stored as pressurized gas, cryogenic liquid or solid fuel as a combination with other materials such as metal hydrides. Due to safety reasons, metal hydrides are the preferable option for hydrogen storage and it has been demonstrated that in comparison to bulk material, nanostructured metals significantly improve the reaction kinetics, reduce the enthalpy of metal hydrides formation, lower the hydrogen absorption and release temperatures.[19-21] Nanoporous metals and their derivates can also be employed for the production of novel 3D-structured batteries. Open porous networks and thin ligaments enable fast diffusion of ions into and out of electrodes, thus, creating fast discharging and recharging batteries.[22] Due to the size-effect-enhanced catalytic properties, nanostructured metals, such as nickel, could be a low-cost substitution for precious-metal catalysts.[18] Furthermore, literature reports the tunability of the

physical properties of nanoporous metals through an applied voltage.[23, 24] Injection of the surface charges into a porous metal nanofoam enhances the surface stresses leading to its expansion or contraction. Actuation properties of metallic nanofoams have been proven experimentally.[25] A bilayer foil consisting of solid and nanoporous gold layer was immersed in an aqueous electrolyte and the electrochemical potential varied. The nanoporous layer expanded or shrunk while the solid one maintained its original dimensions, and thus, bilayer foil bent with the tip displacement of several millimeters. The observed strain was orders of magnitude larger than in conventional cantilever bending experiments. Metal nanofoams can also be applied as implant materials as they have high strength-to-weight ratio and assist osseointegration. Their high porosity and interconnected nanochannels enhance bone ingrowth and insure the long-term stability of the implant.[26, 27]

Several approaches for the preparation of nanoporous metal foams have been established. Erlebacher *et al.* reported the formation of nanoporous gold by the dealloying process from a binary alloy, namely the alloy of silver and gold.[28] Silver, as a less-noble metal, can be etched away either electrochemically or by using acid, resulting in a nanoporous gold network with a ligament spacing of *ca.* 10 nm (Figure 1.1). The morphology of nanoporous gold in terms of sizes of ligaments and pores can be controlled by varying the dealloying potential.[29] An interesting approach in which the dealloying is combined with templating to render hierarchically porous gold has been reported by Nyce *et al.*[30] First, Ag-Au alloy was electroless plated onto micron-sized spheres of polystyrene and then the polymer was removed by pyrolysis. Finally, silver was etched away from Ag-Au alloy using nitric acid, leaving behind hierarchically porous gold.

Sol–gel techniques are well-developed for the synthesis of metal nanoparticles, but their applicability to assemble nanoparticles into metal foams appears to be very challenging. It has been found that the solubility of metal nanoparticles and the removal of the stabilizing ligand are the most important criteria for successful preparation of porous metals.[31] In one example of gold nanofoam preparation via the sol–gel route, highly water-soluble Au nanoparticles (solubility up to 30 wt %), stabilized with a mixture of hydrophilic and hydrophobic ligands, were dissolved in water and the solution was oxidized with hydrogen peroxide. Nanostructured gold precipitates were formed after 48 h (Figure 1.2).[18]

Leventis *et al.* have recently reported a viable route towards metal nanofoams through nanosmelting of hybrid polymer/metal aerogels.[32] Using the sol–gel

approach, an aerogel consisting of resorcinol-formaldehyde (RF) polymer and iron oxide was prepared. Subsequently, the aerogel was exposed to high temperatures (800–1000 °C) under argon atmosphere, which led to simultaneous polymer degradation and iron oxide reduction to metallic iron (Figure 1.3). Similarly, the preparation of porous Cu, Ni, Sn, and Co networks by nanosmelting has been demonstrated.[33]

Combustion synthesis represents another pathway for the nanostructured metal production, in which metal is mixed with the energetic precursor that releases energy during its decomposition and drives the formation of metal nanofoam. Tappan *et al.* have demonstrated the preparation of nanoporous Fe, Cu, Co, and Ag via combustion synthesis.[34]

Utilizing previously presented techniques, one can prepare highly porous metal foams with nano-sized pores. However, the prepared foams are typically highly disordered, which disables the effective stress transmission from the ligament nanoscale to the overall macroscale and results in poor mechanical properties.[35-37] The ordering issue can be overcome in the alternative block copolymer template-directed approach for metal nanofoam synthesis.

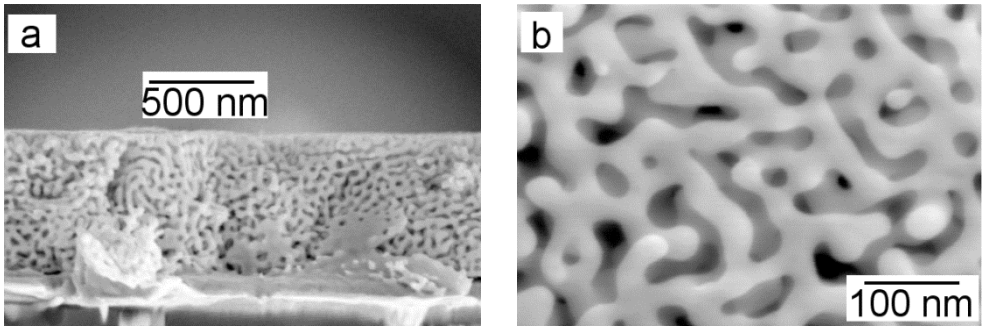

Figure 1.1. *Scanning electron micrographs of nanoporous gold obtained from Ag-Au alloy by selective Ag etching in nitric acid. a) Cross-section of dealloyed* $Ag_{32\%}Au_{68\%}$*, b) Plan view of dealloyed* $Ag_{26\%}Au_{74\%}$ *(atom%). Adapted from Ref. [28].*

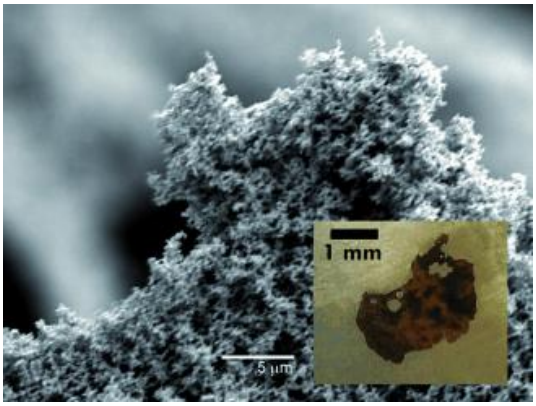

Figure 1.2. *Scanning electron micrograph of nanoporous gold obtained from sol–gel approach. Reprinted from Ref. [18].*

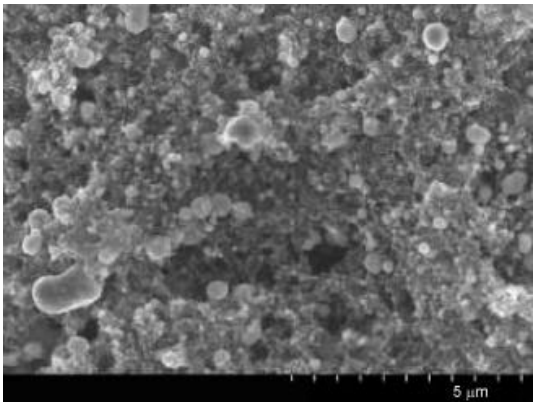

Figure 1.3. *Scanning electron micrograph of iron aerogel prepared by nanosmelting of RF/iron oxide aerogel. Reprinted from Ref. [18].*

1.3 Self-assembled block copolymers and supramolecular complexes

Chemically distinct polymers generally do not mix, but macrophase separate, in a similar fashion to oil and water. In a block copolymer, two or more chemically different homopolymers are covalently linked and this linkage prevents macrophase separation. However, due to the unfavorable interactions between the different blocks, phase separation still occurs but, because of their connectivity, only on the nanometer scale and this process is called microphase separation. The unfavorable interactions between chemically distinct species induce stretching of the polymer chains (*i.e.*, to minimize the interaction enthalpy) and the entropic elasticity (of the entropic spring) resists this stretching (*i.e.*, to maximize the conformational entropy). This enthalpy–entropy balance governs the microphase separation in block copolymers. Experimentally, the block copolymer phase behavior can be controlled by the selection of the composition and the architecture of the block copolymer, the overall degree of polymerization and the segment–segment interaction parameter.[38-41] The schematic illustrations of common, classical, and some complex phases are depicted in Figure 1.4, illustrating the domains of the minority phase. In the enlarged view of the lamellar morphology, the self-assembly of individual molecules within the domains is shown where blue and red parts represent the two chemically distinct blocks.[42] The phase diagram of diblock copolymers was theoretically predicted using self-consistent mean-field theory (Figure 1.5a).[43, 44] Experimental phase diagrams are found to generally be similar to the calculated one, except that they appear more asymmetric. The experimentally determined phase diagram of polystyrene-*block*-polyisoprene (PS-*b*-PI) is represented in Figure 1.5b.[45, 46] As the number of blocks in the copolymer increases, possibilities for novel, complex structures are created. Several examples include three-domain lamellae, core-shell or alternating spheres, cylinders, and gyroid, perforated structures and others.[46-50] Similarly, complex polymer architectures give rise to new, intriguing morphologies. For instance, a star-shaped architecture results in Archimedean tiling pattern morphologies that are unique for this type of copolymers.[51]

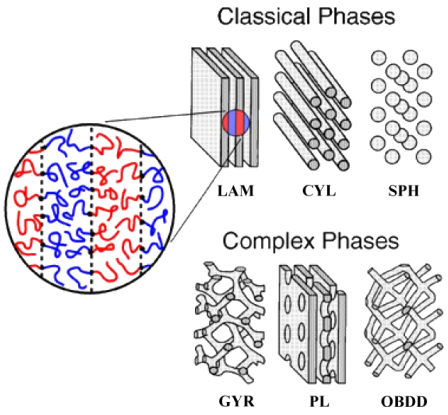

Figure 1.4. *Schematic representations of block copolymer structures showing only the domains of the minority phase. The lamellar (LAM), cylindrical (CYL), and the spherical (SPH) morphology are three examples of common, classical, phases and the gyroid (GYR), perforated lamellar (PL), and the ordered bicontinuous double diamond (OBDD) are three examples of the more complex morphologies revealed in diblock copolymers. The enlarged view of the LAM phase depicts the self-assembly of individual block copolymer chains within this morphology. Adapted with permission from Ref. [42].*

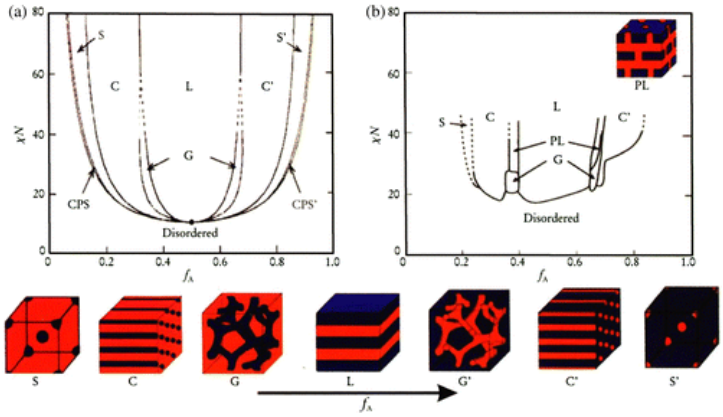

Figure 1.5. *a) Block copolymer phase diagram as calculated using the self-consistent mean-field theory, b) Experimentally determined phase diagram of PS-b-PI. Schematic representations of different morphologies are given below the diagrams. Reprinted with permission from [46]. Copyright 1999, American Institute of Physics.*

When additional components are combined with copolymer systems, the obtained complexes exhibit interesting phase behavior. Supramolecular complexes are defined as assemblies of molecules held together by non-covalent interactions. A specific example of a supramolecular complex is the so-called comb-coil block copolymer in which one of the blocks, namely the comb block, contains side chains that are non-covalently linked to the main chain, usually via hydrogen bonds. A supramolecular complex of polystyrene-*block*-poly(4-vinylpyridine) (PS-*b*-P4VP) and pentadecylphenol (PDP) has been extensively studied in the group of Ikkala and our group.[52-55] Each PDP molecule contains a hydroxyl group which can act as a hydrogen-bond promoting group and each repeating unit of P4VP contains a nitrogen atom that can act as a hydrogen-bond accepting group. Therefore, if PDP is added to P4VP, hydrogen bonds are formed between the nitrogen of the pyridine ring and the hydrogen on the phenol ring. The chemical structure and the schematic representation of the PS-*b*-P4VP(PDP) supramolecule is illustrated in Figure 1.6a. Non-polar PDP alkyl tails microphase separate from P4VP in such a way that PDP molecules align perpendicularly to the P4VP homopolymer which gives rise to the formation of two length scale structures-within-structures (Figure 1.6b). The variation in the PDP content allows for the simple tuning of the long-length scale morphology of the complex.[56, 57] Furthermore, PDP can be selectively removed by an appropriate solvent (*e.g.*, ethanol), resulting in nanoporous polymer material.[54]

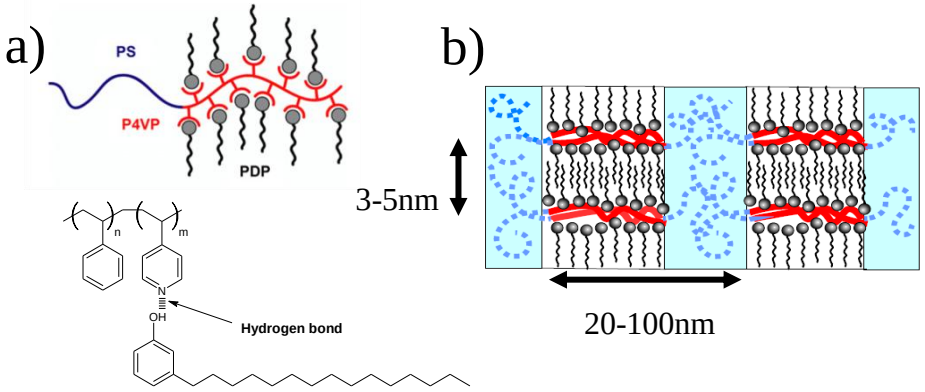

Figure 1.6. *a) The chemical structure and the schematic representation of PS-b-P4VP(PDP) supramolecule, b) PS-b-P4VP(PDP) supramolecules self-assemble into hierarchically ordered structures-within-structures.*

1.4 What do block copolymers and butterflies have in common?

The gyroid morphology was first identified in 1967 in strontium soaps by Luzzatti and Spegt.[58] Three years later, this bicontinuous triple periodic minimal surface was mathematically described by the NASA physicist Alan Schoen and named "gyroid".[59] The single gyroid contains the percolated network and matrix phases and it is characterized by the $I4_132$ symmetry, while the double gyroid with *Ia3d* symmetry has two parallel network phases that are related by inversion (Figure 1.7).[60] The transmission electron micrographs typical for a bicontinuous polymer phase were published already in 1976, but the authors did not comment on the bicontinuous nature of the system.[61] The bicontinuous ordered polymer structure was reported for the first time in 1986 by Alward *et al*. in a star-block copolymer comprised of PS-*b*-PI arms.[62] Thomas *et al*. described the observed morphology as the ordered bicontinuous double diamond (OBDD) with *Pn3m* symmetry.[63] However, theoretical calculations that followed did not provide the evidence that the OBDD is an equilibrium structure in AB diblock copolymers.[64-67] The gyroid morphology in block copolymers has been described for the first time in 1994.[68, 69] Hajduk *et al*. analyzed a linear diblock copolymer PS-*b*-PI containing 37 wt % PS, using small-angle X-ray scattering (SAXS) and transmission electron microscopy (TEM). TEM images suggested the bicontinuous morphology, but SAXS data were inconsistent with the OBDD structure. Peaks in the SAXS pattern were found at the positions √6, √8, √20, √22, √32 and √38 which are allowed by twelve cubic space groups. One of them, the *Ia3d* space group, has additional five allowed reflections that were not present in the experimental Bragg pattern, while the others have seven or more. A space filling model with *Ia3d* symmetry was generated and used to predict SAXS and TEM results. They found a good agreement between the predicted and the experimental data.[68] Theoretical calculations that followed confirmed that the double gyroid can be an equilibrium structure in AB diblock copolymers.[43] In more complicated block copolymer systems, such as block copolymer blends, variations of double gyroid morphology have been discovered. The core-shell double gyroid phase is one example in which gyroid networks are built out of two different polymer blocks, one being a core and the other a corona of gyroid networks that are embedded in the third polymer block that represents a gyroid matrix.[70]

The double gyroid as an isotropic structure with continuous triple periodic percolated domains appears to be superior to classical morphologies (lamellar,

cylindrical or spherical) for a number of technological applications. For instance, the gyroid structure, due to the high interfacial area per specimen volume, could be exploited for gas separation purposes.[71] Shefelbine *et al.* prepared ABC triblock copolymer with the core-shell double gyroid morphology. Glassy polystyrene was chosen as a middle block that separated two rubbery end blocks – polyisoprene and polydimethylsiloxane. A gas mixture would enter one rubbery block, characterized by high permeability and low selectivity. Further, it would diffuse selectively through a glassy layer and would, finally, be collected from the second rubbery layer. Furthermore, due to the ordering and periodicity in three dimensions, the gyroid structure is an excellent candidate for the photonic crystal application.[72-74] Urbas *et al.*[73] examined the optical properties of the gyroid forming PS-*b*-PI block copolymer with spacing comparable to the wavelength of visible light. Furthermore, the gyroid forming block copolymers could be used for templating purposes: one block could be selectively removed, which results in a porous gyroid template that can be, for example, backfilled with an inorganic material. This will be further elaborated in Section 1.5 and supported with examples in Section 1.6. For templating purposes, the gyroid is preferable over anisotropic block copolymer phases (*e.g.*, cylindrical) which often require laborious alignment procedures prior to the application.[75-77]

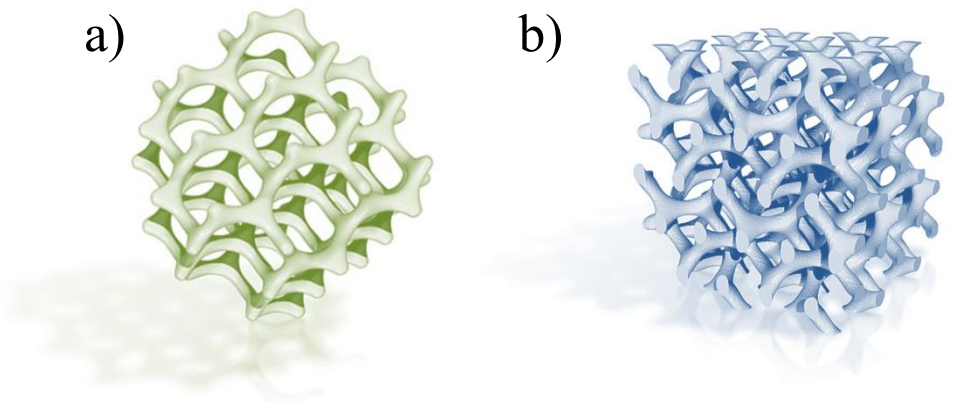

Figure 1.7. *a) The single gyroid morphology with $I4_132$ symmetry, b) the double gyroid morphology with Ia3d symmetry. Adapted with permission from Ref. [78].*

The gyroid structure appears also in nature, namely in butterfly wing scales, and it is responsible for the shimmering wing colors of several butterfly species.

Saranathan *et al.*[79] investigated 3D photonic nanostructures in five butterfly species by SAXS, TEM and SEM and identified their morphology as the single gyroid with $I4_132$ symmetry (Figure 1.8 and 1.9). The butterflies initially develop the thermodynamically favorable double gyroid phase that consists of two networks, different in composition, embedded in a matrix. Chitin is then deposited on one of the two networks and after the cell dies, the chitin-air structure is left behind. The morphology of the porous chitin structure is single gyroid which is optically more efficient than the double gyroid one. This structure could be mimicked in gyroid forming ABC terpolymers, with two chemically distinct networks.[80] A single gyroid template could be provided by the selective removal of one of the networks.

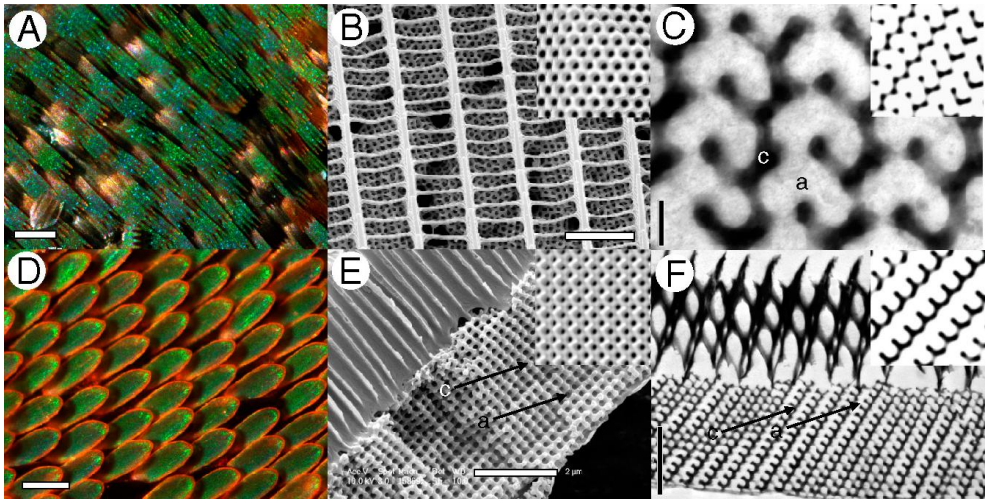

Figure 1.8. *Anatomy of the structural color-producing nanostructures in lycaenid and papilionid butterflies: a, d) light micrographs (scale bars 100 μm), b, e) SEM images (scale bars 2.5 and 2 μm, respectively), c, f) TEM images (scale bars 200 nm and 2 μm, respectively). Reprinted with permission from [79].*

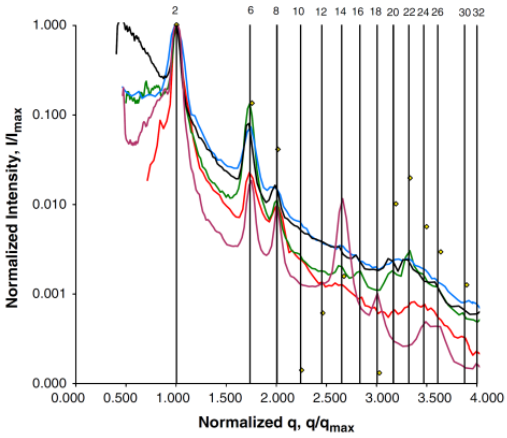

Figure 1.9. *SAXS patterns of the nanostructures of five different butterfly species indicating the single gyroid morphology with $I4_132$ symmetry. Reprinted with permission from [79].*

1.5 Block copolymer template directed preparation of metal nanofoams

The nanoscale ordering in block copolymer structures can be extended to inorganic materials with more appealing properties, *e.g.*, metals. This process generally encompasses several steps (Figure 1.10):

1. Selective removal of the sacrificial polymer block,
2. Backfilling of the porous structure with inorganic material (*e.g.*, metal),
3. Removal of the remaining polymer template.

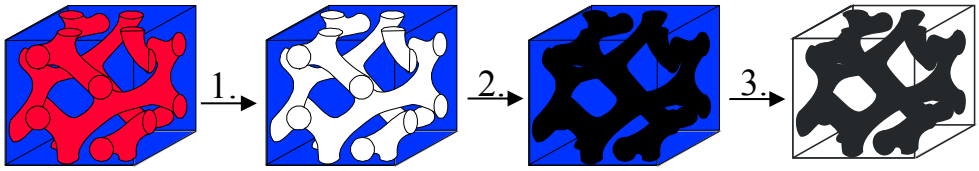

Figure 1.10. *Block copolymer template-directed preparation of ordered inorganic nanostructures: 1. selective removal of the sacrificial polymer block, 2. backfilling of the porous structure with inorganic material (e.g., metal), 3. removal of the remaining polymer template.*

The first two steps can be combined into one by selective inclusion of inorganic compounds, *e.g.*, metal ions, in one of the copolymer blocks.[81]

1.5.1 Selective removal of the sacrificial polymer block

In recent years, many studies successfully demonstrated the selective degradation of polymer blocks from a self-assembled block copolymer structure. Polydiene blocks, such as polyisoprene (PI) or polybutadiene (PBD), can be etched away via ozonolysis.[82-84] Chen *et al.*[84] examined the ozonolysis efficiency in blends of block copolymer PS-*b*-PI and homopolymer PS, and found a strong dependence on the morphology of the PI microdomains. The degree of ozonization after 24 h reaction demonstrated a decreasing trend from 90, 80, 70 to 50 % if the PI microdomains transformed from lamellae, to gyroid network, to cylinders, to spheres, respectively, in the PS matrix, which was attributed to the decrease of the contact area PI/ozone and the accessible volume of PI microdomains.
UV irradiation can be employed for selective removal of PMMA blocks. The exposure of PS-*b*-PMMA block copolymer to UV light leads to degradation of the PMMA phase and simultaneous crosslinking of the PS phase.[85] If a blend of block copolymer PS-*b*-PMMA and homopolymer PMMA is used as a precursor, the nanoporous structure can be generated in two ways: (1) all PMMA (PMMA block and PMMA homopolymer) can be removed by UV irradiation or (2) only PMMA homopolymer can be removed using a selective solvent, namely acetic acid.[86]
Polylactic acid (PLA) blocks can be readily removed from a block copolymer (*e.g.*, PS-*b*-PLA) by a mild aqueous base.[87-89] From crystalline-amorphous block copolymers, such as polyethylene-*block*-polystyrene (PE-*b*-PS) or polystyrene-*block*-poly(vinylidene fluoride)-*block*-polystyrene (PS-*b*-PVDF-*b*-PS), the amorphous component can be selectively etched with fuming nitric acid.[90, 91] Reactive ion etching can be used to generate porous structures from block copolymer precursors with one etch-resistant block.[92-95] Finally, amphiphilic molecule PDP can be removed from a supramolecular complex containing P4VP(PDP) comb-block by selective dissolution in ethanol, as already mentioned in Section 1.3, resulting in porous polymer template.[54]

1.5.2 Backfilling of the porous structure with inorganic material

Metal oxides (*e.g.,* SiO_2 or TiO_2) can be introduced inside the pores of a polymer template via the sol–gel process. In the sol–gel process, the starting colloidal solution – sol, typically composed of metal alkoxides or metal salts, fills pores of a polymer template and subsequently, via hydrolysis and polycondensation reactions, transforms into gel – an integrated network composed of discrete colloidal particles or polymer networks.[96] Hsueh *et al.* prepared a polystyrene-*block*-poly(L-lactide) (PS-*b*-PLLA) block copolymer with double gyroid morphology and then selectively removed the PLLA block via hydrolysis.[97, 98] The obtained porous PS network was filled with amorphous SiO_2 via the sol–gel process. The SAXS pattern, TEM and electron tomography (Figure 1.11a) images of the PS/SiO_2 nanohybrid confirmed its double gyroid morphology. After the polymer removal, a gyroid forming SiO_2 network was exposed (Figure 1.11b) and its porosity was calculated from nitrogen adsorption measurements to be 66 %. The refractive index of dense amorphous SiO_2 is rather low and it further decreases in the porous sample. The refractive index of the prepared gyroid SiO_2 network was estimated to be about 1.1, thus it appeared suitable for optical applications such as antireflection structures.[97] The hydrolysis reaction rate in the sol–gel process towards SiO_2 is exceptionally low, which allows for complete diffusion of sol into the template pores before the gelation starts. On the other hand, titanium alkoxides are not as stable and pores will be blocked by gel before sol completely penetrates the template. Therefore, to fabricate the gyroid PS/TiO_2 nanohybrid, one has to carefully control the reaction conditions. The sol–gel reaction was acid-catalyzed and performed at low temperature (0–10 °C) to prevent pores closure by the oversized gels. Methanol was used as a co-solvent to increase the wetting, but prevent the swelling of the PS template. Since methanol, as a polar solvent, increased the instability of Ti alkoxides, chelating agents, such as diethanolamine, were also applied to countervail the methanol effect. Furthermore, a thermal treatment was employed to remove PS and expose the free-standing, gyroid anatase TiO_2 (Figure 1.12). Its photocatalytic efficiency was determined by evaluating the degradation of methylene blue under UV irradiation. It was found that the decomposition reaction follows first-order kinetics and that the reaction rate is about two times higher in comparison to commercial TiO_2 powder.[98]

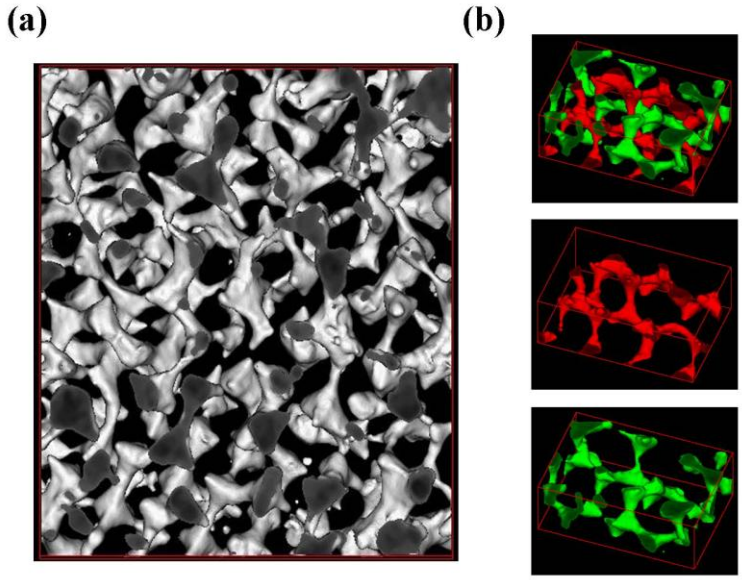

Figure 1.11. *The reconstructed 3D images of: a) gyroid PS/SiO_2 nanohybrid, b) gyroid SiO_2 composed of two parallel networks related by inversion (red and green). Reprinted with permission from Ref. [97]. Copyright 2010 American Chemical Society.*

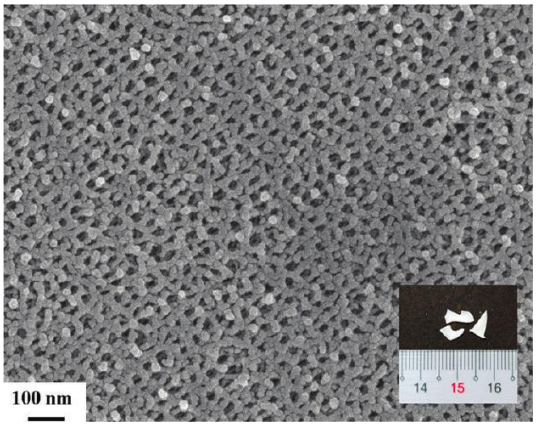

Figure 1.12. *SEM micrograph of the gyroid anatase TiO_2 network. The inset represents the centimeter-sized bulk sample. Reprinted with permission from Ref. [98]. Copyright 2012 American Chemical Society.*

Electrochemical and electroless plating are commonly used techniques to deposit metals onto or into templates.[99-102] To electrochemically deposit metal inside the pores of a polymer template, the working electrode is usually coated by a template and, together with the counter and the reference electrode, placed in the plating bath and connected to an external source of current. To completely plate the sample, the surface of the underlying working electrode should be accessible to the plating bath, which may appear difficult for thicker polymer templates with many defects or highly complex structure. Also relatively simple polymer templates, such as the cylindrical one, require proper alignment prior to electrochemical plating. In electroless plating, a polymer template is immersed into the electroless plating bath and metal is deposited via an autocatalytic process onto the surface of the template. Electroless plating does not require an external current source and allows plating onto complex shapes and through pores. Furthermore, non-conductive surfaces, such as polymers or ceramics, can undergo electroless plating after the appropriate treatment. The pretreatment usually consists of two steps: (1) sensitization in $SnCl_2$/HCl, when Sn^{2+} ions adsorb onto the template surface, (2) activation in $PdCl_2$/HCl, when Pd sites are formed through the following redox reaction: $Sn^{2+} + Pd^{2+} \rightarrow Sn^{4+} + Pd^0$. The Pd sites act as catalysts during the electroless metal plating procedure. In electroless deposition, metal ions, M^{z+}, are reduced by the reducing agent, R^{n-}, and the process can be simply described as: $M^{z+} + R^{n-} \rightarrow M^0 + R^{z-n}$. The process is autocatalytic, *i.e.*, it is catalyzed by metal being deposited. Besides the source of metal ions and the reducing agent, the electroless plating bath usually contains the complexing agent, that acts as a buffer and reduces the concentration of free metal ions, and the stabilizer, that prevents the decomposition of the plating solution.

1.5.3 Removal of the remaining polymer template

There are several methods to remove polymer from the polymer/inorganic nanohydbrid, such as pyrolysis,[30] dissolution,[103, 104] UV degradation,[97, 98] *etc.*

Pyrolysis involves the decomposition of polymer at elevated temperature, leaving behind an inorganic material with preserved morphology. Inorganic materials may as well undergo changes at elevated temperatures. For instance, thermal treatment will increase the crystallinity of TiO_2, thus, amorphous TiO_2 may transform to one of its crystalline forms: rutile, anatase, and brookite.[98] Another example is

nanoporous gold that undergoes thermal coarsening due to the recrystallization in solid state at elevated temperatures.[105] Therefore, the applicability of pyrolysis for polymer template removal depends on the type of inorganic material and its purposes.

1.6 Examples of metal nanofoams prepared by block copolymer templating

There have been a few reports in the literature demonstrating the replication of complex block copolymer structures into the ordered metal phase. This section describes several prominent examples and focuses on the fabrication of gyroid metal nanofoams.

Crossland *et al.*[103] investigated the thin film morphology of poly(4-fluorostyrene)-*block*-poly(D,L-lactide) (PFS-*b*-PLA) that in bulk acquires the cylindrical morphology at 150 °C and the gyroid morphology at 180 °C. When the thin film was annealed for 35 h at 180 °C, and then cooled down to room temperature over 3 h, it was found to adopt the gyroid phase in the entire sample volume. The PLA block was then selectively removed by hydrolysis in a mild aqueous base and platinum was deposited into the remaining pores via electrochemical deposition. Final removal of the PFS block, by dissolution in toluene or exposure to O_2 plasma, resulted in isolated mounds or a continuous freestanding array of a gyroid Pt replica (Figure 1.13) depending on the properties of the underlying substrate. Smooth Au-coated silicon substrate favors the formation of isolated mounds of Pt replica (Figure 1.13a and 1.13b). Chemical modification of the Au-coated silicon substrate using a self-assembled monolayer (SAM) of 1-undecanethiol induced much higher substrate coverage (Figure 1.13c and 1.13d). Presumably, in comparison to Au, SAM is more energetically neutral to copolymer blocks and does not favor the PFS phase. Surface topography is also found to significantly influence the replication of gyroid Pt over large areas. FTO-glass or Au-coated FTO glass, with the amplitude of surface roughness (*ca.* 50 nm) comparable to the copolymer domain spacing, led to the complete surface coverage and formation of a continuous freestanding array of gyroid Pt replica.

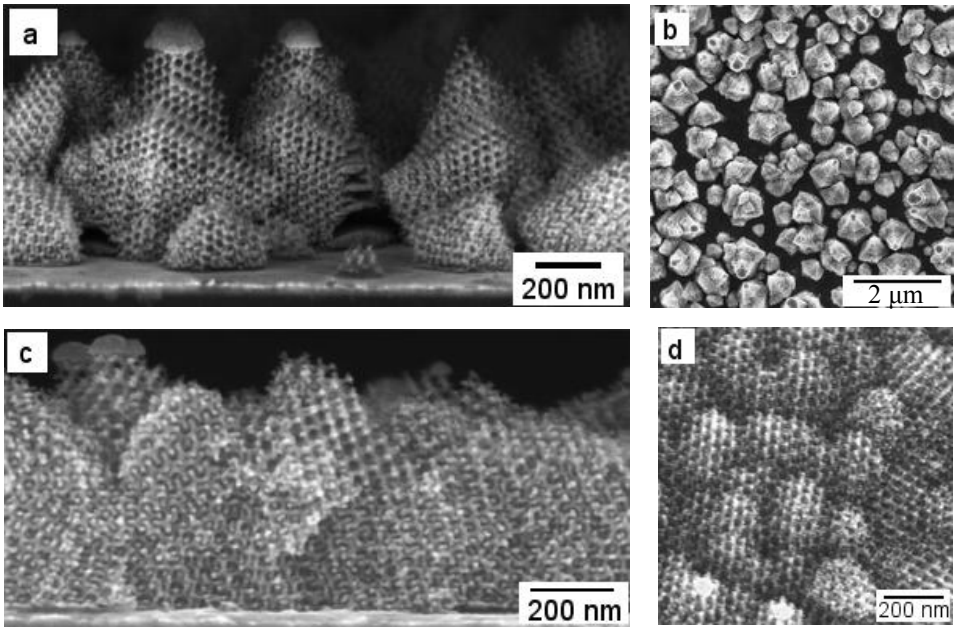

Figure 1.13. *SEM images in cross-sectional and plan view of two gyroid Pt replicas. a, b) If underlying substrate was Au-coated silicon substrate, isolated mounds of gyroid Pt replica are formed, c, d) If underlying substrate was Au-coated silicon substrate modified with a self-assembled monolayer of 1-undecanethiol, a continuous freestanding array of gyroid Pt replica is formed. Adapted from Ref. [103].*

Vignolini *et al.*[106] demonstrated the creation of a gold optical metamaterial starting from triblock copolymer polyisoprene-*block*-polystyrene-*block*-polyethylene oxide (PI-*b*-PS-*b*-PEO). The polymer adopted the double gyroid morphology with two chemically distinct networks (PI and PEO) in a matrix of polystyrene. The PI network was selectively removed by UV irradiation and subsequent rinsing with ethanol. Then, the polymer template was backfilled with gold by electrochemical deposition, and finally, the remaining template was removed by plasma etching resulting in a single gyroid, nanoscale ordered Au foam. The preparation procedure is schematically depicted in Figure 1.14. The single gyroid Au replica was examined under linearly polarized light (Figure 1.15). The tested area contained one grain boundary that divided the sample into two domains with the same orientation perpendicular to the substrate surface and the

twinning in lateral direction. At the twinning boundary, the angle between [100] directions was found to be about 105° (Figure 1.15a). Both domains reflected the identical color when the polarization of incident light was perpendicular to the grain boundary (Figure 1.15b). If the polarization of incident light was parallel to the [100] direction of one of the domains (simultaneously, it is almost perpendicular to the [100] direction of the other domain), the largest optical contrast was observed (Figure 1.15c). The absorption peak was found to tune sinusoidally between 525 and 630 nm with the polarization direction (Figure 1.15e). For the polarization along the [100] direction in the single gyroid Au, the absorption peak appeared at short wavelengths and is red-shifted for polarization in perpendicular direction (Figure 1.15d). Additionally, the Au replica exhibits optical chirality. Transmission measurements with circularly polarized light were performed while the sample was rotated around the [110] surface normal. The maximum transmission was observed for two rotation angles in each full turn, *i.e.*, when the optical axis coincides with the gyroid [111] chiral direction.

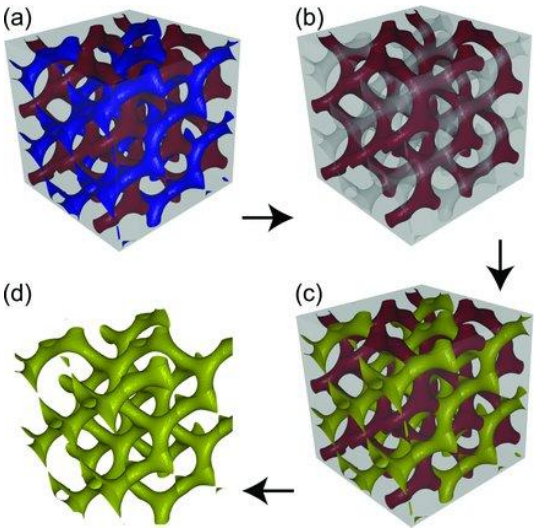

Figure 1.14. *Schematic representation of sample fabrication: a) triblock copolymer PI-b-PS-b-PEO self-assembles into the double gyroid structure with two distinct networks (blue PI and red PEO) in a matrix of PS (grey), b) the PI block is selectively removed, c) the polymer template is backfilled with gold (yellow), d) after the template removal by plasma etching, a single gyroid Au nanofoam is exposed. Reprinted from Ref. [106].*

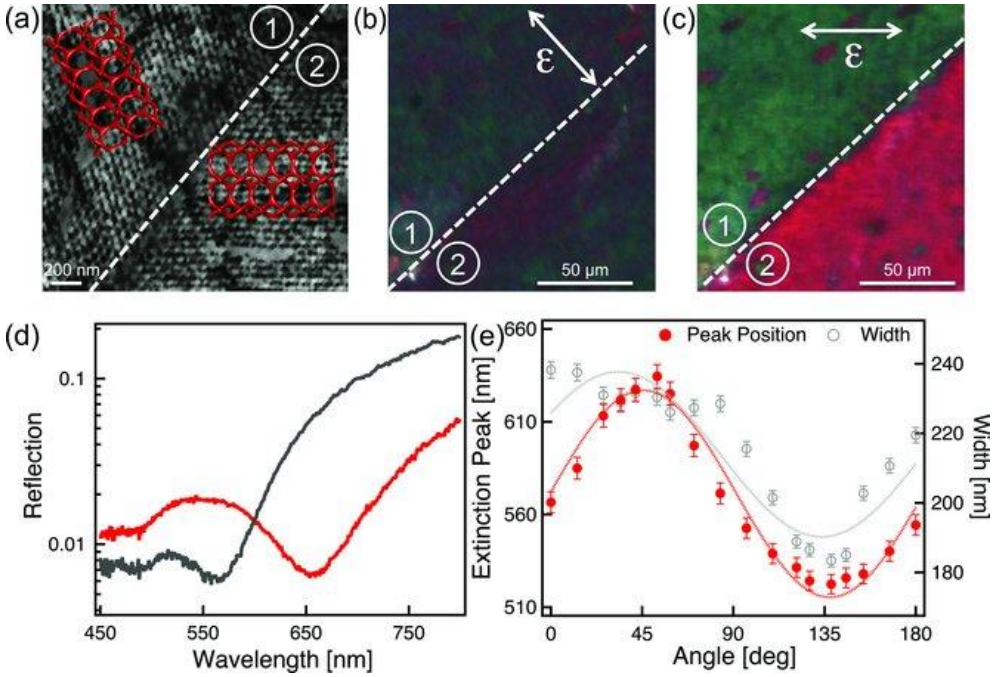

Figure 1.15. *Linear dichroism of the Au gyroid: a) SEM image of the examined sample area, b, c) Optical reflection images obtained with linearly polarized light, perpendicular to the grain boundary (b) or parallel to the [100] gyroid direction of the domain 2 (c), d) Reflection spectra for area 1 with the polarization perpendicular (red) and parallel (dark grey) to the [100] gyroid direction, e) Dependence of the extinction (reflectivity) peak position and width on the angle between the [100] gyroid direction and incident light polarization. Reprinted from Ref. [106].*

Warren *et al.*[107] demonstrated an alternative route towards ordered metal nanofoams via direct self-assembly of block copolymers with ligand-stabilized metal nanoparticles. Block copolymer polyisoprene-*block*-poly(dimethylaminoethyl methacrylate) PI-*b*-PDMAEMA and ligand-stabilized Pt nanoparticles were dissolved in chloroform. The solutions were transferred to Al dishes and heated at 50 °C for approximately 1 h until the solvent completely evaporated. After annealing at 130 °C for 2 days under vacuum, samples adopted the ordered morphology. A cylindrical sample was exposed to rapid pyrolysis and

converted to an ordered porous Pt-C composite. Finally, carbon was removed using Ar-O plasma and the Pt nanofoam was exposed. The electrical conductivity of the Pt-C composite was found to be rather high (400 S/cm). This strategy can be extended to different metals and block copolymer morphologies.

A binary mixture of PS-*b*-PI block copolymer and PS homopolymer with an overall PS volume fraction of 0.66 and the double gyroid morphology was prepared by Hashimoto *et al.*[83] After the selective removal of the PI block by ozonolysis, a gyroid polymer scaffold was electroless nickel plated. Figure 1.16 shows the TEM image of the nickel plated sample and the inset highlights 10 nm nickel particles deposited onto the surface of a 25 nm diameter nanochannel, thus leaving a 5 nm diameter empty channel in the middle. Subsequently, Hsueh *et al.*[104] reported the preparation of gyroid Ni replica starting from PS-*b*-PLLA block copolymers.

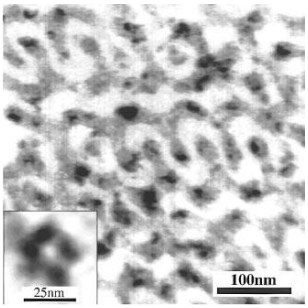

Figure 1.16. *The TEM image of the electroless nickel plated polymer template with the double gyroid morphology. The inset shows a 25 nm nanochannel coated with 10 nm nickel nanoparticles. Reprinted with permission from Ref. [83]. Copyright 1997 American Chemical Society.*

1.7 Thesis overview

This thesis focuses on the characterization and application of supramolecular complexes based on low molecular weight PDP and block copolymer containing P4VP block. In chapter 2, supramolecular complexes based on amphiphilic PDP molecules and triblock copolymer poly(*tert*-butoxystyrene)-*block*-polystyrene-*block*-poly(4-vinylpyridine) (P_tBOS-*b*-PS-*b*-P4VP) are evaluated as precursors to well-ordered metallic nanostructures. Several samples with core-shell double gyroid morphology are found and nanoporous structures, obtained after PDP removal in ethanol, are electroless nickel plated. Channels located close to the surface become filled with nickel, while ones in the middle of the film remain empty.

The other chapters focus on supramolecular complexes based on amphiphilic PDP and diblock copolymer polystyrene-*block*-poly(4-vinylpyridine) (PS-*b*-P4VP). Their phase behavior is meticulously examined in chapters 3 and 4. In chapter 3, the phase behavior of the complexes with P4VP(PDP) as a majority component is studied, and between the lamellar and cylindrical region in the phase diagram, several samples with double gyroid morphology were found. The size of the gyroid unit cell and the porosity of the subsequently obtained nanoporous template can be tuned by careful selection of the parent block copolymer PS-*b*-P4VP.

Chapter 4 focuses on the PS-*b*-P4VP(PDP) complexes with P4VP(PDP) as a minority component. Between cylindrical and lamellar region in the phase diagram, instead of the expected gyroid phase, a hexagonally perforated layer (HPL) phase is detected. HPL is a metastable phase in neat block copolymers, but appears as an equilibrium phase in supramolecular complexes. This atypical phase behavior is examined and elaborated in chapter 4.

In chapter 5, the utilization of gyroid-forming PS-*b*-P4VP(PDP) complexes as precursors to well-ordered metal nanofoams is investigated. The formation of well-ordered inverse gyroid nickel replica is reported. The emptied gyroid structure is backfilled with nickel via electroless plating technique and the remaining polymer is subsequently removed by pyrolysis.

In the future, metal nanofoam characteristics are expected to be improved and adjusted to meet the requirements for desired applications. For instance, their structure can be tailored by employing alternative block copolymer phases as precursors, such as the orthorhombic *Fddd* network[108] or plumber's nightmare[109] phase. Furthermore, their chemical composition can be varied and

alternative metals, such as Ag, Pd, Co, Cr, *etc*., can be deposited in the polymer template channels, leading to new ordered metal nanofoams. Additionally, block copolymer template-directed synthesis can be combined with dealloying; from the alloy deposited in block copolymer template channels, a less noble metal can be removed, leading to a hierarchically porous ordered metal nanofoam. The synthetic routes towards well-ordered metal nanofoams and their application potential are still poorly examined and further investigation and exciting discoveries are expected to emerge.

The outline of this thesis is depicted in Figure 1.17.

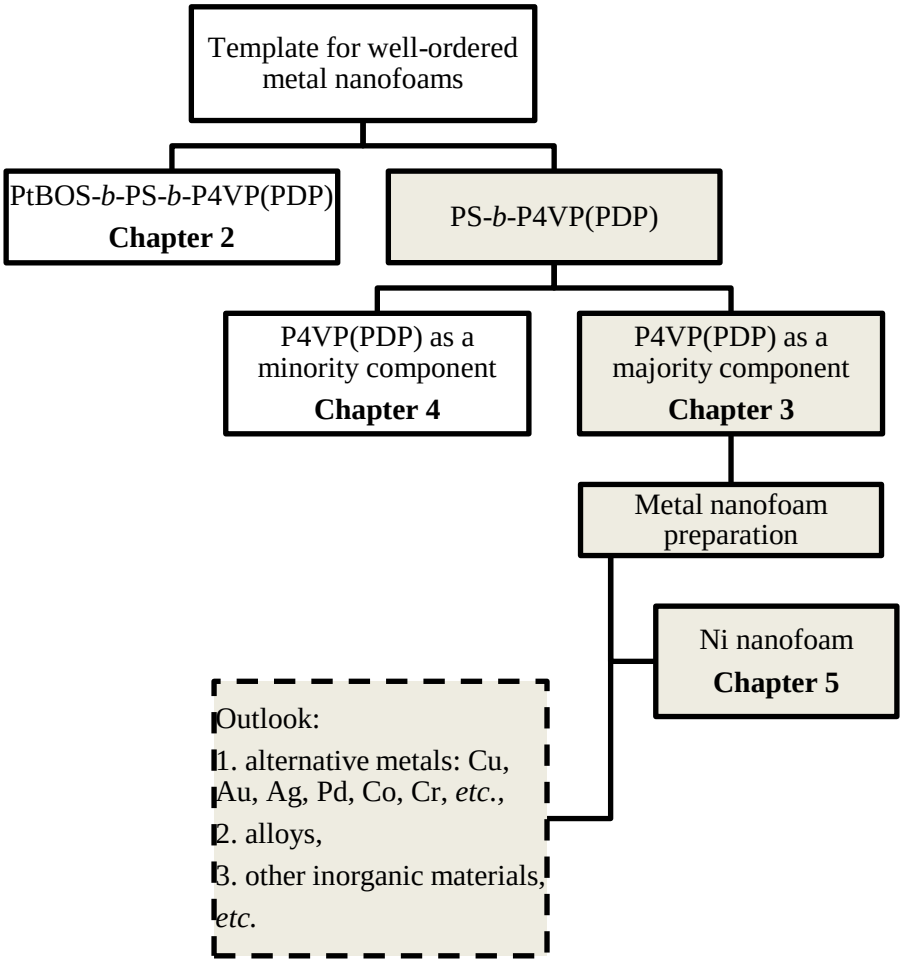

.

Figure 1.17. *Schematic representation of the thesis outline*

1.8 References

1. Mahtab R, Rogers JP, Murphy CJ. J Am Chem Soc 1995;117(35):9099-9100.
2. Weissleder R, Elizondo G, Wittenburg J, Rabito C, Bengele H, Josephson L. Radiology 1990;175:489-493.
3. de la Isla A, Brostow W, Bujard B, Estevez M, Rodriguez JR, Vargas S, et al. Mat Resr Innovat 2003;7:110-114.
4. Salata OV. J Nanobiotechnology 2004;2:3-8.
5. Roy I, Ohulchanskyy TY, Pudavar HE, Bergey EJ, Oseroff AR, Morgan J, et al. J Am Chem Soc 2003;125(26):7860-7865.
6. Duncan TV. J Colloid Interface Sci 2011;363:1-24.
7. Cuenya BR. Thin Solid Films 2010;518:3127-3150.
8. Yamauchi M, Kobayashi H, Kitagawa H. ChemPhysChem 2009;10(15):2566-2576.
9. Pasquini L, Brighi M, Montone A, Antisari MV, Dam B, Palmisano V, et al. IOP Conf Ser: Mater Sci Eng 2012;38:12001-12008.
10. Reiss G, Hutten A. Nat Mater 2005;4:725-726.
11. Xia Y, Yang P, Sun Y, Wu Y, Mayers B, Gates B, et al. Adv Mater 2003;15(5):353-389.
12. Yuan J, Müller AHE. Polymer 2010;51(18):4015-4036.
13. Park S, Kim B, Cirpan A, Russell T. Small 2009;5(11):1343-1348.
14. Smith D. Thin Film Deposition: Principles and Practice. New York: McGraw-Hill, 1995.
15. George SM. Chem Rev 2010;110:111-131.
16. Knoll W, Advincula RC. Functional Polymer Films: Wiley-VCH, 2011.
17. Zhou W, Wang ZL. Three-Dimensional Nanoarchitectures. New York: Springer, 2011.
18. Tappan BC, Steiner SA, Luther EP. Angew Chem Int Ed 2010;49(27):4544-4565.
19. Berube V, Radtke G, Dresselhaus M, Chen G. Int J Energy Res 2007;31(6-7):637-663.
20. Sakintuna B, Lamari-Darkrim F, Hirscher M. Int J Hydrogen Energy 2007;32(9):1121-1140.
21. Berube V, Chen G, Dresselhaus MS. Int J Hydrogen Energy 2008;33:4122-4131.

22. Rolison DR, Long JW, Lytle JC, Fischer AE, Rhodes CP, McEvoy TM, et al. Chem Soc Rev 2009;38(1):226-252.
23. Gleiter H, Weissmüller J, Wollersheim O, Würschum R. Acta Materialia 2001;49(4):737-745.
24. Jin H-J, Weissmüller J. Adv Eng Mater 2010;12(8):714-723.
25. Kramer D, Viswanath RN, Weissmüller J. Nano Letters 2004;4(5):793-796.
26. Bobyn JD, Stackpool GJ, Hacking SA, Tanzer M, Krygier JJ. J Bone Joint Surg Br 1999;81:907-914.
27. Willie BM, Yang X, Kelly NH, Merkow J, Gagne S, Ware R, et al. J Biomed Mater Res B Appl Biomater 2010;92:479-488.
28. Erlebacher J, Aziz MJ, Karma A, Dimitrov N, Sieradzki K. Nature 2001;410:450-453.
29. Detsi E, van de Schootbrugge M, Punzhin S, Onck PR, De Hosson JTM. Scripta Mater 2011;64(4):319-322.
30. Nyce GW, Hayes JR, Hamza AV, Satcher JH. Chem Mater 2007;19(3):344-346.
31. Gacoin T, Lahlil K, Larregaray P, Boilot JP. J Phys Chem B 2001;105(42):10228-10235.
32. Leventis N, Chandrasekaran N, Sotiriou-Leventis C, Mumtaz A. J Mater Chem 2009;19(1):63-65.
33. Leventis N, Chandrasekaran N, Sadekar AG, Sotiriou-Leventis C, Lu H. J Am Chem Soc 2009;131(13):4576-4577.
34. Tappan BC, Huynh MH, Hiskey MA, Chavez DE, Luther EP, Mang JT, et al. J Am Chem Soc 2006;128(20):6589-6594.
35. Ashby MF, Evans AG, Fleck NA, Gibson LJ, Hutchinson JW, Wadley HG. Metal Foams: a Design Guide. Oxford, UK: Butterworth-Heinemann, 2000.
36. Tekoglu C. Size Effects in Cellular Solids. University of Groningen, 2007.
37. Amsterdam E. Structural Performance and Failure Analysis of Aluminium Foams. University of Groningen, 2008.
38. Bates FS, Fredrickson GH. Annu Rev Phys Chem 1990;41:525-527.
39. Hamley IW. The Physics of Block Copolymers. Oxford: Oxford University Press, 1998.

40. Abetz V, Simon P. Phase Behaviour and Morphologies of Block Copolymers. Adv Polym Sci, vol. 189: Springer Berlin / Heidelberg, 2005. pp. 125-212.
41. Abetz V, Boschetti-de-Fierro A. Block Copolymers in the Condensed State. In: Matyjaszewski K, Möller M, editors. Polymer Science: A Comprehensive Reference, vol. 7. Amsterdam: Elsevier BV, 2012. pp. 3-44.
42. Matsen MW. J Phys: Condens Matter 2002;14:R21-R47.
43. Matsen MW, Schick M. Phys Rev Lett 1994;72(16):2660-2663.
44. Matsen MW, Bates FS. Macromolecules 1996;29(4):1091-1098.
45. Khandpur AK, Foerster S, Bates FS, Hamley IW, Ryan AJ, Bras W, et al. Macromolecules 1995;28(26):8796-8806.
46. Bates FS, Fredrickson GH. Phys Today 1999;52:32-38.
47. Epps TH, Cochran EW, Bailey TS, Waletzko RS, Hardy CM, Bates FS. Macromolecules 2004;37(22):8325-8341.
48. Tyler CA, Qin J, Bates FS, Morse DC. Macromolecules 2007;40(13):4654-4668.
49. Gobius du Sart G, Vukovic I, Alberda van Ekenstein G, Polushkin E, Loos K, ten Brinke G. Macromolecules 2010;43(6):2970-2980.
50. Faber M, Voet VSD, ten Brinke G, Loos K. Soft Matter 2012;8(16):4479-4485.
51. Matsushita Y. Macromolecules 2007;40(4):771-776.
52. Ruokolainen J, ten Brinke G, Ikkala O. Adv Mater 1999;11(9):777-780.
53. Ruokolainen J, Saariaho M, Ikkala O, ten Brinke G, Thomas EL, Torkkeli M, et al. Macromolecules 1999;32(4):1152-1158.
54. Mäki-Ontto R, de Moel K, de Odorico W, Ruokolainen J, Stamm M, ten Brinke G, et al. Adv Mater 2001;13:117-121.
55. Ikkala O, ten Brinke G. Science 2002;295:2407-2409.
56. Valkama S, Ruotsalainen T, Nykänen A, Laiho A, Kosonen H, ten Brinke G, et al. Macromolecules 2006;39(26):9327-9336.
57. Nandan B, Vyas MK, Böhme M, Stamm M. Macromolecules 2010;43(5):2463-2473.
58. Luzzatti V, Spegt P. Nature 1967;215:701-702.
59. Schoen AH. NASA Technical Note, TN D-5541 1970.
60. Meuler AJ, Hillmyer MA, Bates FS. Macromolecules 2009;42:7221-7250.
61. Aggarwal SL. Polymer 1976;17:938-956.

62. Alward DB, Kinning DJ, Thomas EL, Fetters LJ. Macromolecules 1986;19:215-224.
63. Thomas EL, Alward DB, Kinning DJ, Martin DC, Handlin DL, Fetters LJ. Macromolecules 1986;19:2197-2202.
64. Anderson DM, Thomas EL. Macromolecules 1988;21(11):3221-3230.
65. Likhtman AE, Semenov AN. Macromolecules 1994;27(11):3103-3106.
66. Olmsted PD, Milner ST. Phys Rev Lett 1994;72(6):936-939.
67. Olmsted PD, Milner ST. Phys Rev Lett 1995;74(5):829-829.
68. Hajduk DA, Harper PE, Gruner SM, Honeker CC, Kim G, Thomas EL, et al. Macromolecules 1994;27(15):4063-4075.
69. Schulz MF, Bates FS, Almdal K, Mortensen K. Phys Rev Lett 1994;73(1):86-89.
70. Goldacker T, Abetz V. Macromolecules 1999;32(15):5165-5167.
71. Shefelbine TA, Vigild ME, Matsen MW, Hajduk DA, Hillmyer MA, Cussler EL, et al. J Am Chem Soc 1999;121(37):8457-8465.
72. Martín-Moreno L, García-Vidal FJ, Somoza AM. Phys Rev Lett 1999;83(1):73-75.
73. Urbas AM, Maldovan M, DeRege P, Thomas EL. Adv Mater 2002;14(24):1850-1853.
74. Michielsen K, Kole JS. Phys Rev B 2003;68(11):115107.
75. Thurn-Albrecht T, Schotter J, Kästle GA, Emley N, Shibauchi T, Krusin-Elbaum L, et al. Science 2000;290(5499):2126-2129.
76. Sidorenko A, Tokarev I, Minko S, Stamm M. J Am Chem Soc 2003;125(40):12211-12216.
77. Olayo-Valles R, Guo S, Lund MS, Leighton C, Hillmyer MA. Macromolecules 2005;38(24):10101-10108.
78. http://www.shapeways.com/shops/virtox.
79. Saranathan V, Osuji CO, Mochrie SGJ, Noh H, Narayanan S, Sandy A, et al. PNAS 2010;107:11676-11681.
80. Suzuki J, Seki M, Matsushita Y. J Chem Phys 2000;112(10):4862-4868.
81. Ghoshal T, Maity T, Godsell JF, Roy S, Morris MA. Adv Mater 2012;24(18):2390-2397.
82. Mansky P, Harrison CK, Chaikin PM, Register RA, Yao N. Appl Phys Lett 1996;68(18):2586-2588.
83. Hashimoto T, Tsutsumi K, Funaki Y. Langmuir 1997;13(26):6869-6872.

84. Chen S-Y, Huang Y, Tsiang RC-C. J Polym Sci A: Polym Chem 2008;46(6):1964-1973.
85. Thurn-Albrecht T, Steiner R, DeRouchey J, Stafford CM, Huang E, Bal M, et al. Adv Mater 2000;12(11):787-791.
86. Joo W, Yang SY, Kim JK, Jinnai H. Langmuir 2008;24(21):12612-12617.
87. Zalusky AS, Olayo-Valles R, Taylor CJ, Hillmyer MA. J Am Chem Soc 2001;123(7):1519-1520.
88. Zalusky AS, Olayo-Valles R, Wolf JH, Hillmyer MA. J Am Chem Soc 2002;124(43):12761-12773.
89. Crossland EJW, Kamperman M, Nedelcu M, Ducati C, Wiesner U, Smilgies DM, et al. Nano Letters 2008;9(8):2807-2812.
90. Uehara H, Kakiage M, Sekiya M, Sakuma D, Yamonobe T, Takano N, et al. ACS Nano 2009;3(4):924-932.
91. Voet VSD, Tichelaar M, Tanase S, Mittelmeijer-Hazeleger MC, ten Brinke G, Loos K. Nanoscale 2013;5(1):184-192.
92. Park M, Harrison C, Chaikin PM, Register RA, Adamson DH. Science 1997;276(5317):1401-1404.
93. Cheng JY, Ross CA, Thomas EL, Smith HI, Vancso GJ. Appl Phys Lett 2002;81(19):3657-3659.
94. Farrell RA, Petkov N, Shaw MT, Djara V, Holmes JD, Morris MA. Macromolecules 2010;43(20):8651-8655.
95. Voet VSD, Pick TE, Park S-M, Moritz M, Hammack AT, Urban JJ, et al. J Am Chem Soc 2011;133(9):2812-2815.
96. Brinker CJ, Scherer JW. Sol–Gel Science: The Physics and Chemistry of Sol–Gel Processing. Boston: Academic Press, 1990.
97. Hsueh H-Y, Chen H-Y, She M-S, Chen C-K, Ho R-M, Gwo S, et al. Nano Letters 2010;10(12):4994-5000.
98. Hsueh H-Y, Ho R-M. Langmuir 2012;28(22):8518-8529.
99. Riedel W. Electroless Nickel Plating. Finishing Publications: Metals Park, 1991.
100. Mallory GO, Hajdu JB. Electroless Plating: Fundamentals and Applications: American Electroplaters and Surface Finishers Society, 1992.
101. Djokić SS. Electroless Deposition of Metals and Alloys. In: Conway BE, White RE, editors., vol. 35: Springer US, 2002. pp. 51-133.

102. Djokić SS, Cavallotti PL. Electroless Deposition: Theory and Applications. vol. 48: Springer New York, 2010. pp. 251-289.
103. Crossland EJW, Ludwigs S, Hillmyer MA, Steiner U. Soft Matter 2010;6(3):670-676.
104. Hsueh HY, Huang YC, Ho RM, Lai CH, Makida T, Hasegawa H. Adv Mater 2011;23(27):3041-3046.
105. Hakamada M, Mabuchi M. J Mater Res 2009;24(2):301-304.
106. Vignolini S, Yufa NA, Cunha PS, Guldin S, Rushkin I, Stefik M, et al. Adv Mater 2012;24(10):OP23-OP27.
107. Warren SC, Messina LC, Slaughter LS, Kamperman M, Zhou Q, Gruner SM, et al. Science 2008;320(5884):1748-1752.
108. Tyler CA, Morse DC. Physical Review Letters 2005;94(20):208302.
109. Finnefrock AC, Ulrich R, Toombes GE, Gruner SM, Wiesner U. J Am Chem Soc 2003;125(43):13084-13093.

Chapter 2

Nanoporous Gyroid Templates from P_tBOS-*b*-PS-*b*-P4VP(PDP) Supramolecules

Several supramolecular complexes based on poly(tert-butoxystyrene)-block-polystyrene-block-poly(4-vinylpyridine) (P_tBOS-b-PS-b-P4VP) triblock copolymer and low molecular weight pentadecylphenol (PDP) were found to self-assemble into a core-shell double gyroid morphology, with a P4VP(PDP) comb block forming the gyroid core channels. Subsequently, PDP molecules were selectively removed by dissolution in ethanol, and the resulting well-ordered porous templates were electroless nickel plated. The porosity of nanoporous structures can be tuned by varying the PDP content in starting supramolecular complexes.

Part of this chapter was published in: *Macromolecular Rapid Communications 2011, 32, 366-370.*

2.1 Introduction

As discussed in the previous chapter, block copolymers can microphase separate and self-assemble into a variety of nanostructures with periodicity of 10–100 nm.[1-3] The phase behavior of linear AB diblock copolymers is mainly dictated by three parameters: (1) the degree of polymerization, N, (2) the segment–segment interaction parameter, χ_{AB}, and (3) the composition, f. As the number of blocks in the copolymer increases, more parameters that influence the block copolymer phase behavior appear, and possibilities for novel, complex structures are created.[4-6] Three interaction parameters (χ_{AB}, χ_{BC}, χ_{AC}) and two independent composition variables (*e.g.*, f_A and f_B), along with the overall degree of polymerization, N, determine the morphology of ABC triblock copolymers. Furthermore, their phase behavior is strongly influenced by the block sequence and the chain architecture.

ABC triblock copolymers in which the A/C interface, where A and C represent non-covalently linked end blocks, is the most energetically unfavorable ($\chi_{AC} \gg \chi_{AB}$ and $\chi_{AC} \gg \chi_{BC}$), belong to the class of non-frustrated systems.[7] In such systems, A/C interfaces are not formed and morphologies similar to the diblock copolymer ones are found, such as alternating spheres, alternating cylinders, triple lamellae, *etc.*[8] If $\chi_{AC} \gg \chi_{AB} \gg \chi_{BC}$, the A/C interface is not formed, the A/B interface is minimized and more B/C contacts are created, which leads to core-shell type morphologies, such as core-shell spheres, core-shell cylinders, and core-shell gyroid.[5, 7, 9, 10] ABC triblock copolymers, in which χ_{AC} is smaller than one or even both interaction parameters, χ_{AB} and χ_{BC}, belong to the class of frustrated systems, and can adopt novel, intriguing morphologies, such as cylinders-between-lamellae, rings or helices around cylinders, cylinders in lamellae, *etc.*[11-14]

The phase behavior of ABC triblock copolymer poly(*tert*-butoxystyrene)-*block*-polystyrene-*block*-poly(4-vinylpyridine) has been studied in our group.[10] The interaction parameters were determined from random copolymer blend miscibility study: $0.39 < \chi_{AC} < 0.43$, $0.031 < \chi_{AB} < 0.034$, and $0.30 < \chi_{BC} < 0.35$, where A = P_tBOS, B = PS, and C = P4VP.[15, 16] All investigated samples of P_tBOS-*b*-PS-*b*-P4VP triblock copolymers were found to exhibit the core-shell type morphology (namely, core-shell cylinders), which is in agreement with the values of segment−segment interaction parameters ($\chi_{AC} > \chi_{BC} \gg \chi_{AB}$). Their phase behavior was altered with the addition of PDP, amphiphilic molecules that form hydrogen bonds with pyridine rings, leading to the formation of supramolecular complexes

P_tBOS-*b*-PS-*b*-P4VP(PDP)$_x$ (*x* denotes the ratio between the PDP molecules and P4VP monomer units).

In this chapter, we analyze the phase behavior of several complexes with less than stoichiometric amounts of PDP. The core-shell double gyroid morphology is detected. The gyroid network is composed out of P4VP(PDP)$_x$ core (orange) and PS (blue) corona while P_tBOS represents the matrix (green) (Figure 2.1a). PDP can be selectively removed by dissolution in ethanol, resulting in well-ordered porous structure (Figure 2.1b). The obtained porous structures were evaluated as templates for electroless metal deposition.

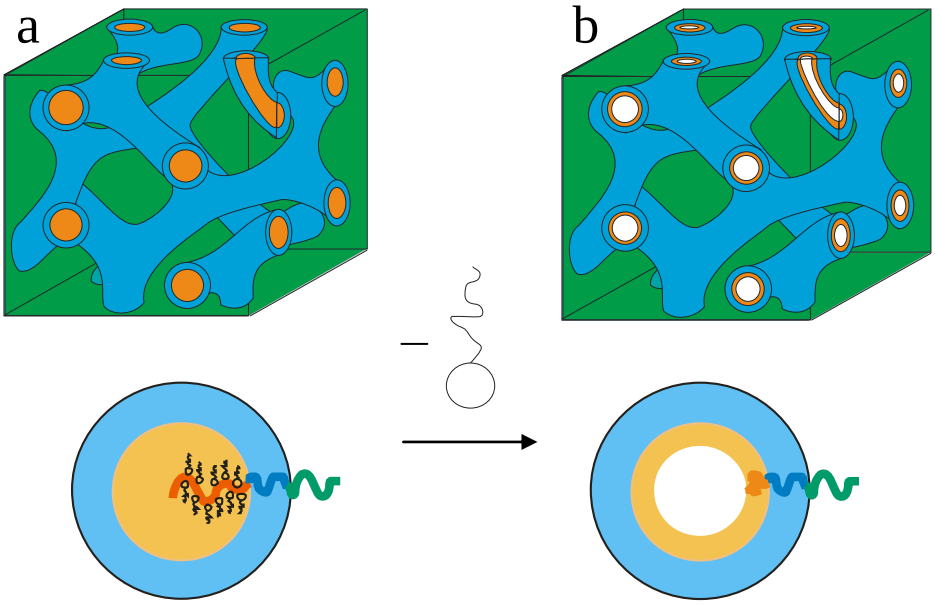

Figure 2.1. *Schematic representation of a) the core-shell double gyroid morphology in P_tBOS-b-PS-b-P4VP(PDP)$_x$ supramolecular complexes. The gyroid network consists of P4VP(PDP)$_x$ core (orange) and PS corona (blue) while the P_tBOS block represents the matrix (green), b) after the selective removal of PDP in ethanol, P4VP chains collapse onto the PS corona, resulting in a well-ordered nanoporous structure.*

2.2 Experimental section

2.2.1 Materials and sample preparation

Materials. Triblock copolymer poly(*tert*-butoxystyrene)-*block*-polystyrene-*block*-poly(4-vinylpyridine) was synthesized using a three-step sequential anionic polymerization in THF at −78 °C and it was kindly provided by Gerrit Gobius du Sart.[10] 3-Pentadecylphenol (PDP) was acquired from Sigma Aldrich (98 wt % purity) and it was recrystallized twice from petroleum ether. Tin chloride (Acros Organics, anhydrous, 98%), palladium chloride (Aldrich, 60% Pd basis), nickel sulfate (Aldrich, anhydrous, 99.99%), nickel chloride hexahydrate (Aldrich, ≥98%), lactic acid (Aldrich, 85%), citric acid trisodium salt (Sigma-Aldrich, anhydrous), glycolic acid (Aldrich, 99%), sodium hypophosphite monohydrate (Aldrich, ≥99%), borane dimethylamine complex (Aldrich, 97%) were used as received. The solvents were of analytical grade.

Preparation of nanoporous polymer films. Films of the supramolecular complexes were cast by dissolving the P_tBOS-*b*-PS-*b*-P4VP triblock copolymer and PDP in chloroform. The concentration of polymer was maintained below 2 wt % to ensure homogeneous complex formation, and the solution was stirred for a couple of hours at room temperature. Afterward, the solution was poured into a glass Petri dish, which was subsequently placed into a saturated chloroform atmosphere. Chloroform was allowed to evaporate slowly during several days at room temperature. Subsequently, the samples were heated at 130 °C for half an hour. The low molecular weight amphiphile was removed by stirring a piece of the film in ethanol for three days at room temperature resulting in the formation of the nanoporous template for metal deposition.

Electroless nickel plating. The electroless metal plating technique, that involved three steps, was employed for Ni deposition onto the polymer substrate.[17, 18] The first step was performed for surface sensitization. The nanoporous polymer film was immersed in an aqueous solution of tin chloride (0.1 M $SnCl_2$ / 0.1 M HCl) and the surface of the nanochannels adsorbed Sn^{2+}. After a thorough rinse with deionized water, the film was transferred into an aqueous solution of palladium chloride (0.0014 M $PdCl_2$ / 0.25 M HCl). In this step the surface was activated by a redox reaction in which the Sn^{2+} ions were oxidized to Sn^{4+} and at the same time the Pd^{2+} ions were reduced to metallic Pd. This metallic palladium was used as the catalyst for the reduction of Ni^{2+}. After a thorough rinse with

deionized water, Pd-containing films were immersed in an electroless nickel plating bath. Nickel plating was performed at high temperature (90 °C) and room temperature. The composition of high temperature nickel plating bath was: nickel chloride hexahydrate (Ni source, 30 g L^{-1}), glycolic acid (buffer, complexant, 35 g L^{-1}) and sodium hypophosphite monohydrate (reductant, 10 g L^{-1}). The pH was adjusted to 4.5 using sodium hydroxide. The composition of room temperature nickel plating bath was: nickel sulfate (Ni source, 40 g L^{-1}), sodium citrate (complexant, 20 g L^{-1}), lactic acid (buffer, complexant, 10 g L^{-1}) and dimethyl amine borane (DMAB) (reductant, 1 g L^{-1}). The pH of the nickel bath was adjusted to 7.0 using ammonium hydroxide. Plating was done during 1 hour.

2.2.2 Characterization methods

Transmission electron microscopy was performed on a Philips CM12 transmission electron microscope operating at an accelerating voltage of 120 kV. Images were recorded on a Gatan slow-scan CCD camera. A piece of the film was embedded in an epoxy resin (Epofix, Electron Microscopy Sciences) and cured overnight at 40°C. The sample was subsequently microtomed to a thickness of about 80 nm using a Leica Ultracut UCT-ultramicrotome and a Diatome diamond knife at room temperature. The microtomed sections were floated on water and subsequently placed on copper grids. To obtain contrast during TEM, samples without metal were stained with iodine (45 min).
Scanning Electron Microscopy was performed on a Philips XL-30S. Prior to imaging, specimens were coated with a few nanometer thick layer of platinum.
^{1}H-NMR spectra in $CDCl_3$ were recorded on a 300 MHz Varian VXR operating at room temperature. The samples of the supramolecular complexes before and after PDP removal were prepared by dissolution of a piece of the film in $CDCl_3$.
FT-IR measurements were carried out on a Bruker IFS88 spectrometer.
Mercury porosimetry was performed using a Carlo Erba 2000, software Milestone 200. The sample was dried at 50 ºC for 8 h and degassed at room temperature and pressure of 0.5 Pa for 2 h. The total pore volume, V_p, and the average pore diameter, D, were acquired from cumulative pore distribution curve. The specific surface area, S_{Hg}, was calculated on the basis of the cylindrical pore model.[19, 20]

2.3 Results and discussion

The block copolymer P_tBOS-*b*-PS-*b*-P4VP used in this study has the following characteristics: $f_{PtBOS} = f_{PS} = 0.46$, $f_{P4VP} = 0.08$, $M_n = 76\ 000$ g mol^{-1}, and $PDI = 1.04$, as determined by GPC and calculated according to the reaction stoichiometry. It self-assembles into the core-shell cylindrical morphology with the P4VP core cylinders, the hexagonally-shaped PS shell, and the P_tBOS matrix. The addition of the stoichiometric amount of PDP induces the formation of the complex P_tBOS-*b*-PS-*b*-P4VP(PDP)$_{1.0}$ ($f_{PtBOS} = f_{PS} = 0.373$, $f_{P4VP(PDP)} = 0.253$), with the triple lamellar structure.[10] If less than stoichiometric amounts of PDP are added, namely $0.3 \leq x \leq 0.8$, the complexes adopt the core-shell double gyroid morphology with the P4VP(PDP)$_x$ gyroid network core, the PS gyroid network shell, and the P_tBOS matrix (Figure 2.1a). The weight fractions of the investigated complexes are listed in Table 2.1. TEM images (Figure 2.2) display the characteristic gyroid double-wave patterns found in supramolecular complexes P_tBOS-*b*-PS-*b*-P4VP(PDP)$_x$, with $0.3 \leq x \leq 0.8$. The double-wave pattern represents the projection through the (211) plane of the gyroid unit cell. The P4VP(PDP)$_x$ blocks are selectively stained with iodine and appear dark in the images.

Table 2.1. *P_tBOS-b-PS-b-P4VP(PDP)$_x$ supramolecules used in this study*

x	f_{PtBOS}	f_{PS}	f_{P4VP}
0.3	0.430	0.430	0.140
0.4	0.421	0.421	0.158
0.5	0.412	0.412	0.175
0.6	0.404	0.404	0.192
0.7	0.396	0.396	0.208
0.8	0.388	0.388	0.224

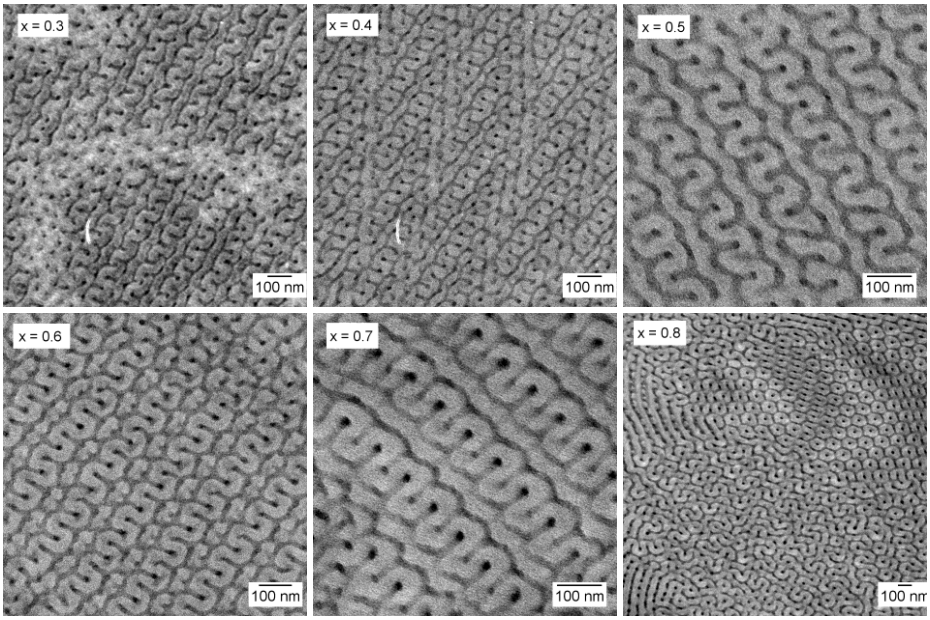

Figure 2.2. *TEM micrographs of P_tBOS-b-PS-b-P4VP(PDP)$_x$ supramolecular complexes, with $0.3 \leq x \leq 0.8$. The P4VP(PDP)$_x$ block appears dark since it is selectively stained with iodine. Displayed double-wave patterns represent projections through the (211) plane of the gyroid unit cell.*

When P_tBOS-*b*-PS-*b*-P4VP(PDP)$_x$ supramolecules are immersed in ethanol, PDP becomes dissolved and P4VP chains collapse onto the PS corona, resulting in the formation of the nanoporous gyroid structure (Figure 2.1b).

The complete removal of PDP in ethanol is proven by ^{1}H NMR (Figure 2.3). The spectrum of PDP is shown in Figure 2.3a ($CDCl_3$, δ, ppm: (a) 6.6–7.2 (4H, aromatic), (b) 2.55 (t, 2H, –PhCH_2–), (c) 1.2–1.6 (m, 26H, –CH_2–), (d) 0.88 (t, 3H, –CH_3). Figure 2.3c shows the spectrum of the representative supramolecular complex P_tBOS-*b*-PS-*b*-P4VP(PDP)$_{0.5}$. As expected, it is simply the sum of the PDP and the triblock copolymer (Figure 2.3b) spectra, and the characteristic PDP peaks (b, d) are visible. After the ethanol treatment, PDP peaks are absent and the spectrum of the triblock copolymer is recovered (Figure 2.3d). This indicates that the ethanol treatment results in the complete removal of PDP.

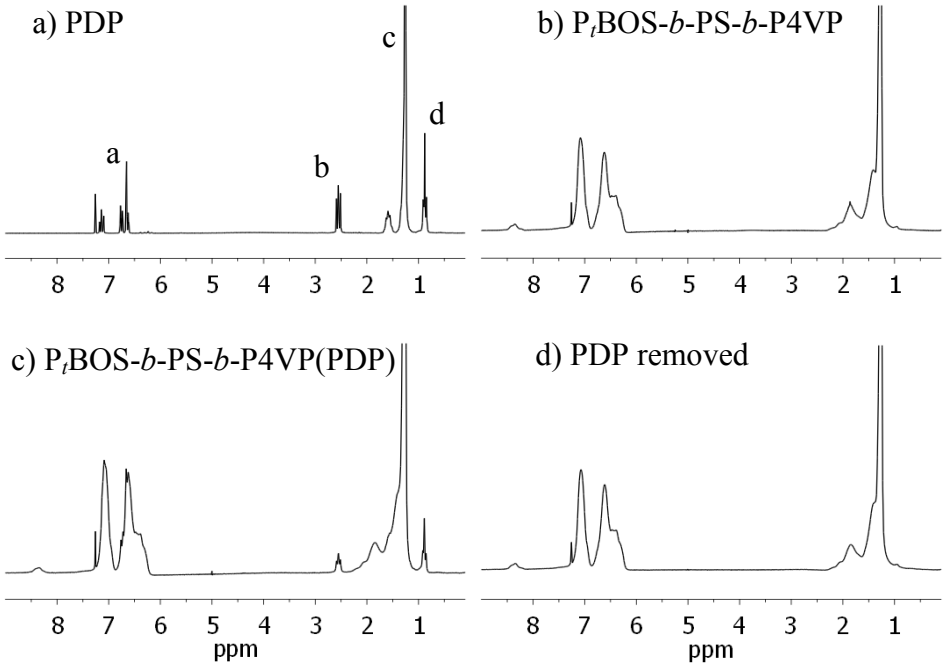

Figure 2.3. *^{1}H NMR spectra of a) PDP, b) P_tBOS-b-PS-b-P4VP triblock copolymer, c) P_tBOS-b-PS-b-P4VP(PDP)$_{0.5}$ supramolecular complex, and d) P_tBOS-b-PS-b-P4VP(PDP)$_{0.5}$ after washing with ethanol.*

Furthermore, the formation of hydrogen bonds in supramolecular complexes and their cleavage during the ethanol treatment is examined by FT-IR (Figure 2.4). The spectrum of the pure triblock copolymer contains the absorption band at 993 cm^{-1}, characteristic for the free pyridine ring vibration. After the complex formation between the P4VP block and PDP, this band shifts to the higher wavenumber, 1008cm^{-1}, which is characteristic for hydrogen-bonded pyridine groups.[21-23] After the ethanol treatment, the FT-IR spectrum of the pure triblock copolymer is recovered, indicating the complete cleavage of hydrogen bonds by ethanol washing.

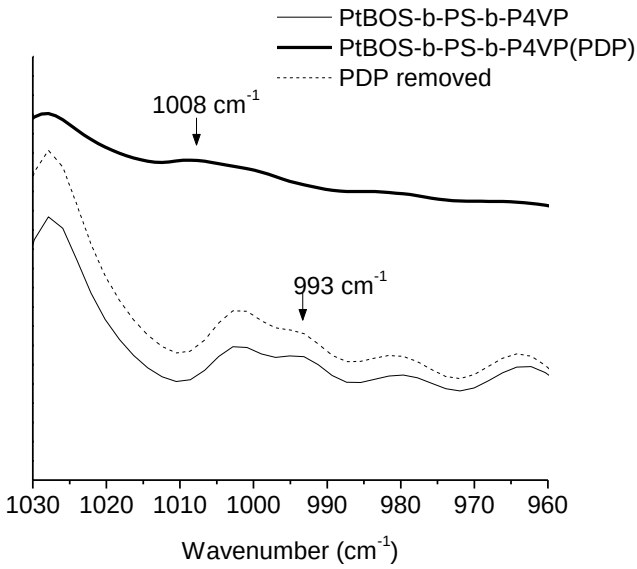

Figure 2.4. *FT-IR spectra of P_tBOS-b-PS-b-P4VP triblock copolymer (solid line), representative P_tBOS-b-PS-b-P4VP(PDP)$_{0.5}$ supramolecular complex (solid bold line), and P_tBOS-b-PS-b-P4VP(PDP)$_{0.5}$ after washing with ethanol (dashed line). The absorption band at 993 cm^{-1}, characteristic for the free pyridine ring vibration, shifts to 1008 cm^{-1} after the complex formation, and shifts back to 993 cm^{-1} after the ethanol treatment.*

The obtained nanoporous gyroid structure is visualized by SEM. Figure 2.5 shows the top view of the representative supramolecular complex P_tBOS-*b*-PS-*b*-P4VP(PDP)$_{0.3}$ after washing with ethanol. The SEM image after washing is clearly similar to the TEM image before washing (Figure 2.2).

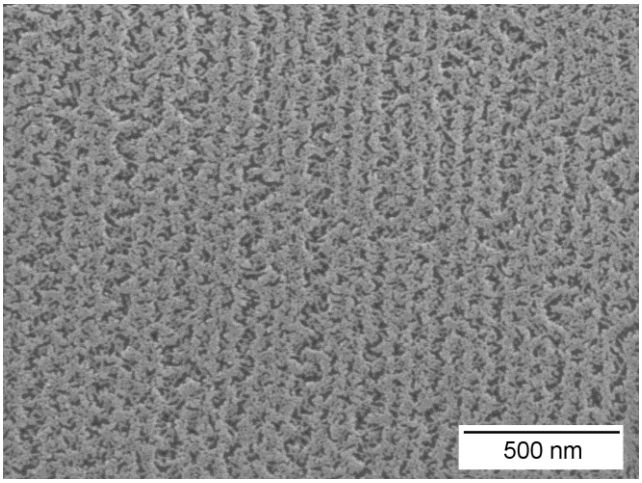

Figure 2.5. *SEM micrograph of the representative supramolecular complex P_tBOS-b-PS-b-P4VP(PDP)$_{0.3}$ after washing with ethanol.*

The textural properties of the obtained porous films are determined by mercury porosimetry. Data for the representative sample (x = 0.5) are given in Table 2.2. The expected textural properties are calculated assuming a double gyroid structure of the sample with 150 nm unit cell and a bulk density of 1 g cm^{-3}. The size of the gyroid unit cell is determined from the reported SAXS data.[24] The expected porosity is estimated as 10.38% on the basis of the amount of PDP originally present, and was used as input for the calculation of the mean pore diameter and the specific surface area. The mercury porosity measurements, when corrected for the presence of large defects give values that are presented in the last column. Excellent agreement between both sets of data is found. Since the core-shell double gyroid morphology is found in supramolecular complexes with different PDP content, namely $0.3 \leq x \leq 0.8$, the porosity of the structures obtained after the PDP removal can be tuned from 6.50 to 15.63%, as calculated.

Table 2.2. *Textural properties of the representative supramolecular complex P_tBOS-b-PS-b-P4VP(PDP)$_{0.5}$ after washing with ethanol.*

	Expected	**Porosimetry**
Total porosity, %	10.38	11.54
Pore volume, $mm^3\ g^{-1}$	103.8	115.4
Pore diameter average, nm	12.5	12
Specific surface area, $m^2\ g^{-1}$	24.4	30.8
Surface-to-volume ratio, m^{-1}	2.4×10^8	2.7×10^8

The obtained nanoporus gyroid films are further evaluated as templates for electroless metal deposition. Figure 2.6 shows TEM images of the representative electroless plated samples. The samples are not stained prior to imaging and the contrast results from nickel deposited in the nanochannels. Figures 2.6a and 2.6b represent the TEM images of the sample plated using high temperature nickel bath. As shown, channels located close to the surface are filled with nickel while ones in the middle of the film remain empty. Relatively high temperature of the plating bath (90 °C) could disturb the nanoporous structure and induce the closure of the template pores, and thus prevent the metal deposition throughout the whole template thickness. Therefore, we employ alternative plating procedure that is performed at room temperature. The TEM image of the sample plated at room temperature is represented in Figure 2.6c. As shown, the plating results are independent on the plating temperature, and in both described examples, nickel is deposited in the pores located only a couple of micrometers away from the surface. This seems to be induced by narrow channels of the template and the fast-growing nickel deposit near the free surface that hinders the reagents' diffusion towards the bulk.[25]

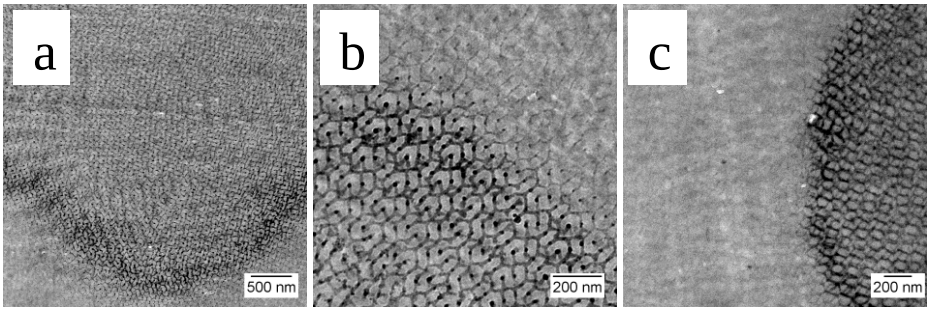

Figure 2.6. *TEM images of the unstained gyroid polymer templates nickel-plated using a, b) high temperature and c) room temperature nickel plating bath. The starting supramolecular complex is* P_tBOS*-b-PS-b-P4VP(PDP)*$_{0.5}$*.*

2.4 Conclusion

A core-shell double gyroid morphology is found in supramolecular complexes P_tBOS-*b*-PS-*b*-P4VP(PDP)$_x$ in a rather broad composition range, namely $0.3 \leq x \leq 0.8$, *i.e.*, $0.430 \geq f_{PtBOS}$, $f_{PS} \geq 0.388$ and $0.140 \leq f_{P4VP} \leq 0.224$. Hydrogen bonds between the P4VP block and PDP molecules can be cleaved in ethanol, leading to the formation of well-ordered nanoporous structures. The porosity of the obtained structures can be tuned from 6.50 to 15.63% (according to the calculations) by altering the PDP content in the starting supramolecular complex from $x = 0.3$ to $x = 0.8$. Via electroless plating technique, nickel can be inserted into the gyroid template nanochannels located a couple of micrometers away from the surface. However, plating of nanochannels located further away remains a challenge.

2.5 References

1. Bates FS, Fredrickson GH. Annu Rev Phys Chem 1990;41:525-527.
2. Hamley IW. The Physics of Block Copolymers. Oxford: Oxford University Press, 1998.
3. Abetz V, Simon P. Phase Behaviour and Morphologies of Block Copolymers. Adv Polym Sci, vol. 189: Springer Berlin / Heidelberg, 2005. pp. 125-212.
4. Bates FS, Fredrickson GH. Phys Today 1999;52:32-38.
5. Epps TH, Cochran EW, Bailey TS, Waletzko RS, Hardy CM, Bates FS. Macromolecules 2004;37(22):8325-8341.
6. Tyler CA, Qin J, Bates FS, Morse DC. Macromolecules 2007;40(13):4654-4668.
7. Bailey TS, Pham HD, Bates FS. Macromolecules 2001;34(20):6994-7008.
8. Mogi Y, Nomura M, Kotsuji H, Ohnishi K, Matsushita Y, Noda I. Macromolecules 1994;27(23):6755-6760.
9. Hückstädt H, Göpfert A, Abetz V. Polymer 2000;41(26):9089-9094.
10. Gobius du Sart G, Vukovic I, Alberda van Ekenstein G, Polushkin E, Loos K, ten Brinke G. Macromolecules 2010;43(6):2970-2980.
11. Breiner U, Krappe U, Thomas EL, Stadler R. Macromolecules 1998;31(1):135-141.
12. Breiner U, Krappe U, Jakob T, Abetz V, Stadler R. Polymer Bulletin 1998;40(2-3):219-226.
13. Balsamo V, von Gyldenfeldt F, Stadler R. Macromolecules 1999;32(4):1226-1232.
14. Abetz V, Goldacker T. Macromol Rapid Commun 2000;21(1):16-34.
15. van Ekenstein AGOR, Meyboom R, ten Brinke G, Ikkala O. Macromolecules 2000;33(10):3752-3756.
16. Gobius du Sart G. Supramolecular Triblock Copolymer Complexes. University of Groningen, 2009.
17. Riedel W. Electroless Nickel Plating. Finishing Publications: Metals Park, 1991.
18. Mallory GO, Hajdu JB. Electroless Plating: Fundamentals and Applications: American Electroplaters and Surface Finishers Society, 1992.

19. Webb PA, Orr C. Analytical Methods in Fine Particle Technology Norcross, GA: Micrometrics Instrument Corporation, 1997.
20. Leofanti G, Padovan M, Tozzola G, Venturelli B. Catal Today 1998;41:207-219.
21. Ruokolainen J, ten Brinke G, Ikkala O, Torkkeli M, Serimaa R. Macromolecules 1996;29(10):3409-3415.
22. Ruokolainen J, Saariaho M, Ikkala O, ten Brinke G, Thomas EL, Torkkeli M, et al. Macromolecules 1999;32(4):1152-1158.
23. Fahmi A, Adam G, Stamm M. J Mol Struct 2003;661-662:161-170.
24. Gobius du Sart G, Vukovic I, Vukovic Z, Polushkin E, Hiekkataipale P, Ruokolainen J, et al. Macromol Rapid Commun 2011;32(4):366-370.
25. Boontongkong Y, Cohen RE, Rubner MF. Chem Mater 2000;12(6):1628-1633.

Chapter 3

Double Gyroid Network Morphology in PS-*b*-P4VP(PDP) Supramolecules

The double gyroid network morphology has been the focus of extensive research efforts as one of the most appealing block copolymer structures for practical applications. We performed an extensive study of the phase behavior of the supramolecular complex PS-b-P4VP(PDP)$_x$ to develop a systematic route to its double gyroid morphology. The morphological characterization of complexes was accomplished by transmission electron microscopy (TEM) and small-angle X-ray scattering (SAXS). Several compositions with the cubic Ia3d symmetry were found in a narrow region between the lamellar and the cylindrical phase. Experimental TEM images were compared to computer simulations of projections through multiple gyroid planes. Typical gyroid patterns – "double wave" and "wagon wheel" – were regularly found. The size of the gyroid unit cell was calculated from the SAXS data. The lattice parameter could be varied (from ca. 70 nm to 125 nm) by altering the molar mass of the block copolymer precursors. A number of complexes were found to exhibit characteristic biphasic morphologies – coexisting lamellar and gyroid phase or gyroid and cylindrical phase. Finally, gyroid complexes with different relative PDP ratios were obtained which provides the opportunity to generate nanoporous structures with tunable porosities by dissolving the amphiphiles.

Part of this chapter was published in: *Macromolecules 2012, 45, 3503-3512.*

3.1 Introduction

Self-assembly in block copolymers has attracted a lot of attention since the development of living anionic polymerisation[1] and the subsequent experimental discovery of ordered mesostructures in the simplest linear AB diblock copolymers.[2-6] As already mentioned in the first chapter, more complex systems such as triblock and multiblock copolymers, star-type and graft-type copolymers, blends of block copolymers with homopolymers, *etc.*, are found to exhibit a broad variety of novel morphologies.[7-13]

The bicontinuous gyroid morphology has captivated researchers due to a wide range of possible technological applications, such as hybrid solar cells,[14] antireflection structures,[15] photonic crystals,[16] optical metamaterials,[17] *etc.* In comparison to classical phases (body centered cubic spheres (BCC), hexagonally ordered cylinders (CYL) and lamellae (LAM)), a bicontinuous gyroid morphology appears over a narrow range of the copolymer composition f in the diblock copolymer phase diagram. It is mostly found in the weak-to-intermediate segregation regime ($10 < \chi N < 40$), and its region in the phase diagram gradually contracts as χN increases, possibly due to the packing frustration induced by narrowing interfaces in the strong segregation regime.[18] Therefore, careful selection of the block copolymer system parameters is required to target the gyroid region of the phase diagram. Another challenge that is of crucial importance for certain applications is the ability to control the domain size in the gyroid unit cell. For instance, interdomain spacing of several hundreds of nanometers is required for a visible-light photonic crystal[16] while it should be comparable to the exciton diffusion length (~10 nm) for a hybrid solar cell application.[14]

Addition of another component to a block copolymer alters its phase behavior and can affect the appearance of new equilibrium morphologies, particularly between LAM and CYL phases.[19-21] Studies of the phase behavior of diblock copolymer/homopolymer blends have shown that bicontinuous phases can be stabilized by the presence of the homopolymer.[22, 23] The previous chapter describes another example where the appearance of the core–shell double gyroid morphology is influenced by the addition of amphiphilic molecule PDP (pentadecylphenol) to the triblock copolymer P*t*BOS-*b*-PS-*b*-P4VP (poly(*tert*-butoxystyrene)-*b*-polystyrene-*b*-poly(4-vinylpyridine)).[24] Moreover, it is

possible to tailor the morphology of the system in a simple fashion by varying the relative fraction of the additional component and thus saving the effort of synthesizing a block copolymer to achieve the desired morphology.[25] In this chapter we focus on the formation of the double gyroid network morphology in supramolecular complexes of amphiphilic PDP and PS-*b*-P4VP (polystyrene-*b*-poly(4-vinylpyridine)) diblock copolymers. As described before, PDP molecules interact via hydrogen bonds with pyridine rings to form PS-*b*-P4VP(PDP)$_x$ complexes (*x* denotes the ratio between PDP molecules and P4VP repeat units). The amphiphiles can be removed in a selective solvent to generate nanoporous structures.[26, 27] If the nanoporous material has a continuous morphology, the critical alignment issue is overcome which provides the opportunity for several applications, such as membranes,[28] templates for inorganic materials, *etc*.[14, 15, 17, 29, 30]

In the study of the phase diagram of the PS-*b*-P4VP(PDP)$_{1.0}$ complex, Valkama *et al*. have reported the formation of the double gyroid morphology in a sample with the weight fraction of PS (f_{PS}) 0.38 and the total molar mass (including PDP) 83 300 g mol^{-1}. When the total molar mass was increased to 129 000 g mol^{-1}, while f_{PS} was maintained constant, the complex adopted a lamellar morphology. The same behavior was noticed with the further increase of the total molar mass of the complex.[31] For the present study we prepared a large number of different PS-*b*-P4VP(PDP)$_x$ samples to systematically study the phase behavior of the supramolecular system in the region of the phase diagram in which the double gyroid morphology was expected. The systems investigated were divided into three groups according to the ratio between the molar mass of the PS block and the P4VP block in the starting block copolymer (this ratio is designated as *r*). Figure 3.1 schematically presents the block copolymer precursors and the corresponding supramolecular complexes from groups 1, 2, and 3. Ratios *r* for groups 1, 2, and 3 were chosen such that double gyroid morphologies in supramolecular complexes, formed upon the addition of PDP, were expected for $x = 1.0$, $x < 1.0$, and $x > 1.0$, respectively. In each group, *r* was maintained relatively constant while the molar masses of the PS-*b*-P4VP block copolymers were altered which allowed us to move vertically in the phase diagram. Additionally, by adjusting the amount of PDP, the weight fractions of the blocks in the supramolecular complexes were changed and we could move along the *x*-axis in the phase diagram. Our aim was to

understand which parameter values of the system give rise to the gyroid morphology, how can we tune the size of the gyroid unit cell as well as the porosity of the nanoporous gyroid templates, and what are the possible limitations in terms of the molar masses of the starting block copolymers and the size of the structures obtained.

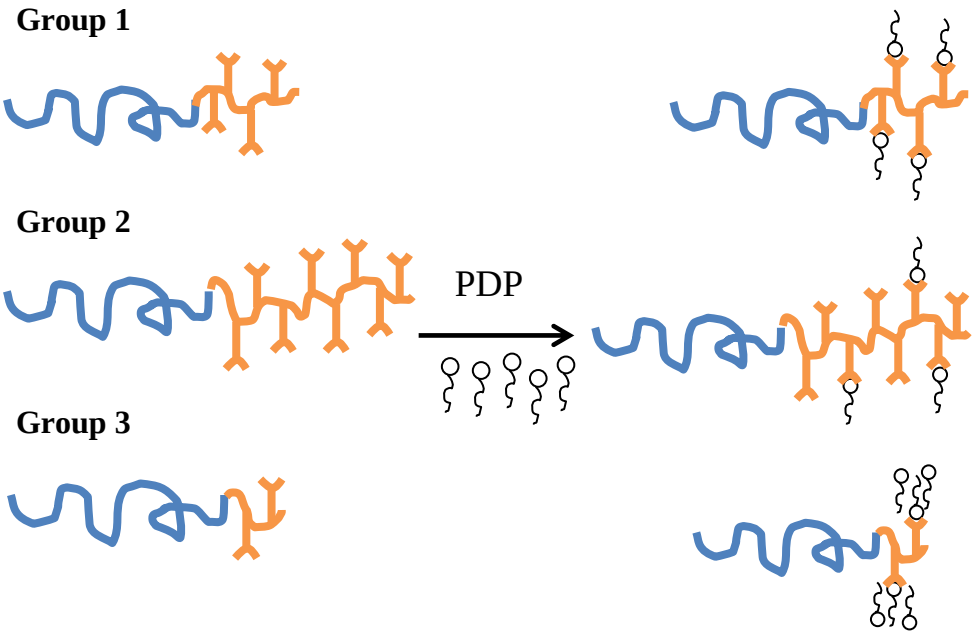

Figure 3.1. *Schematic representation of the block copolymer precursors and the corresponding supramolecular complexes from groups 1, 2, and 3. Ratios r (r = M_n(PS) / M_n(P4VP)) for groups 1, 2, and 3 are r ≅ 2.45, r < 2.45, and r > 2.45, respectively. The double gyroid morphology of the final supramolecular complex is expected for a comb block weight fraction f(P4VP(PDP)$_x$) of ca. 0.62.[31] To achieve this, different relative amounts x of PDP have to be added to the block copolymer precursors from groups 1, 2, and 3: x ≅ 1.0, x < 1.0, and x > 1.0, respectively.*

3.2 Experimental section

3.2.1 Materials and sample preparation

Materials. Diblock copolymers of polystyrene and poly(4-vinylpyridine) were obtained from Polymer Source Inc. The properties of the diblock copolymers studied are listed in Table 3.1. The polymers were used as received. 3-Pentadecylphenol (PDP) was acquired from Sigma Aldrich (98 wt % purity) and was recrystallized twice from petroleum ether. Chloroform (*p.a.*, LAB-SCAN) was used as received.

Preparation of the polymer films. Films of the supramolecular complexes were cast by dissolving the PS-*b*-P4VP diblock copolymer and PDP in chloroform. The concentration of polymer was maintained below 2 wt % to ensure homogeneous complex formation, and the solution was stirred for a couple of hours at room temperature. Afterward, the solution was poured into a glass Petri dish, which was subsequently placed into a saturated chloroform atmosphere. Chloroform was allowed to evaporate slowly during several days at room temperature. Subsequently, the samples were dried in vacuum at 30 °C overnight and annealed several days at 120 °C under N_2 atmosphere with 1 bar overpressure to make sure that the morphology represents the equilibrium structure of the melt state of the PS-*b*-P4VP(PDP) complex. Finally, samples were slowly cooled down to room temperature.

3.2.2 Characterization methods

Transmission electron microscopy was performed on a Philips CM12 transmission electron microscope operating at an accelerating voltage of 120 kV. Images were recorded on a Gatan slow-scan CCD camera. Samples for TEM were prepared according to the procedure described in chapter 2. A piece of the film was embedded in an epoxy resin, microtomed and then, the sections of about 80 nm thickness were placed on copper grids. To obtain contrast for TEM, the samples were stained with iodine (45 min).

Small-angle X-ray scattering (SAXS) was performed on two different setups. The first one was at the Dutch–Belgian Beamline (DUBBLE) station BM26B of the

European Synchrotron Radiation Facility (ESRF) in Grenoble (France). The sample-to-detector distance was *ca.* 5 m with a wavelength of 1.033 Å. A Dectris-Pilatus 1 M detector with a resolution of 981 × 1043 pixels and a pixel size of 172 × 172 μm has been employed to record the 2D–SAXS scattering patterns. Standard corrections for sample absorption and background subtraction have been performed. The data were normalized with respect to the incident beam intensity in order to correct for primary beam intensity fluctuations. The scattering patterns from rat tail were used for the calibration of the wave vector scale of the scattering curve. The SAXS patterns were acquired at room temperature. The scattering vector q is defined as $q = 4\pi/\lambda \, (\sin \theta)$ with 2θ being the scattering angle.[32, 33]

In situ shearing was performed using a parallel plate shear cell obtained from Linkam.

The second setup was on the SAXS device in the Nanomicroscopy Center at the Aalto University that consists of a Bruker MICROSTAR microfocus rotating anode X-ray source with Montel Optics (parallel beam, Cu K_α radiation $\lambda = 1.54$ Å), where the beam was further collimated using three sets of JJ X-ray 4-blade slits. A sample-to-detector distance of 4.64 m was used. The scattering intensities were measured using a 2D area detector (Bruker HiStar). The samples were measured at room temperature in vacuum.

Table 3.1. *Properties of the diblock copolymers PS-b-P4VP used in this study.*[a]

sample code	M_n(PS), g mol^{-1}	M_n(P4VP), g mol^{-1}	*r*	PDI
Group 1				
S4VP-33.5k-1	24 000	9 500	2.53	1.10
S4VP-45.1k-1	31 900	13 200	2.42	1.08
S4VP-53.5k-1	37 500	16 000	2.34	1.30
S4VP-68.3k-1	48 000	20 300	2.36	1.13
Group 2				
S4VP-21.5k-2	12 000	9 500	1.26	1.09
S4VP-43.5k-2	27 000	16 500	1.64	1.15
S4VP-56.0k-2	35 000	21 000	1.67	1.09
S4VP-65.0k-2	41 000	24 000	1.71	1.09
Group 3				
S4VP-15.0k-3	11 000	4 000	2.75	1.09
S4VP-32.0k-3	25 000	7 000	3.57	1.10
S4VP-67.0k-3	50 000	17 000	2.94	1.15

[a]*The division into three groups is made according to the ratio r between the molar masses of the PS and the P4VP block. The first number in the sample code denotes the total molar mass of the PS-b-P4VP block copolymer, and the second number denotes the group to which it belongs.*

3.3 Results and discussion

The weight fraction *f* of the comb block P4VP(PDP)$_x$ in the supramolecular PS-*b*-P4VP(PDP)$_x$ complex is related to the mass *m* of the different constituents by

$$f\ P4VP\ PDP\ = \frac{m\ PDP\ + m(P4VP)}{m\ PDP\ + m\ P4VP\ + m(PS)} \quad (3.1)$$

The mass of PDP can be expressed as

$$m\ PDP\ = \frac{m\ P4VP}{105\ g/mol} \times x \times\ 304\ g/mol \cong 3x \times m\ P4VP \quad 3.2$$

Hence,

$$f\ P4VP\ PDP\ \cong \frac{3x+1}{3x+1+r} \quad (3.3)$$

Taking previous experimental results into account,[31] the double gyroid morphology is expected in complexes with a weight fraction of the comblike P4VP(PDP)$_x$ block of *ca.* 0.62.

3.3.1 Morphological characterization of the PS-*b*-P4VP(PDP)$_x$ samples from group 1

When a stoichiometric ratio between PDP molecules and P4VP monomer units (x = 1.0) is aimed for, block copolymers with a ratio *r* between molar masses of PS and P4VP block of ca. 2.45 should be used as precursors for the preparation of supramolecular complexes with potentially double gyroid morphology. The polymers of group 1 (Table 3.1) have been selected accordingly.

As reported before, our SAXS and TEM investigations confirm that the supramolecular complex PS-*b*-P4VP(PDP)$_{1.0}$ (f_{PS} = 0.38, M_{total} = 83300 g mol^{-1})[31] prepared from S4VP-45.1k-1 (M_n(PS) = 31 900 g mol^{-1}, M_n(P4VP) = 13 200 g mol^{-1}) forms a double gyroid morphology. Bright-field TEM images

representing projections through the (111), (110), and (211) planes of the gyroid unit cell are presented in Figures 3.2a, 3.2b, and 3.2c, respectively. The PS domains appear bright while the $P4VP(PDP)_{1.0}$ domains appear dark due to the iodine staining. Computer-simulated projections (Figures 3.2d, 3.2e, and 3.2f) of cross sections, cut parallel to (111), (110), and (211) gyroid planes, respectively, are obtained by TEMsim[34] and show a good agreement with the experimental data. The typical gyroid patterns, the "wagon wheel" (Figures 3.2a and 3.2d) and the "double wave" pattern (Figures 3.2c and 3.2f), confirm the morphological assignment. SAXS analysis (Figure 3.3) of the sample supports the TEM data. The first two reflections are positioned in the q ratio $\sqrt{6}:\sqrt{8}$, and they are attributed to the (211) and (220) spacings of the double gyroid morphology. The intensity ratio 10:1 between the first two peaks is a good indication of the bicontinuous *Ia3d* morphology (as discussed in the literature).[3] The first intensity maximum is centered at $q = 0.199$ nm^{-1} corresponding to the d_{211} spacing equal to 31.6 nm and the lattice parameter a of 77.3 nm ($a = \sqrt{6}d_{211}$). Higher order gyroid peaks, although with relatively low intensity, are readily visible in the SAXS pattern (Figure 3.3). A peak centered at $q = 1.58$ nm^{-1} corresponds to lamellar structures with the lamellar period of 4 nm, formed in the comblike $P4VP(PDP)_{1.0}$ complex due to the microphase separation between the nonpolar PDP alkyl tails and the polar backbone.[35]

The block copolymer S4VP-33.5k-1 (M_n(PS) = 24 000 g mol^{-1}, M_n(P4VP) = 9 500 g mol^{-1}) with shorter blocks but similar ratio between the molar masses of the PS and P4VP blocks is used to prepare a set of supramolecular samples by systematically changing the amount of PDP from 0.5 to 1.7, thus reducing f_{PS} from 0.51 to 0.30. As a function of x, the morphology of the complex changes along the pathway LAM ($0.5 \leq x \leq 0.8$) → GYR ($0.9 \leq x \leq 1.0$) → CYL ($1.1 \leq x \leq 1.7$). Figure 3.4 shows representative TEM images. Well-aligned lamellae of the sample with $x = 0.7$ are shown in Figure 3.4a. Figure 3.4b presents the projection through the (110) plane of the gyroid sample ($x = 1.0$), and hexagonally ordered cylinders of the sample with $x = 1.3$ are depicted in Figure 3.4c. The bicontinuous *Ia3d* morphology is found in the composition range $\Delta f_{PS} \geq 0.02$ ($f_{PS} = 0.41$ for $x = 0.9$ and $f_{PS} = 0.39$ for $x = 1.0$). SAXS patterns of two gyroid samples from this range are shown in Figure 3.5. The q ratios of $\sqrt{6}:\sqrt{8}$ and intensity ratios of nearly 10:1 between the first two reflections represent an unambiguous signature of the double

gyroid morphology. The first-order reflections are equally positioned for both samples at q = 0.216 nm^{-1}, indicating the size of the unit cells to be 71.2 nm. This implies that the small variation of the PDP amount does not affect the size of the unit cell which can be exploited for the preparation of porous templates with the same interdomain spacing but somewhat different porosity. As calculated, the porosity of the templates prepared from these particular complexes can be varied from 42.5% to 45.1%. However, the size of the gyroid unit cell is influenced by the total molar mass of the starting copolymer, which allows us to adjust the lattice parameter by varying the molar mass of the block copolymer precursor.

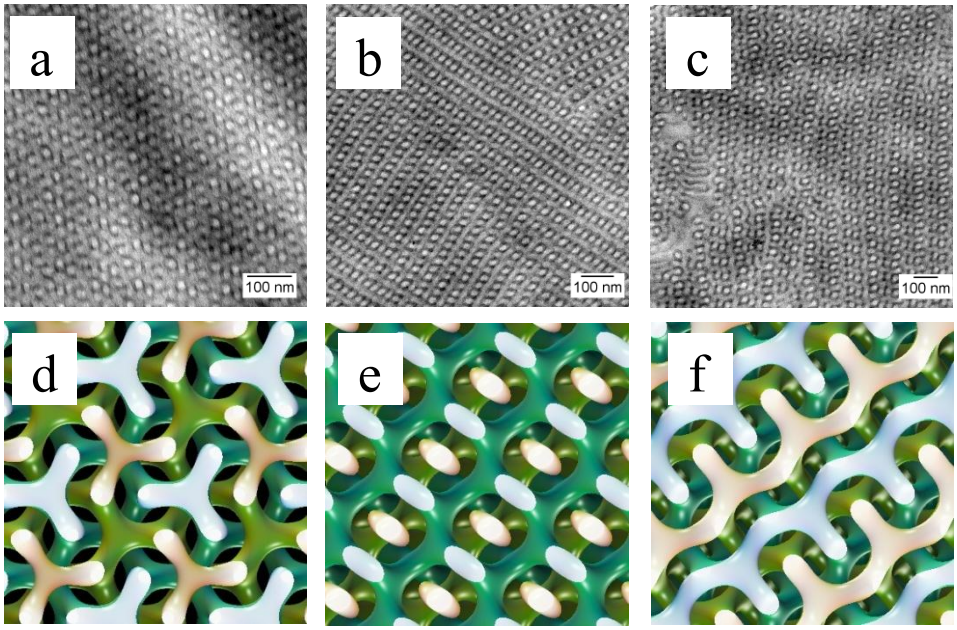

Figure 3.2. *Bright-field TEM images of PS-b-P4VP(PDP)$_{1.0}$, f_{PS} = 0.38, M_{total} = 83300 g mol^{-1} based on S4VP-45.1k-1; panels a, b, and c represent projections through the (111), (110), and (211) gyroid planes, respectively. TEM simulations of the (111), (110), and (211) planes are given in panels d, e, and f, respectively, as a comparison to experimental data.[34]*

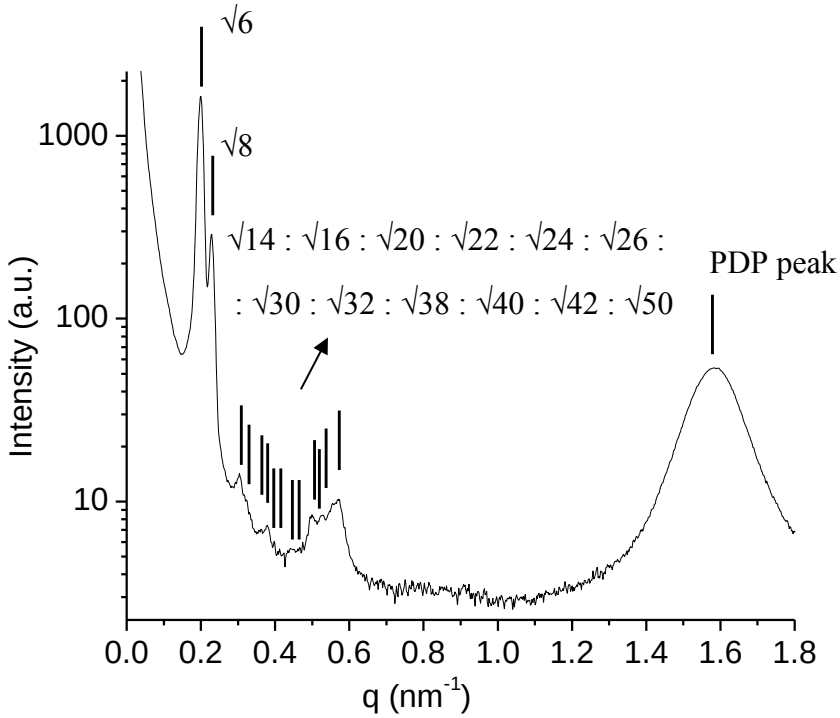

Figure 3.3. *SAXS pattern of PS-b-P4VP(PDP)$_{1.0}$, f_{PS} = 0.38, M_{total} = 83300 g mol^{-1} based on S4VP-45.1k-1. Lines indicate the expected reflections for the gyroid phase (cubic Ia3d symmetry), and they are positioned in the ratio √6:√8:√14:√16:√20:√22:√24:√26:√30:√32:√38:√40:√42:√50. The reflection at q = 1.58 nm^{-1} corresponds to the lamellar self-assembly within the P4VP(PDP)$_{1.0}$ domains.*

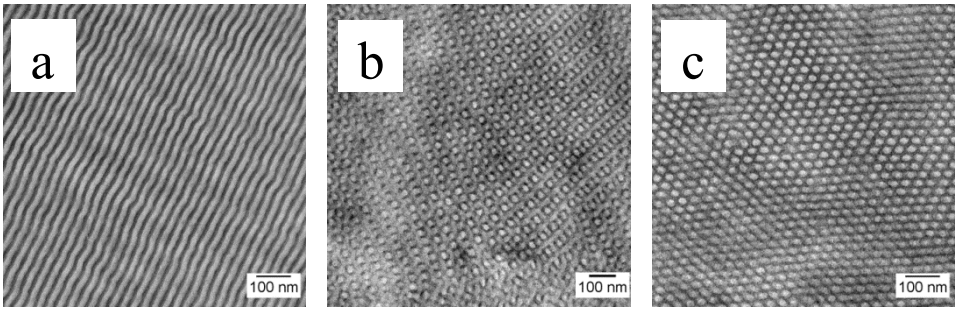

Figure 3.4. *Bright-field TEM images of PS-b-P4VP(PDP)$_x$ complexes prepared from the diblock copolymer S4VP-33.5k-1 with x values of (a) 0.7, (b) 1.0, and (c) 1.3.*

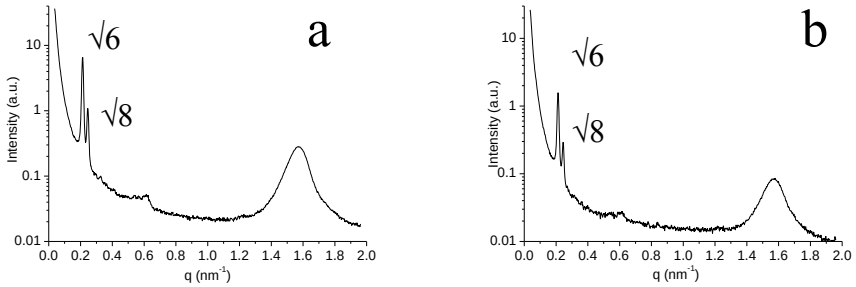

Figure 3.5. *SAXS patterns of PS-b-P4VP(PDP)$_x$ complexes with a double gyroid morphology. The samples are prepared from the diblock copolymer S4VP-33.5k-1 and have x = (a) 0.9 and (b) 1.0.*

To further investigate the phase behavior of the supramolecular complex PS-*b*-P4VP(PDP)$_x$, another set of samples is prepared starting from the diblock copolymer with longer blocks S4VP-53.5k-1 (M_n(PS) = 37 500 g mol^{-1}, M_n(P4VP) = 16 000 g mol^{-1}). The PDP content is varied from x = 0.5 to x = 1.5, which implies a change in the weight fraction of the PS block from 0.49 to 0.30. The morphology of the complexes changes as follows: LAM ($0.5 \leq x \leq 0.6$) → LAM + GYR (x = 0.7) → GYR (x = 0.8) → GYR + CYL (x = 0.9) → CYL ($1.0 \leq x \leq 1.5$). Bright-

field TEM images of several representative samples are given in Figure 3.6. Equally thick alternating PS and P4VP(PDP) lamellae of the sample with $x = 0.6$ are shown in Figure 3.6a, the gyroid "double wave" pattern of the sample with $x = 0.8$ is depicted in Figure 3.6c, and hexagonally packed cylinders of the sample with $x = 1.0$ are represented in Figure 3.6e. Additionally, biphasic morphologies appear as transitional phases between the lamellar and the gyroid phase (Figure 3.6b, sample with $x = 0.7$), as well as between the gyroid and the cylindrical phase (Figure 3.6d, sample with $x = 0.9$). Biphasic morphologies do not really come as a surprise since theoretical studies on related supramolecular diblock copolymers show their presence in the phase diagram due to the supramolecular nature of the system.[36, 37] Grain boundaries between the two coexisting phases can be easily observed in the TEM images. The double gyroid morphology is confirmed in one sample ($x = 0.8$), and if a slight horizontal move to any side in the phase diagram is made (to $x = 0.7$ or $x = 0.9$), the complexes enter the biphasic region. If this is compared with the previously discussed results (Figures 3.4 and 3.5), we notice a contraction of the gyroid region with an increase of the molar mass of the block copolymer precursor, as in the case of simple diblock copolymers.[18] The phase behavior of the complexes is further examined by SAXS. The first-order reflection of the lamellar sample (Figure 3.7) appears at $q^* = 0.148$ nm^{-1} (hence, lamellar period is 42.4 nm), and another reflection is found at the position $3q^*$. Even-order reflections ($2q^*$, $4q^*$, $6q^*$, *etc.*) are absent due to the symmetry of the alternating lamellae having equal thickness.[38] In the SAXS pattern of the gyroid sample, the peaks are found at the following positions: $\sqrt{6}q^*$, $\sqrt{8}q^*$, $\sqrt{14}q^*$, $\sqrt{22}q^*$, and $\sqrt{50}q^*$ as indicated with arrows. The first reflection of the gyroid sample coincides with the first reflection of the lamellar sample, implying the size of the gyroid unit cell to be 104 nm. The SAXS pattern of the sample with a coexisting lamellar and gyroid phase is also shown in Figure 3.7 and it is expected to represent a superposition of the former two patterns. The $\sqrt{6}$:$\sqrt{8}$ q ratio between the first two reflections and higher order peaks indicated with arrows confirm the existence of the double gyroid regions in the sample. It is rather difficult to confirm the presence of the lamellar phase from SAXS results, since the $3q^*$ lamellar peak would be the only signal to contribute to the SAXS pattern, and it is positioned closely to the gyroid $\sqrt{50}q^*$ peak. The first peak in the SAXS pattern of the cylindrical sample (Figure 3.8) is centered at $q^* = 0.131$ nm^{-1} (hence, the calculated distance between the

cylinders is 55.4 nm), and higher order peaks positioned at $\sqrt{4}q^*$ and $\sqrt{7}q^*$ confirm the morphological assignment. An identical SAXS pattern with well-defined higher order cylindrical peaks is found in the sample with a coexisting cylindrical and gyroid phase. The absence of gyroid peaks in the biphasic sample could imply that the cylinders represent the majority phase or that the gyroid phase has a low degree of ordering. To better resolve the first two reflections, the gyroid sample was measured for 90 h (Figure 3.9). Two signals positioned in the q ratio $\sqrt{6}$:$\sqrt{8}$ (q_1 = 0.148 nm^{-1} and q_2 = 0.171 nm^{-1}) can be clearly observed.

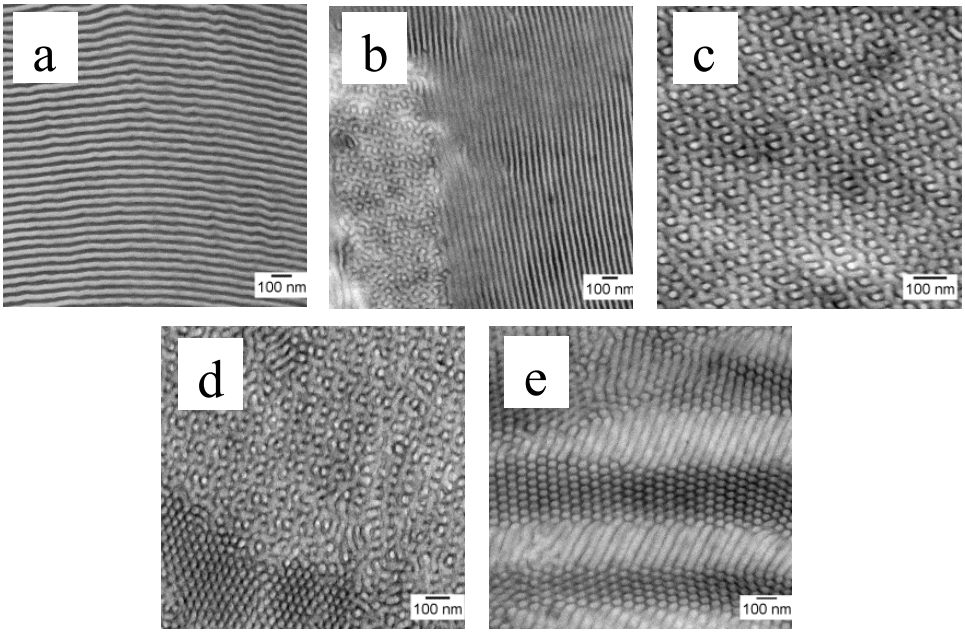

Figure 3.6. *Bright-field TEM images of PS-b-P4VP(PDP)$_x$ complexes prepared from the diblock copolymer S4VP-53.5k-1 with x values of (a) 0.6, (b) 0.7, (c) 0.8, (d) 0.9, and (e) 1.0.*

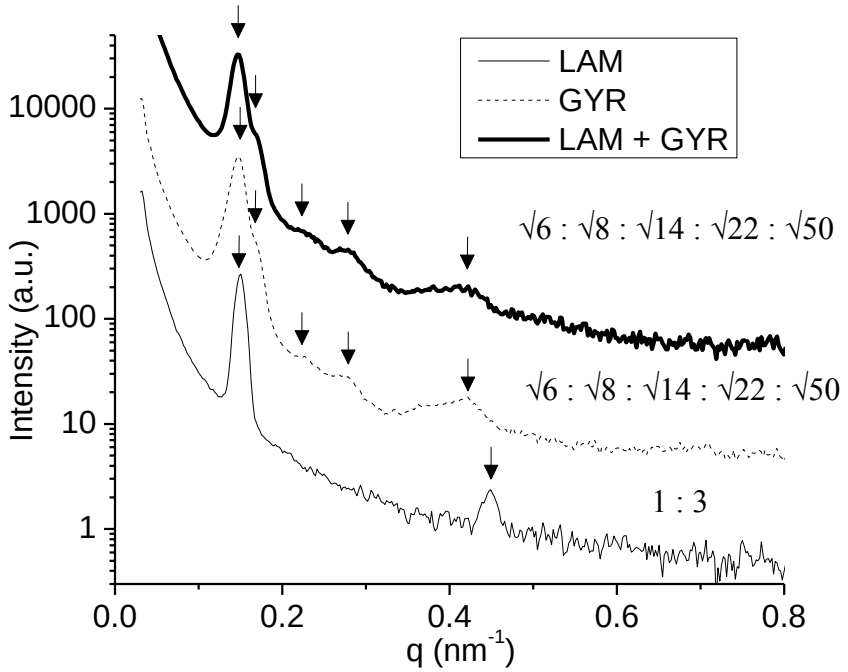

Figure 3.7. *SAXS patterns of PS-b-P4VP(PDP)$_x$ complexes prepared from the diblock copolymer S4VP-53.5k-1 with x = 0.6 (solid line), x = 0.7 (solid bold line), and x = 0.8 (dashed line).*

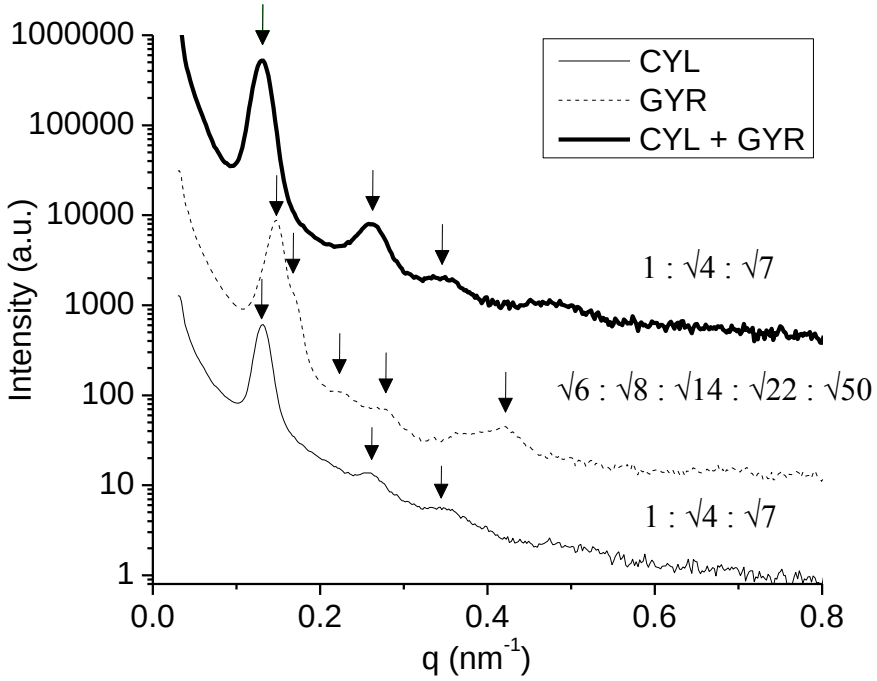

Figure 3.8. *SAXS patterns of PS-b-P4VP(PDP)$_x$ complexes prepared from the diblock copolymer S4VP-53.5k-1 with x = 0.8 (dashed line), x = 0.9 (solid bold line), and x = 1.0 (solid line).*

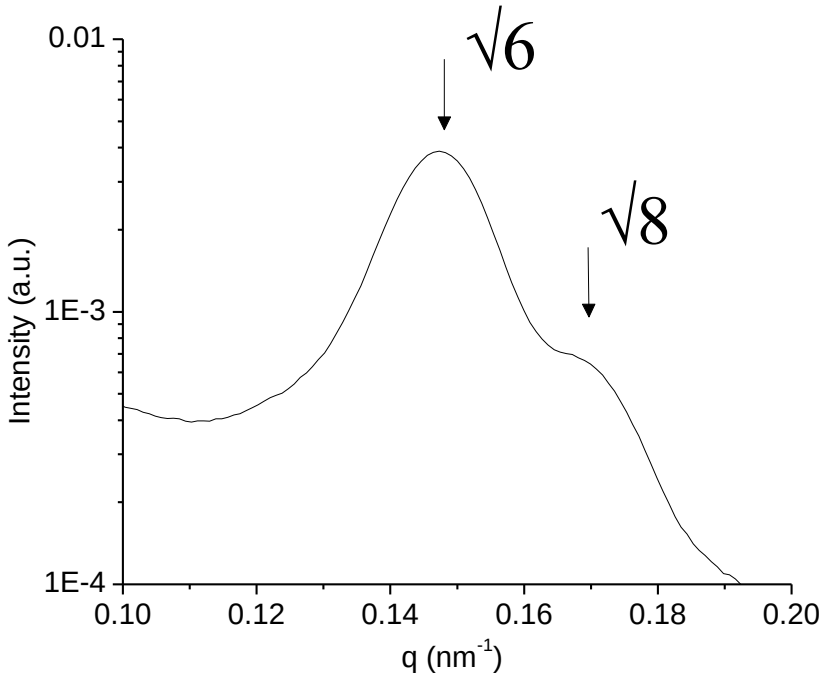

Figure 3.9. *SAXS pattern of PS-b-P4VP(PDP)$_{0.8}$ complex prepared from the diblock copolymer S4VP-53.5k-1. The initial part of the pattern is magnified to resolve the first two reflections characteristic for the double gyroid morphology.*

To examine the phase behavior of complexes with even higher molar mass and thus stronger segregation, a series of samples with *x* ranging from 1.0 to 1.7 is prepared from the block copolymer precursor S4VP-68.3k-1 (M_n(PS) = 48 000 g mol^{-1}, M_n(P4VP) = 20 300 g mol^{-1}). Here a direct transition from the lamellar to the cylindrical phase is found: LAM ($1.0 \leq x \leq 1.1$) → CYL ($1.2 \leq x \leq 1.7$), and the double gyroid morphology is not observed anymore. Representative TEM images are given in Figure 3.10. This suggests that the double gyroid phase does not exists in supramolecular complexes PS-*b*-P4VP(PDP)$_x$ based on block copolymer precursors of group 1 if the molar mass of the starting block copolymer exceeds a critical value.

The morphological characterization of PS-*b*-P4VP(PDP)$_x$ complexes from group 1 is summarized in Figure 3.11 and Table 3.2.

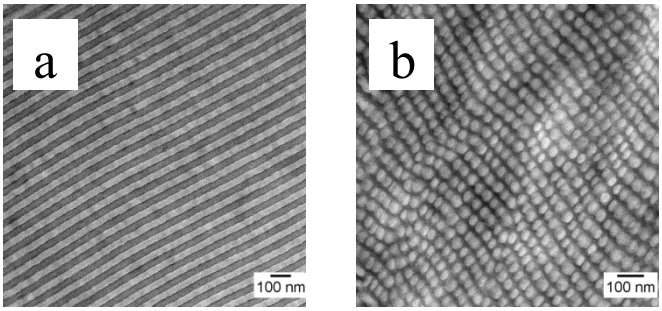

Figure 3.10. *Bright-field TEM images of PS-b-P4VP(PDP)$_x$ complexes prepared from the diblock copolymer S4VP-68.3k-1 with values of x = (a) 1.0 and (b) 1.5.*

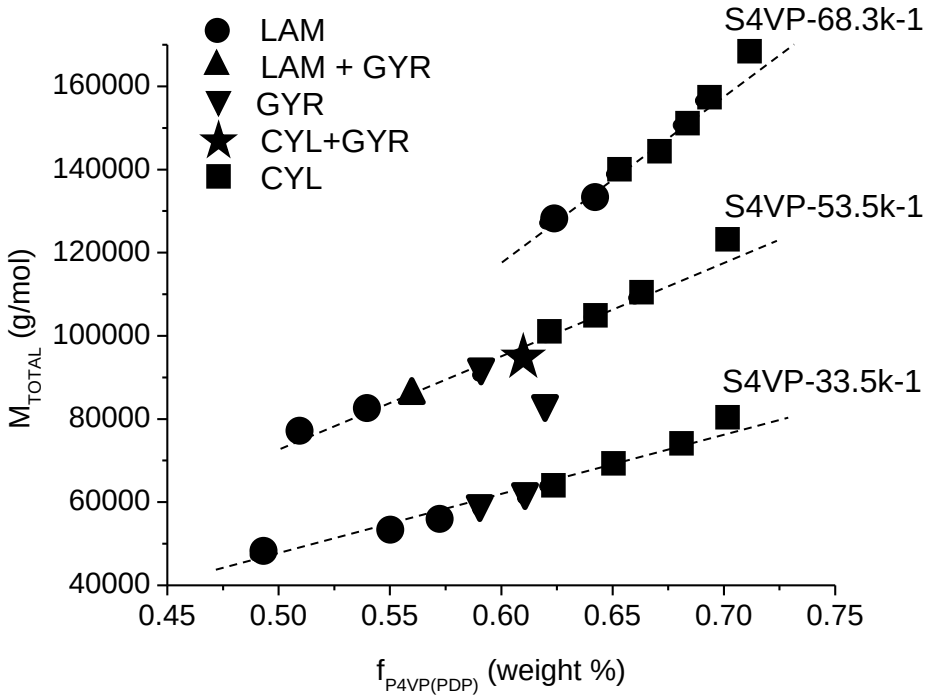

Figure 3.11. *Phase diagram of supramolecular complexes PS-b-P4VP(PDP)$_x$ from group 1. The total molar mass of the complex is given on the y-axis while the weight fraction of the comb block is given on the x-axis. Samples connected with dashed lines are prepared from the same block copolymer precursor with code as given.*

Table 3.2. *Morphological characterization of supramolecular complexes PS-b-P4VP(PDP)$_x$ from group 1.*

block copolymer code	***x***	f_{PS}	**morphology**
S4VP-45.1k-1	1.0	0.38	GYR
S4VP-33.5k-1	0.5	0.51	LAM
S4VP-33.5k-1	0.7	0.45	LAM
S4VP-33.5k-1	0.8	0.43	LAM
S4VP-33.5k-1	0.9	0.41	GYR
S4VP-33.5k-1	1.0	0.39	GYR
S4VP-33.5k-1	1.1	0.38	CYL
S4VP-33.5k-1	1.3	0.35	CYL
S4VP-33.5k-1	1.5	0.32	CYL
S4VP-33.5k-1	1.7	0.30	CYL
S4VP-53.5k-1	0.5	0.49	LAM
S4VP-53.5k-1	0.6	0.46	LAM
S4VP-53.5k-1	0.7	0.44	LAM + GYR
S4VP-53.5k-1	0.8	0.41	GYR
S4VP-53.5k-1	0.9	0.39	GYR + CYL
S4VP-53.5k-1	1.0	0.38	CYL
S4VP-53.5k-1	1.1	0.36	CYL
S4VP-53.5k-1	1.2	0.34	CYL
S4VP-53.5k-1	1.5	0.30	CYL

S4VP-68.3k-1	1.0	0.38	LAM
S4VP-68.3k-1	1.1	0.36	LAM
S4VP-68.3k-1	1.2	0.35	CYL
S4VP-68.3k-1	1.3	0.33	CYL
S4VP-68.3k-1	1.4	0.32	CYL
S4VP-68.3k-1	1.5	0.31	CYL
S4VP-68.3k-1	1.7	0.29	CYL

3.3.2 Morphological characterization of the PS-*b*-P4VP(PDP)$_x$ samples from group 2

In this group of systems the gyroid morphology is expected for $x < 1$. As a guideline for the appearance of the gyroid phase, we again prepared samples around $f_{P4VP(PDP)x} \cong 0.62$.

The total number of monomer units in the block copolymer precursors of group 2 varies from *ca.* 215 to 650, and as it will be shown, the double gyroid morphology is indeed found in several samples. The TEM image and the SAXS pattern of a representative sample PS-*b*-P4VP(PDP)$_{0.75}$ prepared from the diblock copolymer S4VP-65.0k-2 are given in Figure 3.12. The gyroid reflections $\sqrt{6}q^*$, $\sqrt{8}q^*$, $\sqrt{30}q^*$, $\sqrt{38}q^*$, and $\sqrt{50}q^*$ are resolved in the SAXS pattern (Figure 3.12b). The lattice parameter a = 124 nm, as calculated from the position of the first-order reflection at q = 0.124 nm^{-1}. The TEM image (Figure 3.12a) represents the typical "wagon wheel" gyroid pattern.

In supramolecular complexes prepared from the diblock copolymer with the shortest blocks S4VP-21.5k-2 (M_n(PS) = 12 000 g mol^{-1}, M_n(P4VP) = 9 500 g mol^{-1}), the double gyroid phase is found for x = 0.40, and when x is changed by ± 0.05, the complex adopts a lamellar and cylindrical, morphology.

For the PS-*b*-P4VP precursors with higher molar mass biphasic morphologies are mostly found. TEM images of samples with two coexisting phases are shown in

Figure 3.13. Figure 3.13a shows a combination of lamellae and gyroids for a sample based on the S4VP-56.0k-2 precursor, whereas well-ordered grains of the gyroid and the cylindrical phase, separated by a transitional phase of poorly ordered cylinders, is depicted in Figure 3.13b for a sample based on the S4VP-65.0k-2 precursor. Much to our surprise, we observed the sequence GYR + CYL → GYR → CYL rather than the anticipated GYR → GYR + CYL → CYL sequence for the samples prepared from the highest molar mass S4VP-65.0k-2. As an additional surprise, the GYR + CYL region becomes broader with an increase of the molar mass of the block copolymer precursor. This demonstrates the complex nature of the system as compared to simple diblock copolymers. Not only do we have a comblike molecular architecture of the supramolecular block, but in adition the effective interaction between PS and P4VP(PDP)$_x$, and therefore the degree of segregation, depends on the relative amount of PDP, *i.e.*, *x*.

The morphological characterization of PS-*b*-P4VP(PDP)$_x$ complexes from group 2 is summarized in Figure 3.14 and Table 3.3.

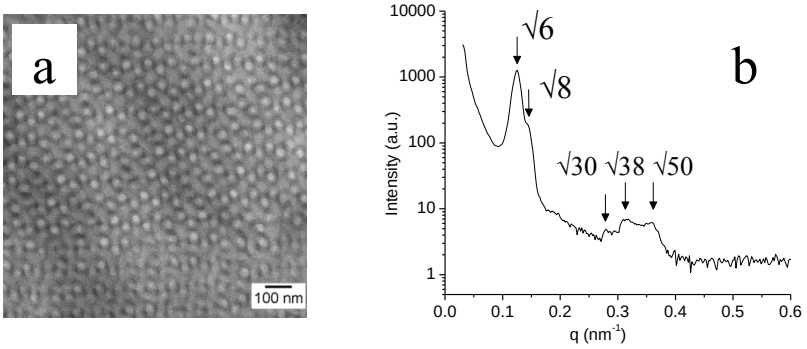

Figure 3.12. *PS-b-P4VP(PDP)$_{0.75}$ complex prepared from the diblock copolymer S4VP-65.0k-2: (a) bright-field TEM image representing the projection through the gyroid (111) plane and (b) SAXS pattern of the gyroid sample.*

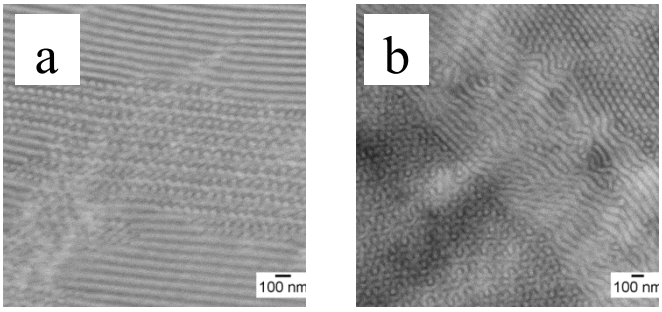

Figure 3.13. *Bright-field TEM images of PS-b-P4VP(PDP)$_x$ complexes: (a) S4VP-56.0k-2 precursor, x = 0.53 and (b) S4VP-65.0k-2 precursor, x = 0.7.*

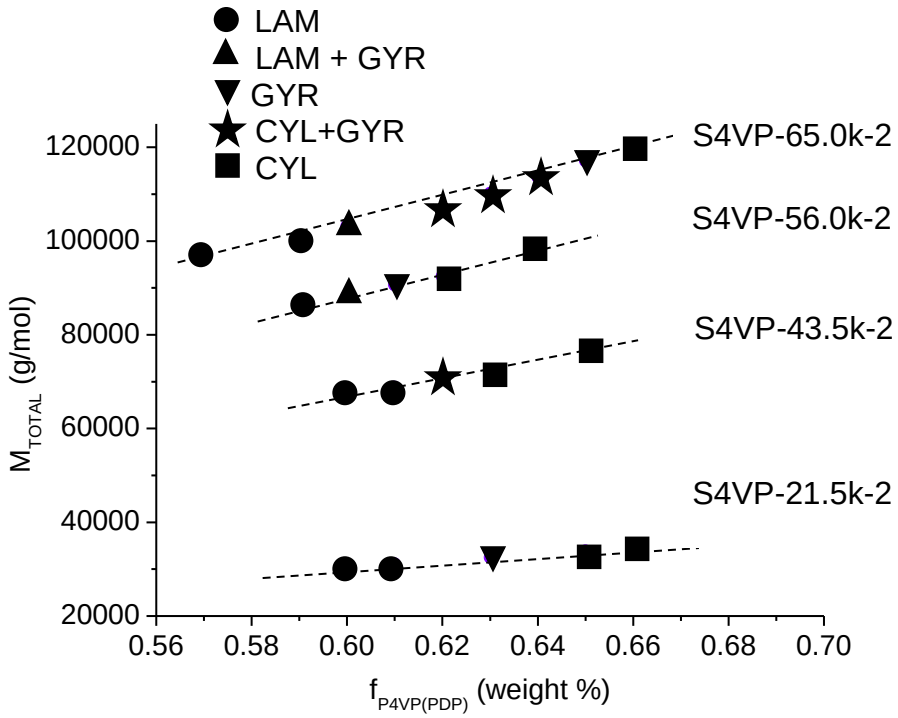

Figure 3.14. *Phase diagram of supramolecular complexes PS-b-P4VP(PDP)$_x$ from group 2. The total molar mass of the complex is given at the y-axis while the weight fraction of a comb block is given at the x-axis. Samples connected with a dashed line are prepared from the same block copolymer precursor with the code as given.*

Table 3.3. *Morphological characterization of supramolecular complexes PS-b-P4VP(PDP)$_x$ from group 2.*

block copolymer code	***x***	f_{PS}	**morphology**
S4VP-21.5k-2	0.3	0.40	LAM
S4VP-21.5k-2	0.35	0.39	LAM
S4VP-21.5k-2	0.4	0.37	GYR
S4VP-21.5k-2	0.45	0.35	CYL

S4VP-21.5k-2	0.5	0.34	CYL
S4VP-21.5k-2	1.0	0.24	CYL
S4VP-43.5k-2	0.5	0.40	LAM
S4VP-43.5k-2	0.53	0.39	LAM
S4VP-43.5k-2	0.57	0.38	GYR + CYL
S4VP-43.5k-2	0.6	0.37	CYL
S4VP-43.5k-2	0.7	0.35	CYL
S4VP-56.0k-2	0.5	0.41	LAM
S4VP-56.0k-2	0.53	0.40	LAM + GYR
S4VP-56.0k-2	0.57	0.39	GYR
S4VP-56.0k-2	0.6	0.38	CYL
S4VP-56.0k-2	0.7	0.36	CYL
S4VP-65.0k-2	0.45	0.43	LAM
S4VP-65.0k-2	0.5	0.41	LAM
S4VP-65.0k-2	0.55	0.40	LAM + GYR
S4VP-65.0k-2	0.6	0.38	GYR + CYL
S4VP-65.0k-2	0.65	0.37	GYR + CYL
S4VP-65.0k-2	0.7	0.36	GYR + CYL
S4VP-65.0k-2	0.75	0.35	GYR
S4VP-65.0k-2	0.8	0.34	CYL

3.3.3 Morphological characterization of the PS-*b*-P4VP(PDP)$_x$ samples from group 3

Finally, we discuss the morphology of PS-*b*-P4VP(PDP)$_x$ complexes where a gyroid morphology is anticipated to occur for an excess of PDP molecules with respect to the number of pyridine groups. PS-*b*-P4VP polymers with *ca.* 150, 320, and 670 monomer units in total and $r > 2.45$ (Table 3.1, group 3) are used for this purpose.

Complexes produced from the polymer precursor S4VP-15.0k-3 (M_n(PS) = 11 000 g mol^{-1}, M_n(P4VP) = 4 000 g mol^{-1}) with $N = 150$ and $1.1 \leq x \leq 1.5$ ($0.40 \geq f_{PS} \geq 0.34$) have a disordered microphase separated morphology as shown by TEM (Figure 3.15a). The value of the interaction parameter between PS and P4VP is on the order of $\chi_{S,4VP} \cong 0.35$.[39, 40] Therefore, the polymer precursor with $\chi N \cong 50$ is well within the ordered range. The disordered microphase-separated structures of the complexes confirm that the addition of PDP to PS-*b*-P4VP reduces the effective interaction parameter between the two phases, PS and P4VP(PDP), respectively.

Samples obtained from the precursor S4VP-32.0k-3 (M_n(PS) = 25 000 g mol^{-1}, M_n(P4VP) = 7 000 g mol^{-1}) with x ranging from 1.5 to 1.9 (f_{PS} varies from 0.40 to 0.35) exhibit a lamellar morphology LAM for $x = 1.5$ and a rather broad biphasic GYR + CYL region for $1.6 \leq x \leq 1.9$. Figures 3.15b and 3.15c present a gyroid grain (projection through the (110) plane) and a cylindrical grain as found in a representative biphasic sample ($x = 1.6$).

If the starting block copolymer has a sufficiently high molar mass (S4VP-67.0k-3, M_n(PS) = 50 000 g mol^{-1}, M_n(P4VP) = 17 000 g mol^{-1}) a direct transition from the lamellar to the cylindrical phase is found: LAM ($x = 1.1$) → CYL ($1.17 \leq x \leq 1.5$). Representative TEM images are provided in Figures 3.15d and 3.15e.

The morphological characterization of PS-*b*-P4VP(PDP)$_x$ complexes from group 3 is summarized in Figure 3.16 and Table 3.4.

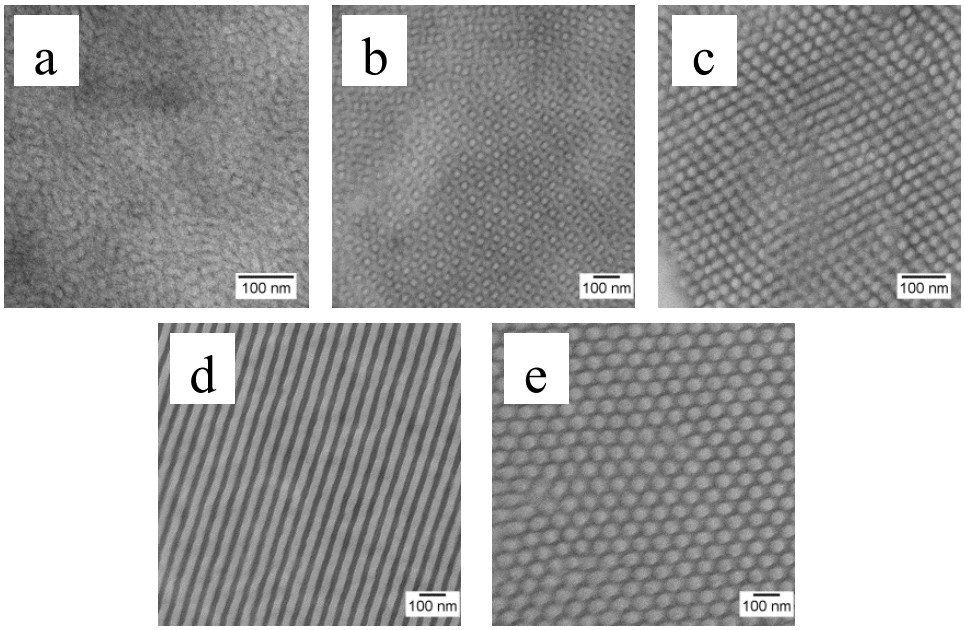

Figure 3.15. *Bright-field TEM images of PS-b-P4VP(PDP)$_x$ complexes: (a) S4VP-15.0k-3 precursor, x = 1.1, (b, c) S4VP-32.0k-3 precursor, x = 1.6, (d) S4VP-67.0k-3 precursor, x = 1.1, and (e) S4VP-67.0k-3 precursor, x = 1.5.*

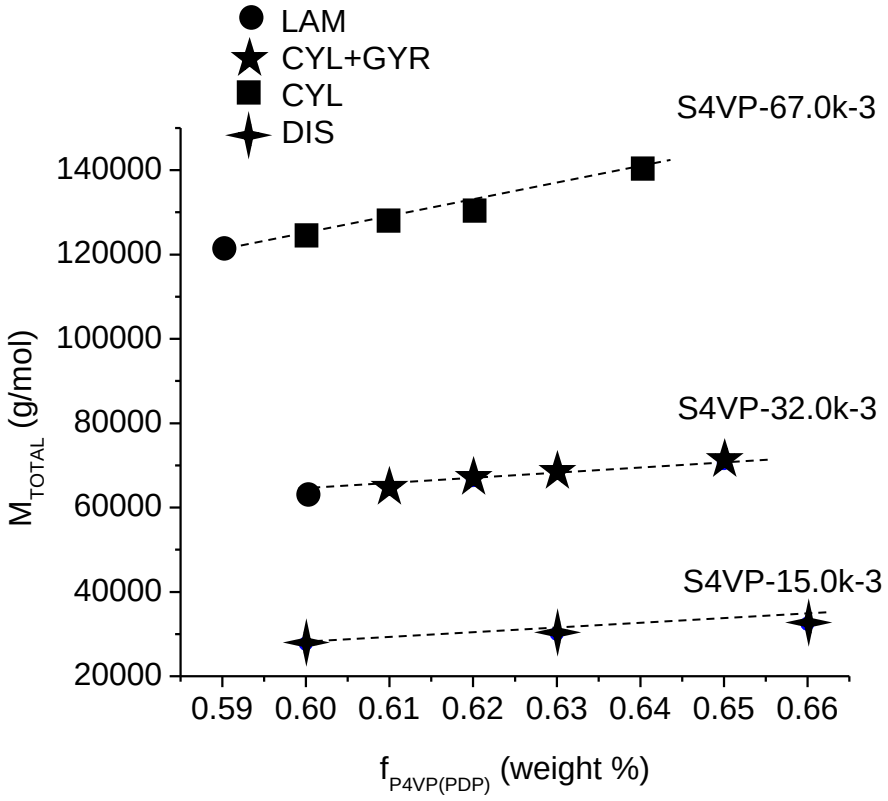

Figure 3.16. *Phase diagram of supramolecular complexes PS-b-P4VP(PDP)$_x$ from group 3. The total molar mass of the complex is given at the y-axis while the weight fraction of a comb block is given at the x-axis. Samples connected with a dashed line are prepared from the same block copolymer precursor with code as given.*

Table 3.4. *Morphological characterization of supramolecular complexes PS-b-P4VP(PDP)$_x$ from group 3.*

block copolymer code	***x***	f_{PS}	**morphology**
S4VP-15.0k-3	1.1	0.40	DIS
S4VP-15.0k-3	1.3	0.37	DIS
S4VP-15.0k-3	1.5	0.34	DIS
S4VP-32.0k-3	1.5	0.40	LAM
S4VP-32.0k-3	1.6	0.39	GYR + CYL
S4VP-32.0k-3	1.7	0.38	GYR + CYL
S4VP-32.0k-3	1.8	0.37	GYR + CYL
S4VP-32.0k-3	1.9	0.35	GYR + CYL
S4VP-67.0k-3	1.1	0.41	LAM
S4VP-67.0k-3	1.17	0.40	CYL
S4VP-67.0k-3	1.24	0.39	CYL
S4VP-67.0k-3	1.3	0.38	CYL
S4VP-67.0k-3	1.5	0.36	CYL

3.4 Conclusion

A comprehensive study of the phase behavior of supramolecular complexes PS-*b*-P4VP(PDP)$_x$ from three different groups where the double gyroid morpholohy is anticipated to occur at $x < 1.0$, $x = 1.0$, and $x > 1.0$, respectively, has been conducted. A number of samples exhibiting the double gyroid network morphology was found. The morphological characterization of the complexes from group 1 (gyroid morphology expected for $x \cong 1.0$) indicated a contraction of the width of the gyroid region with an increase in molar mass of the polymer precursor PS-*b*-P4VP, followed by the absence of the cubic *Ia3d* symmetry above a critical value. This was also found for the samples from group 3 ($x > 1.0$). Samples from group 2 behaved differently, in the sense that for the highest molar mass employed, a large biphasic window was found with one of the phases being the gyroid phase. Of course, it cannot be excluded that also for this group the gyroid morphology will cease to exist for even higher molar masses.

The size of the gyroid unit cell was tuned by varying the molar mass of the starting block copolymer from $a = 71.2$ nm to $a = 124$ nm. The porosities of the nanoporous templates obtained from gyroid supramolecular complexes PS-*b*-P4VP(PDP)$_x$ by dissolving PDP can be tuned as well since the cubic *Ia3d* symmetry appeared in samples from all three groups, *i.e.*, $x < 1.0$, $x = 1.0$, and $x > 1.0$. The results of this study show how to prepare double gyroid templates with tailored feature sizes and porosities.

3.5 Appendix

3.5.1 Electron tomography of gyroid PS-*b*-P4VP(PDP) complexes

Electron tomography was employed to further elucidate the 3D structure of gyroid supramolecular complexes.

The measurements were performed in annular dark-field (ADF) scanning transmission electron microscopy (STEM) mode using the TU/e CryoTitan. The CryoTitan, comprising a field emission gun and a Fischione high-angle ADF detector, was operated at 300kV acceleration voltage. STEM images of the tomographic tilt-series were recorded over an angular range of ± 64 degrees at 1 degree (Figure 3.17) or 2 degree increments (Figure 3.18) with Xplore3D software (FEI company). Prior to ET, ultramicrotomed thin sections of the material were stained with iodine and labeled with 10 nm and 20 nm gold particles which aid in the alignment of the tilt-series. Subsequently, the images of the tilt-series were aligned, binned to a final pixel size of 0.7 nm, and reconstructed (SIRT, 10 iterations) in IMOD.[41] Before 3D visualization using isosurface rendering in Avizo (VSG), results were denoised by nonlinear anisotropic diffusion.[41, 42]

Gyroid PS-b-P4VP(PDP)$_x$ complexes with x = 1.0 (S4VP-33.5k-1 precursor) and x = 0.8 (S4VP-53.5k-1 precursor) were studied using electron tomography. TEM micrographs of these samples display projections through various gyroid planes, as for example, the projection through (110) (Figure 3.4b, complex with x = 1.0 from S4VP-33.5k-1 precursor) or (211) gyroid plane (Figure 3.6c, complex with x = 0.8 from S4VP-53.5k-1 precursor). Additionally, their SAXS patterns contain the first two reflections in the $\sqrt{6}$:$\sqrt{8}$ ratio (Figure 3.5b, 3.7 and 3.8) which represents the unambiguous conformation of their gyroid structure. Electron tomography provides the visualization of their 3D structure. Figures 3.17 and 3.18 represent the electron tomography results from gyroid PS-b-P4VP(PDP)$_x$ complexes with x = 1.0 (S4VP-33.5k-1 precursor) and x = 0.8 (S4VP-53.5k-1 precursor), respectively. In dark-field TEM, opposite to the bright-field TEM, the iodine stained P4VP(PDP)$_x$ domains appear bright. Both gyroid samples are well-ordered over large areas/volumes. The 3D structure of the sample with the smaller repetition unit (Figure 3.17) is better resolved.

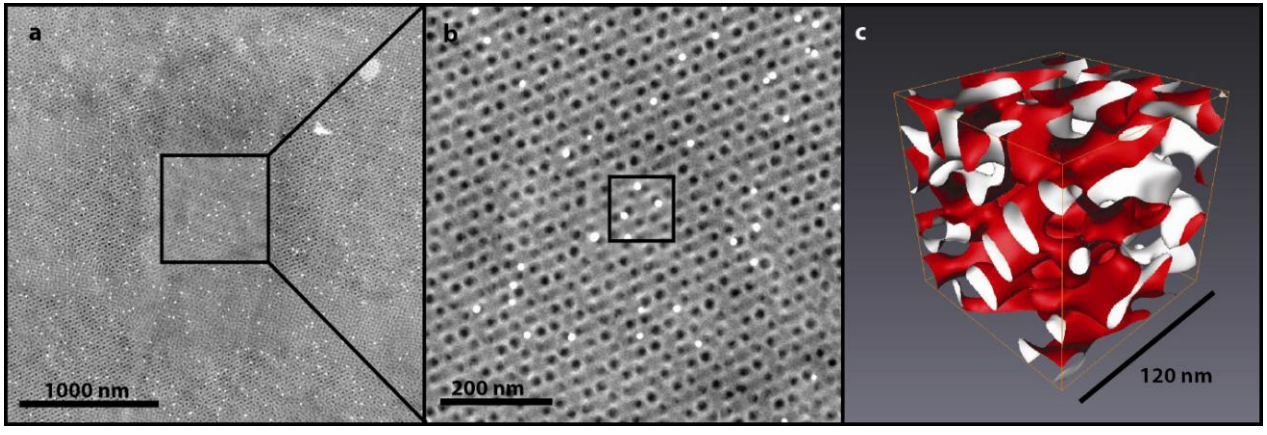

Figure 3.17. *Electron tomography results from gyroid PS-b-P4VP(PDP)$_{1.0}$ derived from S4VP-33.5k precursor.*

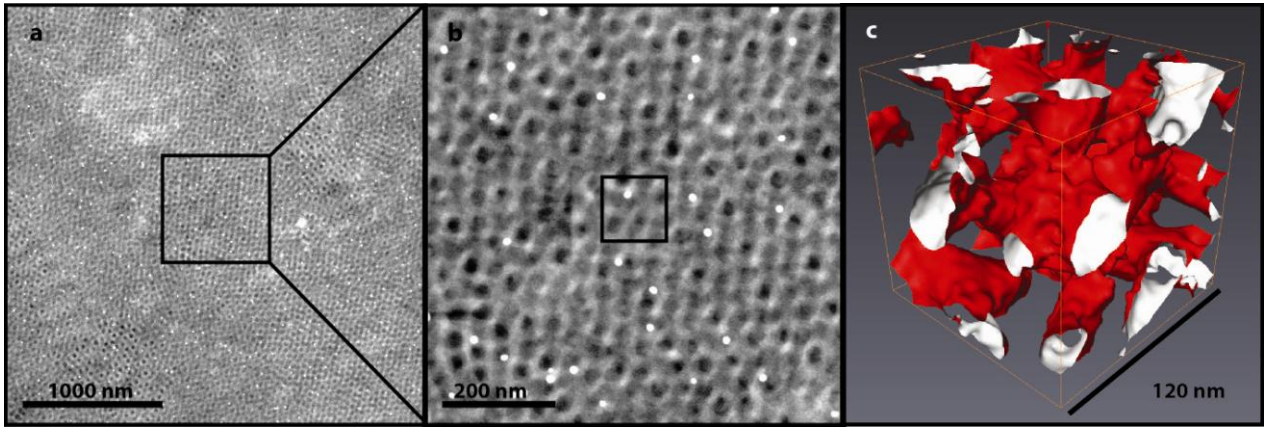

Figure 3.18. *Electron tomography results from gyroid PS-b-P4VP(PDP)$_{0.8}$ derived from S4VP-53.5k precursor.*

3.5.2 Shear-induced orientation of gyroid PS-*b*-P4VP(PDP) complexes

It is well-established that the long-range order of block copolymer structures can be induced by large amplitude oscillatory shear (LAOS).[43] In the lamellar phase, alternating layers may orient parallel, perpendicular, or transverse with respect to the shear plane (Figure 3.17). For instance, Stangler and Abetz[44] studied the orientation of lamellar polystyrene-*block*-polyisoprene (PS-*b*-PI) block copolymer upon LAOS. A perpendicular orientation was observed at 105°C and low shearing frequencies. At higher frequencies a parallel orientation of the lamellae was found that developed either from a previously perpendicular or a previously transverse orientation. The transverse orientation was obtained in lamellar polystyrene-*block*-polyisoprene (PS-*b*-PI) block copolymers of intermediate molecular weight.[45] Moreover, hexagonal cylindrical phases can also be oriented by LAOS, exposing the (10) cylindrical planes parallel with respect to the shear plane (see [43] and references therein).

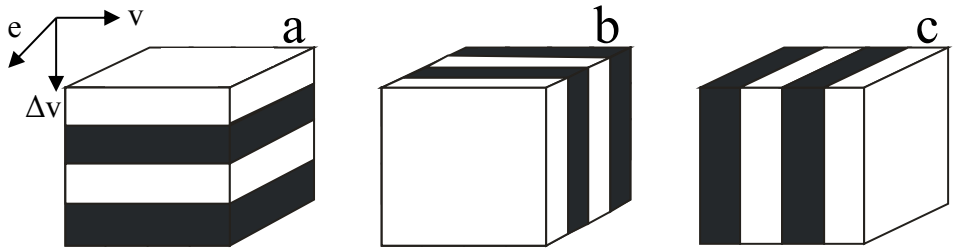

Figure 3.17. *Orientations of the lamellar phase with respect to the shear plane (v, e): (a) parallel, (b) perpendicular, and (c) transverse. Shear direction (v), gradient direction (Δv), and neutral direction (e) are displayed.*

In a blend of polystyrene-*block*-poly(2-vinylpyridine) block copolymers, a oriented gyroid phase was found to develop from the shear-oriented hexagonal cylindrical phase.[4] The epitaxial relationship between the two phases was revealed. By shearing, (10) hexagonal planes of the cylindrical structure oriented parallel to the shear plane. On heating, the oriented gyroid phase was formed with a (111) direction along the shear direction. An epitaxial relationship between the hexagonally perforated layer (HPL) and the gyroid phase was also observed.[46]

Vigild *et al.* studied the phase behavior of poly(ethylene-*alt*-propylene)-*block*-poly(dimethylsiloxane). Using isothermal time-resolved small-angle neutron scattering, they followed the transformation of the shear-oriented metastable HPL phase to the GYR phase. Additionally, they studied the isothermal growth of the GYR phase after quenching from a high-temperature shear-oriented CYL phase and the HPL appeared as a transitional phase.

Shear alignment of semi-crystalline block copolymers was studied by Fairclough *et al.*[47] Poly(ethylene oxide)-*block*-poly(butylene oxide) (PEO-*b*-PBO) block copolymer that adopted the GYR morphology in the melt state was oriented by oscillatory shear as confirmed by SAXS. Upon crystallization of the PEO block, a semicrystalline lamellar phase was formed. The lamellar planes retained the preferred directions of the oriented gyroid melt, but the domain spacing increased. Therefore, this transition was not defined as epitaxial, but it was rather concluded that the soft melt phase acted as a template for the hard crystalline phase.

The phase behavior of the gyroid PS-*b*-P4VP(PDP) supramolecular complex was examined by SAXS under *in situ* oscillatory shear. In contrast to most of the previous studies, we directly shear a gyroid sample in order to improve its orientation. The sample was heated above glass transition temperature of PS block (120 °C) and sheared *in situ* at a constant frequency (0.5 rad s^{-1}) and strain amplitude (100%). SAXS data were collected in consecutive frames of 30 s duration. The 2D diffraction pattern of the unsheared sample based on diblock copolymer S4VP-33.5k-1 with x = 1.0 (Figure 3.18a) contains two isotropic rings with $\sqrt{6}$:$\sqrt{8}$ radii ratio that originate from (211) and (220) reflection planes, respectively. After a short time of large amplitude oscillatory shear (*ca*. 2-3 min), the diffraction pattern transforms to a 10-spot pattern reported for the shear-oriented gyroid samples.[46] The 2D SAXS of shear-oriented gyroid sample is collected over a time interval of 300 s and it is displayed in Figure 3.18b.

The shear-oriented gyroid phase is aligned with (111) lattice direction parallel to the shear direction as depicted in Figure 3.19. The characteristic diffraction pattern of the shear-oriented gyroid phase consists of ten first-order and six second-order spots originating from the families of (211) and (220) reflection planes, respectively (Figure 3.20a).[46, 48] The oriented gyroid is not a single-crystal domain, but it consist of multiple domains rotated randomly around the (111) lattice directions. This characteristic 10-spot pattern arises from the rotation of single crystal domains by an angle θ around the (111) direction. Figure 3.20b

displays the sequence of eight diffraction patterns observed as the gyroid grain is rotated by an angle θ around the (111) direction. A full rotation (360°) runs three times through this sequence which is corresponding to the directionally oriented gyroid crystal.

The gyroid complexes described in chapter 3 contain randomly oriented grains with a maximal size of several micrometers. Promptly upon large amplitude oscillatory shear, the (111) gyroid lattice direction orients parallel to the shear direction. The application of sheared complexes as, for instance, precursors to metal nanofoams will lead to nanofoams with improved architecture. Since macroscopic functional properties of metal nanofoams emerge as a result of the interaction between their nanoligaments, the importance of their nanostructural architecture is obvious. Therefore, metallic nanostructures prepared from sheared complexes might have superior properties and perform better, as actuators, for example, in comparison to those prepared from unsheared complexes.

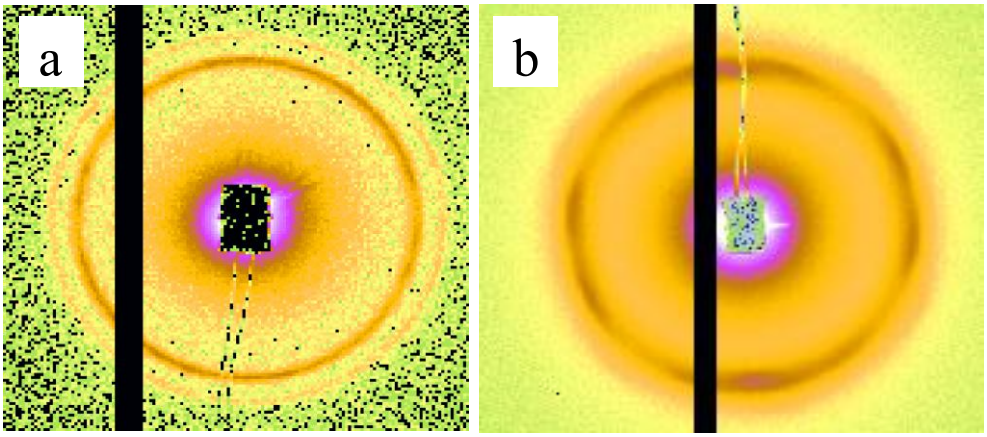

Figure 3.18. *2D diffraction patterns of PS-b-P4VP(PDP)$_{1.0}$ complex with a double gyroid morphology prepared from the diblock copolymer S4VP-33.5k-1. (a) before and (b) after shearing at 120 °C, 0.5 rad s^{-1} frequency, and 100% strain amplitude.*

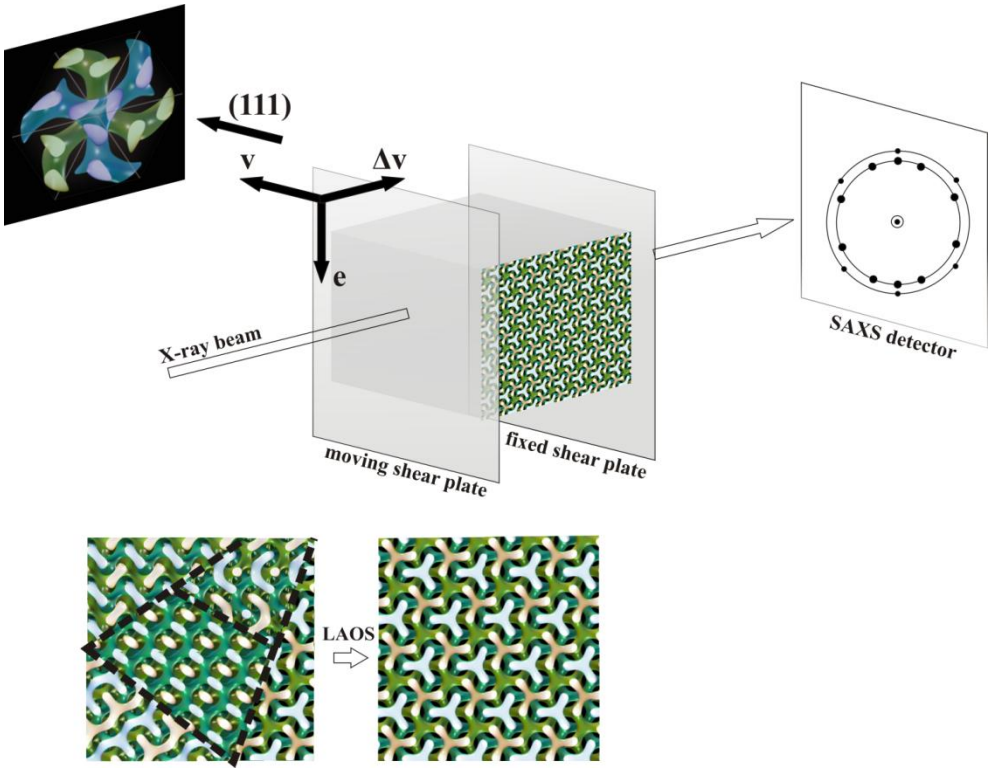

Figure 3.19. *Schematic representation of shear-induced orientation of the gyroid PS-b-P4VP(PDP) complex. The gyroid phase aligns with the (111) direction parallel to the shear direction. Its diffraction pattern consist of ten first-order and six second-order spots originating from the families of (211) and (220) reflection planes, respectively. Shear direction (v), gradient direction (Δv), and neutral direction (e) are displayed. TEM simulations are adapted from [49].*

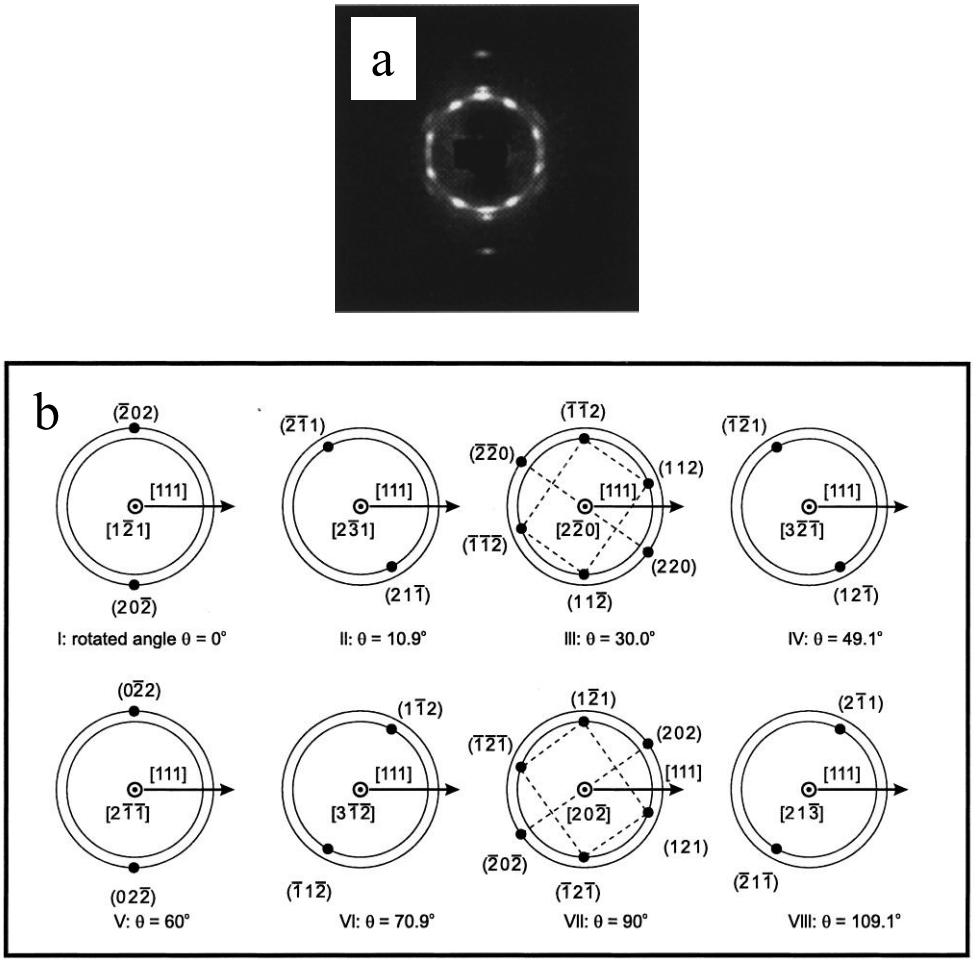

Figure 3.20. *(a) SAXS pattern of poly(ethylene-alt-propylene)-block-poly(dimethylsiloxane) diblock copolymer with the oriented gyroid phase developed from the shear-oriented HPL phase.(b) The sequence of eight diffraction patterns encountered as the gyroid structure is rotated by an angle θ around the (111) direction. Reprinted with permission from [46]. Copyright 1998 American Chemical Society.*

3.5.3 Temperature-induced phase transitions in gyroid PS-*b*-P4VP(PDP) complexes

The phase behavior of the gyroid PS-*b*-P4VP(PDP)$_{1.0}$ complex, based on S4VP-33.5k-1 diblock copolymer, upon heating/cooling was examined by SAXS. SAXS heating scans (Figure 3.21a) indicated the phase transition GYR → LAM around 170 °C. The GYR → LAM transition in a similar gyroid PS-*b*-P4VP(PDP)$_x$ complex was reported in literature.[31] Upon cooling, the opposite LAM → GYR transition was not found (Figure 3.21b) which indicated that probably upon cooling the complex got trapped into a metastable lamellar state.

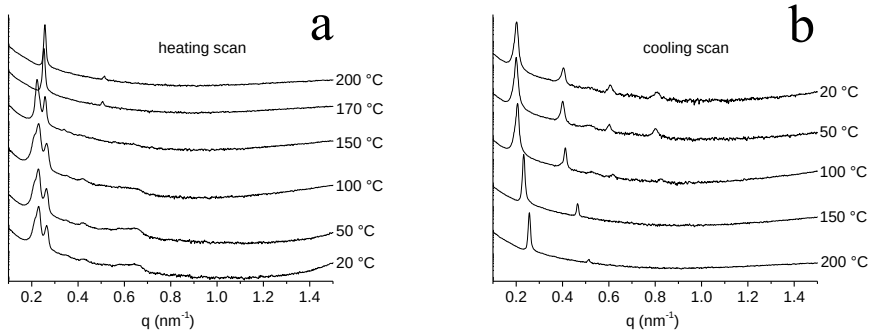

Figure 3.21. *SAXS patterns of PS-b-P4VP(PDP)$_{1.0}$ complex prepared from the diblock copolymer S4VP-33.5k-1 as a function of temperature. (a) The sample is heated from 20 to 200 °C with a heating rate 10 °C/min. (b) The sample is cooled from 200 to 20 °C with a cooling rate 10 °C/min.*

3.6 References

1. Szwarc M. Nature 1956;178:1168-1169.
2. Bates FS, Fredrickson GH. Annu Rev Phys Chem 1990;41:525-527.
3. Hajduk DA, Harper PE, Gruner SM, Honeker CC, Kim G, Thomas EL, et al. Macromolecules 1994;27(15):4063-4075.
4. Schulz MF, Bates FS, Almdal K, Mortensen K. Phys Rev Lett 1994;73(1):86-89.
5. Hamley IW. The Physics of Block Copolymers. Oxford: Oxford University Press, 1998.
6. Meuler AJ, Hillmyer MA, Bates FS. Macromolecules 2009;42:7221-7250.
7. Bates FS, Fredrickson GH. Phys Today 1999;52:32-38.
8. Epps TH, Cochran EW, Bailey TS, Waletzko RS, Hardy CM, Bates FS. Macromolecules 2004;37(22):8325-8341.
9. Abetz V, Simon P. Phase Behaviour and Morphologies of Block Copolymers. Adv Polym Sci, vol. 189: Springer Berlin / Heidelberg, 2005. pp. 125-212.
10. Tyler CA, Qin J, Bates FS, Morse DC. Macromolecules 2007;40(13):4654-4668.
11. Matsushita Y. Macromolecules 2007;40(4):771-776.
12. Gobius du Sart G, Vukovic I, Alberda van Ekenstein G, Polushkin E, Loos K, ten Brinke G. Macromolecules 2010;43(6):2970-2980.
13. Faber M, Voet VSD, ten Brinke G, Loos K. Soft Matter 2012;8(16):4479-4485.
14. Crossland EJW, Kamperman M, Nedelcu M, Ducati C, Wiesner U, Smilgies DM, et al. Nano Letters 2008;9(8):2807-2812.
15. Hsueh H-Y, Chen H-Y, She M-S, Chen C-K, Ho R-M, Gwo S, et al. Nano Letters 2010;10(12):4994-5000.
16. Urbas AM, Maldovan M, DeRege P, Thomas EL. Adv Mater 2002;14(24):1850-1853.
17. Vignolini S, Yufa NA, Cunha PS, Guldin S, Rushkin I, Stefik M, et al. Adv Mater 2012;24(10):OP23-OP27.
18. Cochran EW, Garcia-Cervera CJ, Fredrickson GH. Macromolecules 2006;39(2449-2451).
19. Matsen MW. Macromolecules 1995;28(17):5765-5773.

20. Hayashida K, Takano A, Arai S, Shinohara Y, Amemiya Y, Matsushita Y. Macromolecules 2006;39(26):9402-9408.
21. Lo C-T, Lee B, Pol VG, Dietz Rago NL, Seifert S, Winans RE, et al. Macromolecules 2007;40(23):8302-8310.
22. Ajdari A, Leibler L. Macromolecules 1991;24:6803-6805.
23. Xi H, Milner ST. Macromolecules 1996;29(7):2404-2411.
24. Gobius du Sart G, Vukovic I, Vukovic Z, Polushkin E, Hiekkataipale P, Ruokolainen J, et al. Macromol Rapid Commun 2011;32(4):366-370.
25. Nandan B, Vyas MK, Böhme M, Stamm M. Macromolecules 2010;43(5):2463-2473.
26. Ikkala O, ten Brinke G. Science 2002;295:2407-2409.
27. Mäki-Ontto R, de Moel K, de Odorico W, Ruokolainen J, Stamm M, ten Brinke G, et al. Adv Mater 2001;13:117-121.
28. Hillmyer MA. Adv Polym Sci 2005;190:137-181.
29. Crossland EJW, Ludwigs S, Hillmyer MA, Steiner U. Soft Matter 2010;6(3):670-676.
30. Urade VN, Wei TC, Tate MP, Kowalski JD, Hillhouse HW. Chem Mater 2007;19:768-777.
31. Valkama S, Ruotsalainen T, Nykänen A, Laiho A, Kosonen H, ten Brinke G, et al. Macromolecules 2006;39(26):9327-9336.
32. Borsboom M, Bras W, Cerjak I, Detollenaere D, Glastra Van Loon D, Goedtkindt P, et al. J Synchrotron Radiat 1998;5:518-520.
33. Bras W, Dolbnya IP, Detollenaere D, van Tol R, Malfois M, Greaves GN, et al. J Appl Crystallogr 2003;36:791-794.
34. Matsen MW. J Phys: Condens Matter 2002;14:R21-R47.
35. Ruokolainen J, Torkkeli M, Serimaa R, Komanschek BE, Ikkala O, ten Brinke G. Phys Rev E 1996;54:6646-6649.
36. Angerman HJ, ten Brinke G. Macromolecules 1999;32:6813-6820.
37. Feng EH, Lee WB, Fredrickson GH. Macromolecules 2007;40(3):693-702.
38. Hamley IW, Castelletto V. Progress in Polymer Science 2004;29(9):909-948.
39. van Ekenstein AGOR, Meyboom R, ten Brinke G, Ikkala O. Macromolecules 2000;33:3752-3756.
40. Zha W, Han CD, Lee DH, Han SH, Kim JK, Kang JH, et al. Macromolecules 2007;40(6):2109-2119.

41. Kremer JR, Mastronarde DN, McIntosh JR. J Struct Biol 1996;116(1):71-76.
42. Frangakis AS, Hegerl R. J Struct Biol 2001;135(3):239-250.
43. Hamley IW. J. Phys.: Condens. Matter 2001;13:R643-R671.
44. Stangler S, Abetz V. Rheol Acta 2003;42:569-577.
45. Zhang Y, Wiesner U. J Chem Phys 1995;103(11):4784-4793.
46. Vigild ME, Almdal K, Mortensen K, Hamley IW, Fairclough JPA, Ryan AJ. Macromolecules 1998;31(17):5702-5716.
47. Fairclough JPA, Mai S-M, Matsen MW, Bras W, Messe L, Turner SC, et al. J Chem Phys 2001;114(12):5425-5431.
48. Foerster S, Khandpur AK, Zhao J, Bates FS, Hamley IW, Ryan AJ, et al. Macromolecules 1994;27(23):6922-6935.
49. https://secure.msri.org/about/sgp/jim/software/temsim/index.html.

Chapter 4

Hexagonally Perforated Layer Morphology in PS-*b*-P4VP(PDP) Supramolecules

In this chapter, PS-b-P4VP(PDP) complexes with a minority P4VP(PDP) block are morphologically characterized focusing on the region between the lamellar and cylindrical phase. Dynamic mechanical measurements and small-angle X-ray scattering are used to follow the transitions between the ordered states upon heating/cooling. The self-assembled state at various temperatures is determined by small-angle X-ray scattering and transmission electron microscopy. In contrast to the opposite case of majority P4VP(PDP) blocks, where the transition from lamellar to cylindrical structures frequently occurs via the gyroid morphology (chapter 3), the complexes adopt the hexagonally perforated layered morphology in a broad range of compositions. Although known as a metastable phase in pure diblock copolymers, the hexagonally perforated layered phase appears as an equilibrium phase in PS-b-P4VP(PDP) complexes, being stabilized by the presence of the hydrogen-bonded PDP side chains in the minority component domains.

Part of this chapter was published in: *Macromolecules 2012, 45, 9409-9418.*

4.1 Introduction

During the last few decades extensive research has been devoted to the field of block copolymers.[1-3] Block copolymers are built out of chemically different blocks that generally repel each other, but their covalent attachment prevents macrophase separation to occur. Instead, microphase separation takes place leading to a variety of ordered nanostructures with ample opportunities for nanotechnological applications.[4-6] As mentioned previously, three parameters mainly dictate the phase behavior of block copolymers: (1) the degree of polymerization, N, (2) the Flory-Huggins interaction parameter, χ, and (3) the composition, *i.e.*, the volume fraction of each block, f. A symmetric diblock copolymer (f = 0.5) with sufficiently high χN is ordered into a lamellar structure (LAM). As f increases, the copolymer becomes more asymmetric and morphologies such as cylindrical (CYL) or spherical (SPH) become favorable. In a small part of the phase diagram between the LAM and CYL region, additional intriguing morphologies appear: the gyroid (GYR),[7, 8] the hexagonally perforated layers (HPL),[9, 10] and the *Fddd* (O^{70}) phase.[11-13] *Fddd* is an orthorhombic, single-network phase, while the GYR phase has a cubic symmetry and consists of two interpenetrated, 3D continuous networks inside a continuous matrix. Besides *Fddd* and GYR morphology, the hexagonally perforated lamellar (HPL) structure has also been found experimentally. The HPL structure consist of alternating layers of the minority and majority component and the former layers contain hexagonally packed cylinders of the majority component. However, theoretical studies found *Fddd* and GYR to be stable equilibrium phases, whereas the HPL is only a metastable phase in neat diblock copolymers.[14, 15]

To achieve a specific morphology the system parameters (f, N, χ) have to be selected carefully and this becomes considerably more challenging if the desired structure exists only in a rather narrow range of f and χN values. Additionally, time-consuming elaborate syntheses are required to obtain all the different morphologies in one kind of block copolymer system. The process of creating different morphologies in a given diblock copolymer system can be simplified by adding a component that preferentially resides in the domains of one of the blocks, thereby allowing a simple alteration in the effective composition (f) with concurrent adaptation of the structure. Well-known examples include block copolymer/homopolymer blends in which the homopolymer is chemically identical to one of the copolymer blocks,[16-19] blends in which the homopolymer forms

hydrogen bonds with one of the copolymer blocks,[20, 21] and mixtures of block copolymers and hydrogen-bonding low molecular weight compounds.[22-24] Their phase behavior often resembles that of neat diblock copolymers. Hashimoto and co-workers studied the phase behavior of polystyrene-*block*-polyisoprene (PS-*b*-PI) blended with polystyrene homopolymer (PS) and found that its phase diagram shows complexity and features similar to phase diagrams of pure block copolymers.[19] Shih-Chien Chen *et al.* investigated blends of poly(4-vinylphenol)-*block*-polystyrene (PVPh-*b*-PS) and homopolymers with different hydrogen bonding strength: poly(4-vinylpyridine) (P4VP), poly(methyl methacrylate) (PMMA), and poly(4-vinylphenol) (PVPh).[21] It was shown that the PVPh-*b*-PS/P4VP blend has a much higher fraction of hydrogen bonded PVPh block compared to the blends with PMMA and PVPh homopolymers. Furthermore, the PVPh-*b*-PS/P4VP blend behaves as a neat diblock copolymer and exhibits the characteristic series of transitions (LAM → GYR → CYL → SPH) as the P4VP content increases.

As the segment–segment interaction parameter, χ, is inversely proportional to temperature, the phase behavior of block copolymers is thermally dependent, and examples of thermoreversible order-order transitions (OOT) in classical block copolymers, such as cylindrical-to-spherical,[25-27] cylindrical-to-gyroid,[28, 29] or lamellar-to-cylindrical,[30, 31] have been reported in the literature. In mixtures of block copolymers and hydrogen-bonding low molecular weight compounds, elevated temperatures reduce the strength of hydrogen bonds and may also induce the solubility of low molecular weight compounds in the non-hydrogen bonding block, thus leading to OOTs.[22, 23]

Several studies focused on the mixture between polystyrene-*block*-poly(4-vinylpyridine) (PS-*b*-P4VP) copolymer and the low molecular weight amphiphilic compound pentadecylphenol (PDP), that forms hydrogen bonds with the P4VP block.[32, 33] Valkama *et al.* investigated the phase diagram of PS-*b*-P4VP(PDP)$_{1.0}$ (the number in the subscript denotes the ratio between PDP molecules and P4VP monomer units) and, besides classical morphologies, reported novel structures, such as HPL and GYR, in two individual complexes at room temperature (the weight fraction of P4VP(PDP)$_{1.0}$ block, $f_{P4VP(PDP)x}$, was 0.28 and 0.62, and the total molar mass, including PDP, was 49 500 and 83 300 g mol^{-1}, respectively).[22] In the previous chapter, the PS-*b*-P4VP(PDP)$_x$ phase behavior in the region between the LAM and CYL phase with P4VP(PDP)$_x$ being the majority component was meticulously examined. At these compositions the supramolecular

complexes appeared to behave very similar to neat diblock copolymers, considering that the transition sequence LAM → GYR → CYL was generally found as the weight fraction of the P4VP(PDP)$_x$ block increased. A set of gyroid samples with tailored feature sizes was obtained in the composition range 0.59 < $f_{P4VP(PDP)x}$ < 0.65 and they could be exploited in a number of practical applications.[5, 6, 34, 35]

In the present study, we are focusing on the PS-*b*-P4VP(PDP)$_x$ phase behavior in the region between the CYL and LAM phase at the other side of the phase diagram in which PS represents the majority rather than the minority component. Our initial motivation was to find the gyroid morphology with P4VP(PDP)$_x$ being the minority network component. However, instead of GYR, a surprisingly broad region with HPL was found and a quite fascinating phase behavior was discovered. The PS-*b*-P4VP(PDP)$_x$ complexes investigated are prepared from block copolymer precursors with molar masses ranging from 33 700 to 67 000 g mol^{-1}, and the amount x of PDP added is adjusted to achieve $f_{P4VP(PDP)x}$ between 0.30 and 0.39. Temperature dependent SAXS and dynamic mechanical measurements are conducted to follow thermally induced order-order phase transitions in the samples and determine their morphologies. TEM is employed as an additional technique to further elucidate room temperature and high temperature equilibrium morphologies of PS-*b*-P4VP(PDP)$_x$ complexes. The HPL morphology appears to be the equilibrium morphology in a broad composition range, in contrast to the phase behavior of neat diblock copolymers. This perforated layered structure was experimentally found before, but the authors could not determine whether it was a metastable or an equilibrium structure.[22, 36] Self-consistent mean-field theory calculations by Matsen indicated that the HPL phase can be stabilized by the addition of homopolymer to a diblock copolymer at certain compositions due to the relief of packing frustrations.[37, 38] This principle may apply even more to the PS-*b*-P4VP(PDP)$_x$ supramolecular side chain complexes, thus explaining the phase behavior observed.

4.2 Experimental section

4.2.1 Materials and sample preparation

Materials. *sec*-Butyllithium (*s*BuLi, Acros, 1.3 M in cyclohexane) was used without further purification as an initiator in anionic polymerization. Styrene (St, 99%, Acros) was dried over calcium hydride for 24 h and over dibutylmagesium for another 24 h. Finally, it was condensed into a storage ampule and kept at −18 °C under nitrogen atmosphere. 4-Vinylpyridine (4VP, Acros, 95%) was stirred under nitrogen atmosphere over calcium hydride for 24 h at room temperature and condensed into a flask containing freshly cut sodium. When the solution turned yellowish green, it was condensed into an ampule and stored under nitrogen at −18 °C. Tetrahydrofuran (THF, Acros, 99.9%) was first condensed and then reacted with *tert*-butyllithium for 45 min at −78 °C. A yellow color of solution was the indication that the solvent was suitable for anionic polymerization. Afterward the solvent was condensed into the polymerization flask and degassed by three freeze–pump–thaw cycles. LiCl (Aldrich, 99.99 +%) was dried overnight in vacuum at 130 °C. Several other PS-*b*-P4VP copolymers were supplied by Polymer Source Inc. and used as received. Their properties are listed in Table 4.1. Chloroform (p.a., LAB-SCAN) was used as received. 3-Pentadecylphenol (PDP, 98%, Aldrich) was recrystallized twice from petroleum ether. Methanol was degassed by argon bubbling for several hours at room temperature.

Synthesis of PS-*b*-P4VP by anionic polymerization. The PS-*b*-P4VP diblock copolymer was synthesized by sequential anionic polymerization in THF at −78 °C on a high-vacuum line. LiCl was added in 5-fold excess relative to the amount of initiator in order to stabilize anionic species and minimize side reactions. Using degassed syringes, St and *s*BuLi were added to the polymerization flask and the reaction started. After 45 min, a 10 mL sample for GPC analysis was withdrawn and dispersed into degassed methanol. Then the calculated amount of 4VP was added and the reaction was allowed to proceed for another 45 min. The polymerization was terminated by the addition of 5 mL of degassed methanol. The block polymer was precipitated in water and characterized with GPC and ^{1}H NMR. The properties of the synthesized polymer are given in Table 4.1.

Preparation of the polymer films. Films of the supramolecular complexes PS-*b*-P4VP(PDP) were prepared according to the procedure described in chapter 3.

4.2.2 Characterization methods

^{1}H NMR spectra in $CDCl_3$ were recorded on a 400 MHz Varian VXR operating at room temperature.
Gel permeation chromatography (GPC) was performed in DMF (1 mL min^{-1}) with 0.01 M LiBr on a Viscotek GPCmax equipped with model 302 TDA detectors, using two columns (PSS-Gram-1000/30, 10 μ 30 cm). The GPC is calibrated using narrow disperse poly(methyl methacrylate) standards (Polymer Laboratories).
Transmission electron microscopy (TEM) was performed on a Philips CM12 transmission electron microscope operating at an accelerating voltage of 120 kV. Images were recorded on a Gatan slow-scan CCD camera. Samples for TEM were prepared according to the procedure described in chapter 2. To obtain contrast for TEM, the samples were stained with iodine (45 min). To study high temperature structures, the samples were first annealed for 4h hours at desired temperature and then quenched in liquid nitrogen.
Small-angle X-ray scattering (SAXS) was performed at the Dutch–Belgian Beamline (DUBBLE) station BM26B of the European Synchrotron Radiation Facility (ESRF) in Grenoble (France). The sample-to-detector distance was *ca.* 6 m. The SAXS patterns were collected in temperature range between 20 and 200 °C with a heating/cooling rate of 10 °C/min. The detailed explanation of the technique is provided in chapter 3.[39, 40]
Dynamic mechanical experiments were performed on a AR 1000 N rheometer using an aluminum cone-and-plate fixture of 4° and 20 mm in diameter. The frequency of 0.1 Hz and the strain amplitude of 0.1% were applied to the sample during heating and cooling cycles. Sample temperature was varied in a range between 100 and 200 °C, with a heating/cooling rate of 1 °C/min.

Table 4.1. *Properties of the diblock copolymers PS-b-P4VP used in this study.*[a]

sample code	**M_n(PS), g mol^{-1}**	**M_n(P4VP), g mol^{-1}**	**PDI**
S4VP-33.7k[b]	27 200	6 500	1.07
S4VP-41.0k[c]	33 000	8 000	1.10
S4VP-45.6k[c]	40 000	5 600	1.09
S4VP-67.0k[c]	50 000	17 000	1.13

[a]*The number in the sample code denotes the total molar mass of the block copolymer.*

[b]*Synthesized by anionic polymerization.*

[c]*Obtained from Polymer Source Inc.*

4.3 Results and discussion

To thoroughly explore the phase behavior of PS-*b*-P4VP(PDP)$_x$ complexes, the molar mass of the block copolymer precursors and the amount of PDP in the samples are systematically changed.

We start with a set of PS-*b*-P4VP(PDP)$_x$ complexes prepared from the block copolymer S4VP-33.7k synthesized by living anionic polymerization. Block copolymer S4VP-33.7k is characterized by ^{1}H NMR (Figure 4.1) and GPC (Figure 4.2). The PDP content is varied from x = 0.3 to x = 0.5, which implies a change in the weight fraction of the P4VP(PDP)$_x$ block from 0.31 to 0.37. Surprisingly, at room temperature all the investigated samples adopt the HPL structure, which subsequently transforms to the CYL phase at higher temperatures. The morphological characterization of a representative sample (x = 0.5) is given in Figures 4.3, 4.4, and 4.5. The change in morphology of a block copolymer system can be followed by monitoring the change in its mechanical properties.[41-43] Figure 4.3 presents the dynamic storage modulus *G'* during temperature scans of the aforementioned sample at a constant frequency of 0.1 Hz and a constant shear amplitude of 0.1%. *G'* decreases constantly as the temperature increases to 140 °C and then it suddenly begins to increase indicating a transition between two ordered states. The cooling scan confirms that the observed transition is reversible and that the low temperature phase is thermodynamically stable. To identify the symmetry of both phases, SAXS measurements are performed (Figure 4.4). SAXS results during cooling (Figure 4.4a) and heating (Figure 4.4b) confirm that the reversible order-order transition occurs between 140 and 160 °C. The SAXS intensity pattern of the sample at 200 °C is shown in Figure 4.4c. The diffraction peaks positioned in the q ratio 1:√3:√4:√7:√9 indicate the CYL morphology of the complex at high temperatures (q^* = 0.272 nm^{-1}, hence, the distance between the cylinders is 26.7 nm). The SAXS curve of the low temperature phase (Figure 4.4d) contains three peaks at q^*, 1.08q^*, and 2q^*, which can be attributed to the HPL structure.[42, 44-46] The peak at 0.92q*, characteristic for the HPL phase, is comprised in the intense first-order diffraction peak and it is not distinguished probably due to the lack of the long-range order. To confirm the low temperature structure of the sample, TEM is employed as a supplementary technique. The schematic representation of the HPL morphology and its various projections is depicted in Figure 4.5 (a, c–e) and a good agreement with the experimental TEM data (Figure 4.5b) is found. In the TEM micrograph, the HPL structure is clearly manifested by

the projections parallel (region A and C) and normal (region B) to the perforated layers. The PS domains appear bright while the $P4VP(PDP)_{0.5}$ domains appear dark due to selective iodine staining. The parallel projections consist of alternating layers of majority PS and minority $P4VP(PDP)_{0.5}$ component and the latter are shown with (region A) and without the perforations (region C). Hexagonally packed bright spots result from the normal projection of the PS perforations (region B).

The complexes with x = 0.3 and x = 0.4 exhibit similar phase behaviors (Figures 4.6–4.9); at room temperature they adopt the HPL structure, which is transformed into the CYL phase as temperature increases.

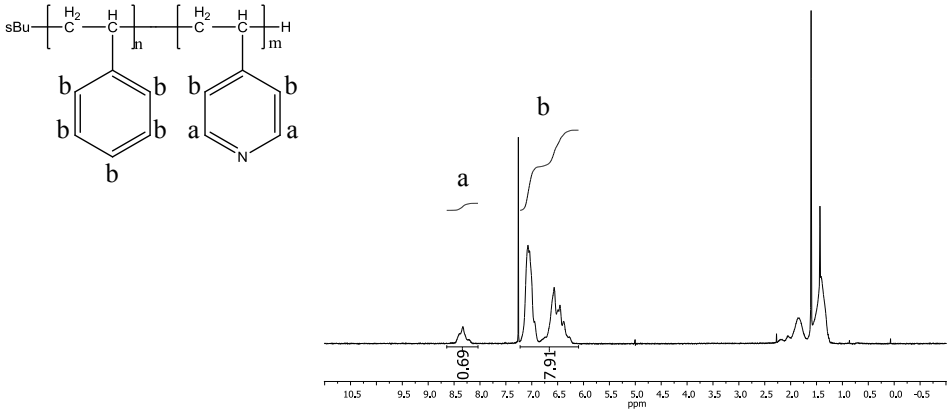

Figure 4.1. *^{1}H NMR spectrum of S4VP-33.7k block copolymer. The signal around 8.3 ppm corresponds to two protons at meta positions in the pyridine ring (a), and the group of signals at 6.0–7.2 ppm correspond to two protons at ortho positions in the pyridine ring and the protons of the aromatic polystyrene ring (b). Comparing the areas below these signals, the composition of the block copolymer is determined to be f_{P4VP} = 0.194.*

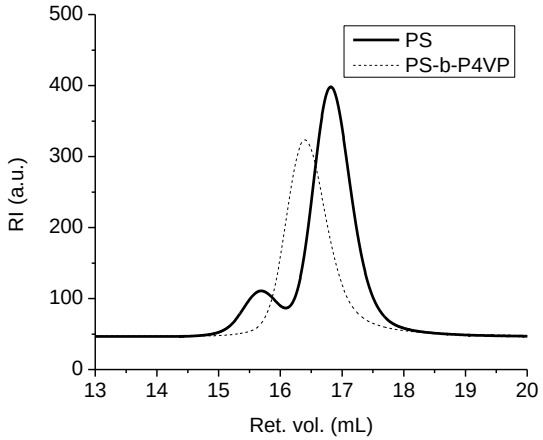

Figure 4.2. *An overlay of GPC traces of PS homopolymer precursor (solid line) and S4VP-33.7k block copolymer (dashed line). A shoulder in the GPC trace of PS indicates the oxidative coupling.*

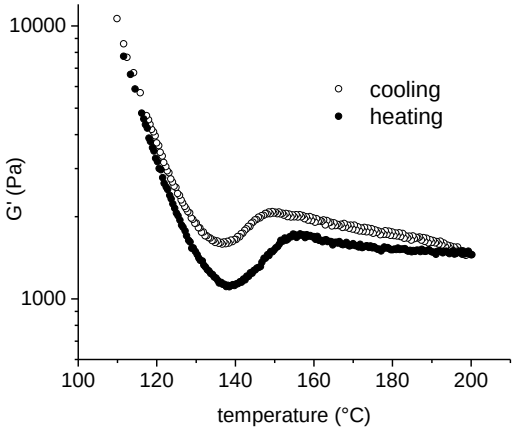

***Figure* 4.3.** *Temperature dependence of the dynamic storage modulus (G') for PS-b-P4VP(PDP)$_{0.5}$, $f_{P4VP(PDP)}$ = 0.37, M_{total} = 43 100 g mol^{-1} based on S4VP-33.7k. The frequency of shearing is 0.1 Hz, the strain amplitude 0.1%, and the heating/cooling rate is 1 °C/min.*

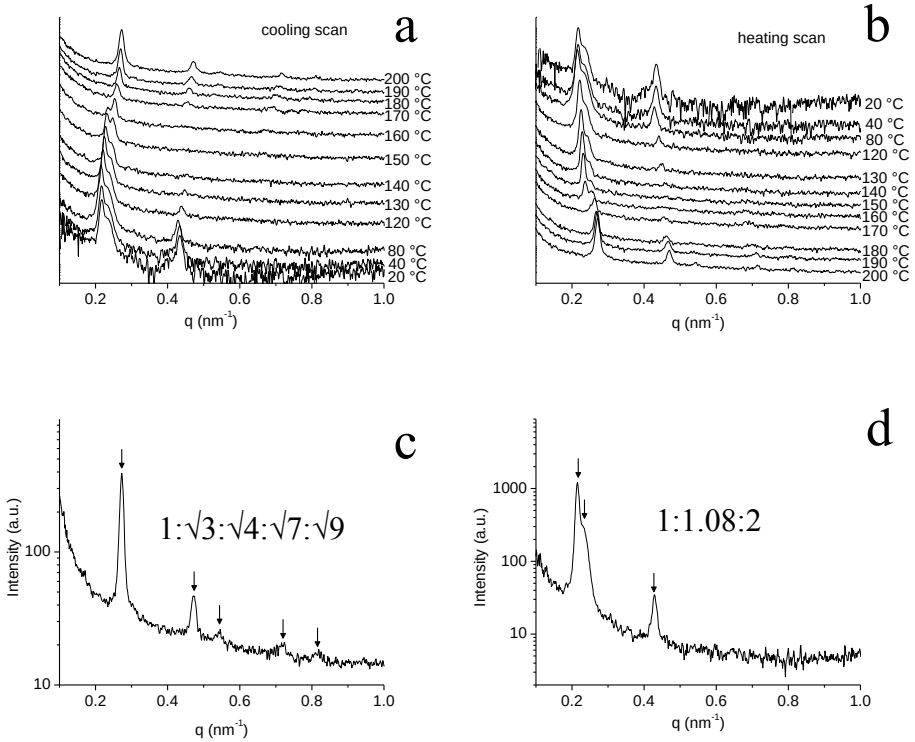

Figure 4.4. *SAXS intensity patterns for PS-b-P4VP(PDP)$_{0.5}$, $f_{P4VP(PDP)}$ = 0.37, M_{total} = 43 100 g mol^{-1} based on S4VP-33.7k (a) as a function of temperature, the sample is cooled from 200 to 20 °C with a cooling rate of 10 °C/min, (b) as a function of temperature, the sample is heated from 20 to 200 °C with a heating rate of 10 °C/min, (c) at 200 °C, and (d) at 80 °C.*

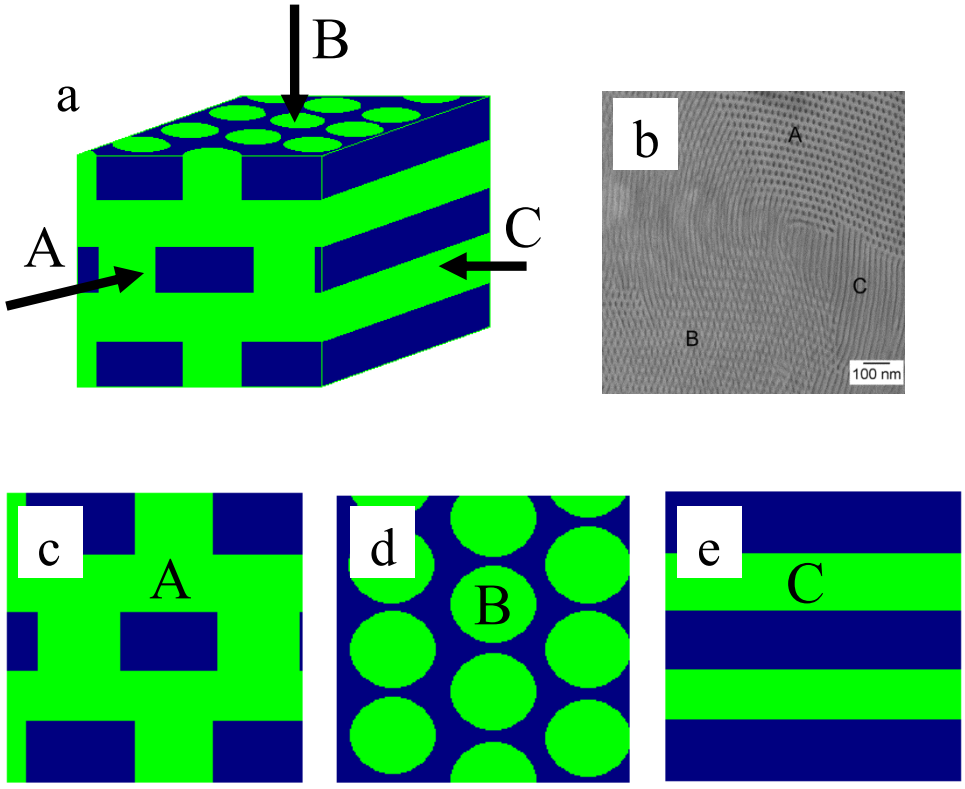

Figure 4.5. *Schematic representation of (a) the HPL morphology, (c) projection parallel to the perforated layers shown with perforations, (d) projection normal to the perforated layers, and (e) projection parallel to the perforated layers shown without perforations; (b) TEM micrograph of PS-b-P4VP(PDP)$_{0.5}$, $f_{P4VP(PDP)}$ = 0.37, M_{total} = 43 100 g mol^{-1} based on S4VP-33.7k. The sample acquires the HPL structure at room temperature and the letters A, B, and C denote different projections through the HPL unit cell.*

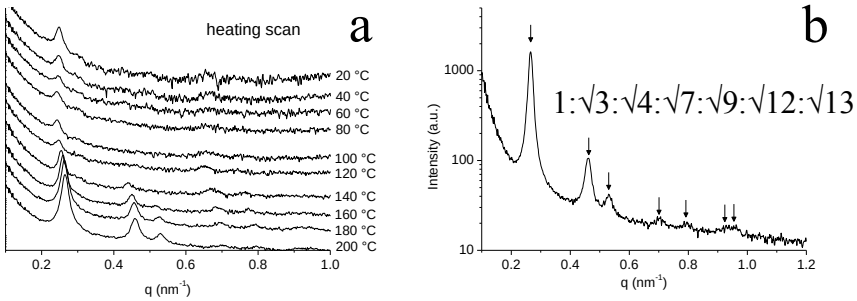

Figure 4.6. *SAXS intensity patterns for PS-b-P4VP(PDP)$_{0.3}$, $f_{P4VP(PDP)}$ = 0.31, M_{total} = 39 300 g mol^{-1} based on S4VP-33.7k (a) as a function of temperature, the sample is heated from 20 to 200 °C with a heating rate of 10 °C/min and (b) at 200 °C. There is an order-order transition around 140 °C, and at higher temperatures the sample has CYL morphology as evidenced by reflections positioned in the relative ratio 1:√3:√4:√7:√9:√12:√13. To determine the low temperature morphology of the sample, TEM is employed as a supplementary technique.*

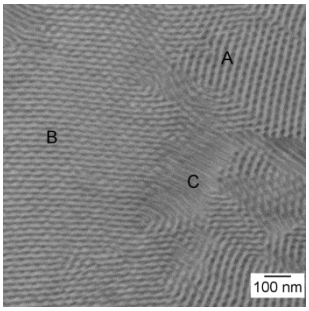

Figure 4.7. *TEM micrograph of PS-b-P4VP(PDP)$_{0.3}$, $f_{P4VP(PDP)}$ = 0.31, M_{total} = 39 300 g mol^{-1} based on S4VP-33.7k. The sample acquires the HPL structure at room temperature and the letters A, B, and C denote different projections through the HPL unit cell.*

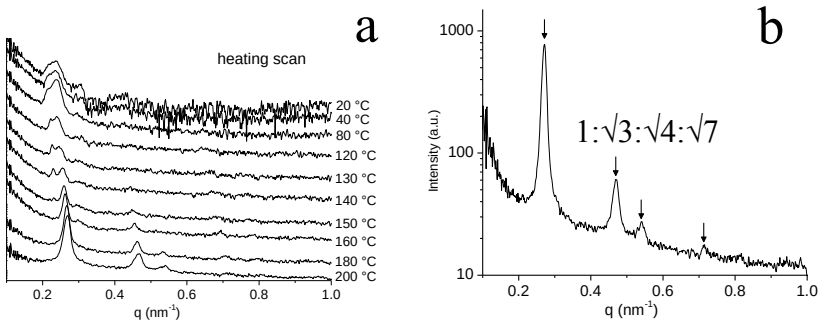

Figure 4.8. *SAXS intensity patterns for PS-b-P4VP(PDP)$_{0.4}$, $f_{P4VP(PDP)}$ = 0.34, M_{total} = 41 200 g mol^{-1} based on S4VP-33.7k (a) as a function of temperature, the sample is heated from 20 to 200 °C with a heating rate of 10 °C/min and (b) at 200 °C. There is an order-order transition around 140 °C and at higher temperatures the sample has CYL morphology as evidenced by reflections positioned in the relative ratio 1:√3:√4:√7. To determine the low temperature morphology of the sample, TEM is employed as a supplementary technique.*

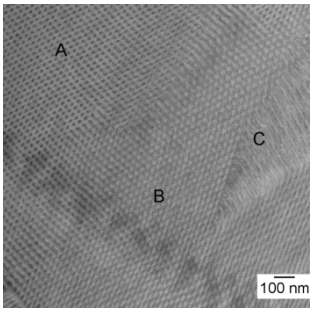

Figure 4.9. *TEM micrograph of PS-b-P4VP(PDP)$_{0.4}$, $f_{P4VP(PDP)}$ = 0.34, M_{total} = 41 200 g mol^{-1} based on S4VP-33.7k. The sample acquires the HPL structure at room temperature and the letters A, B, and C denote different projections through the HPL unit cell.*

The stability of the HPL phase over a broad composition range may come as a surprise considering the fact that HPL is not an equilibrium structure for neat diblock copolymers. Furthermore, as shown in the previous chapter, not a single PS-*b*-P4VP(PDP)$_x$ sample from the opposite side of the phase diagram, where P4VP(PDP)$_x$ represents the majority component, adopts the HPL morphology at room temperature. This unique behavior can, however, be explained by the specific supramolecular nature of the PS-*b*-P4VP(PDP)$_x$ complexes. PDP molecules bind to the P4VP monomer units and occupy the space around the P4VP chain forcing it to adopt more stretched conformations. PDP molecules present near the interface between PS and P4VP(PDP)$_x$ can push block copolymer chains from each other, thus increasing the distance between the junction points. This further results in a tendency of the system to create a curved interface, with P4VP(PDP)$_x$ chains positioned on the convex side. For complexes where P4VP(PDP)$_x$ represents the majority component this can be easily accommodated (Figure 4.10a). The opposite situation, *i.e.*, the formation of the structures in which P4VP(PDP)$_x$ chains are located on the concave side of the interface, is, naturally, unfavorable (Figure 4.10b). Hence, PS-*b*-P4VP(PDP)$_x$ complexes with $f_{P4VP(PDP)} < 0.5$ will rather form a straight interface than a curved interface with P4VP(PDP)$_x$ blocks on the concave side. This explains the observed asymmetry in the PS-*b*-P4VP(PDP)$_{1.0}$ phase diagram (the CYL region is narrower if P4VP(PDP)$_{1.0}$ represents a minority component)[22] or the appearance of the LAM phase in similar supramolecular complexes of polyisoprene-*block*-poly(2-vinylpyridine)(octyl gallate) (PI-*b*-P2VP(OG)) already at $f_{P2VP(OG)}$ = 25.6%.[23] The HPL structure is exceptional because its interfaces are straight or curved in such a manner that the minority component is located on the convex side. This explains why the HPL structure is stabilized in our system and occupies a relatively large composition range (Figure 4.10c). Theoretical studies demonstrated that in homopolymer/block copolymer blends, the CYL phase is favored when the homopolymer is added to a matrix of the CYL phase since the homopolymer chains fill the corners of Wigner–Seitz cells and relieve the packing frustrations.[37, 38] Following a similar mechanism, the

HPL phase can be stabilized if the homopolymer is added to a minority component, since in the HPL phase the majority component forms the hexagonally packed channels. Analogously, the presence of PDP in the minority component of PS-*b*-P4VP(PDP)$_x$ complexes may relieve the packing frustrations and stabilize the HPL phase.

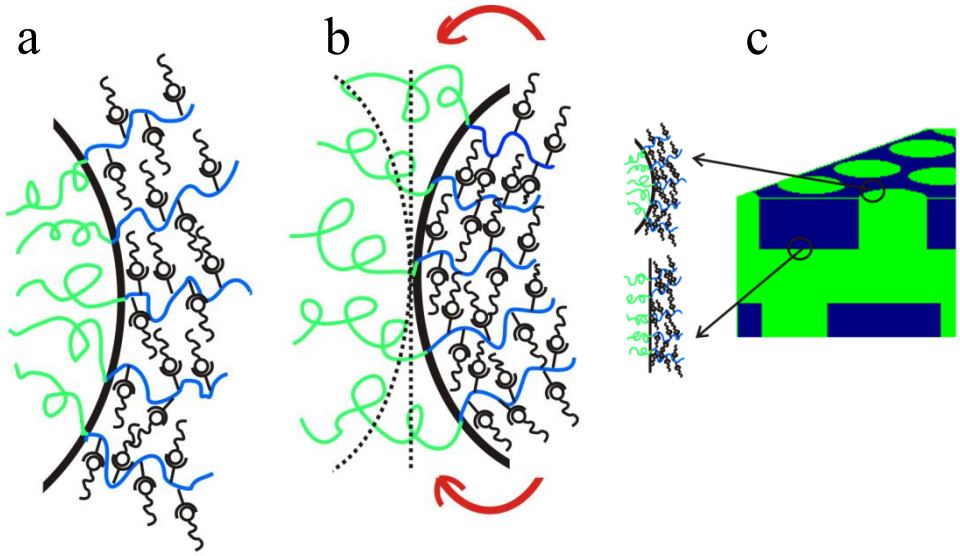

Figure 4.10. *Schematic representation of the situation when (a) P4VP(PDP)$_x$ block represents a majority component in the complex and this situation is favorable, (b) P4VP(PDP)$_x$ block represents a minority component in the complex. This situation is unfavorable and the complexes will tend to either straighten or bend the interfaces to the other side. The HPL structure is atypical since its interfaces are straight or curved with the minority block on the convex side (c).*

To further investigate the phase behavior of PS-*b*-P4VP(PDP)$_x$ complexes, another sample is prepared from block copolymer S4VP-41.0k with x = 0.5 and $f_{P4VP(PDP)}$ = 0.37. The composition of this sample is identical to the previously described one, but its total molar mass is somewhat higher. Dynamic mechanical measurements indicate the reversible HPL-CYL order-order transition to occur in the range between 130 and 150 °C (Figure 4.11), which is also confirmed by SAXS during the cooling scan (Figure 4.12a). At higher temperatures the sample adopts the CYL

morphology which is indicated by the SAXS peaks positioned in the ratio 1:√3:√4 (Figure 4.12b) with the distance between cylinders of 27.8 nm ($q^* = 0.261$ nm^{-1}). The low temperature SAXS pattern (Figure 4.12c) is similar to the low temperature SAXS pattern of the previously described sample (Figure 4.4d): three peaks are found at the positions q^*, $1.08q^*$, and $2q^*$, which can be attributed to the HPL phase. The HPL morphology is further confirmed by TEM. Figure 4.12d depicts different projections through the HPL unit cell: parallel (region A and C) and normal (region B) to the perforated layers. Hence, the HPL morphology encompasses not only a considerable composition range, but it also extends in the vertical (χN) direction in the PS-*b*-P4VP(PDP)$_x$ phase diagram.
Additional TEM images that unambiguously confirm the HPL morphology of the previously described samples are provided in Figure 4.13.

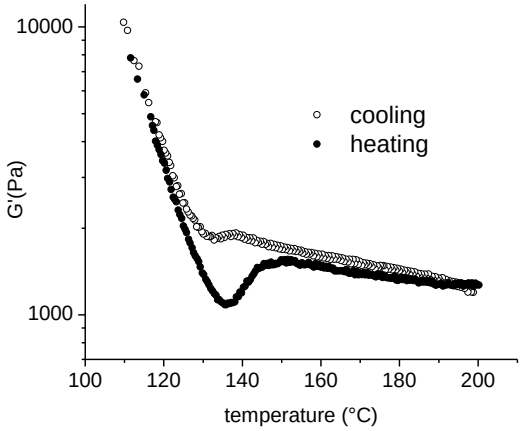

Figure 4.11. *Temperature dependence of the dynamic storage modulus (G') for PS-b-P4VP(PDP)$_{0.5}$, $f_{P4VP(PDP)} = 0.37$, $M_{total} = 52\ 600$ g mol^{-1} based on S4VP-41.0k. The frequency of shearing is 0.1 Hz, the strain amplitude 0.1%, and the heating/cooling rate is 1 °C/min.*

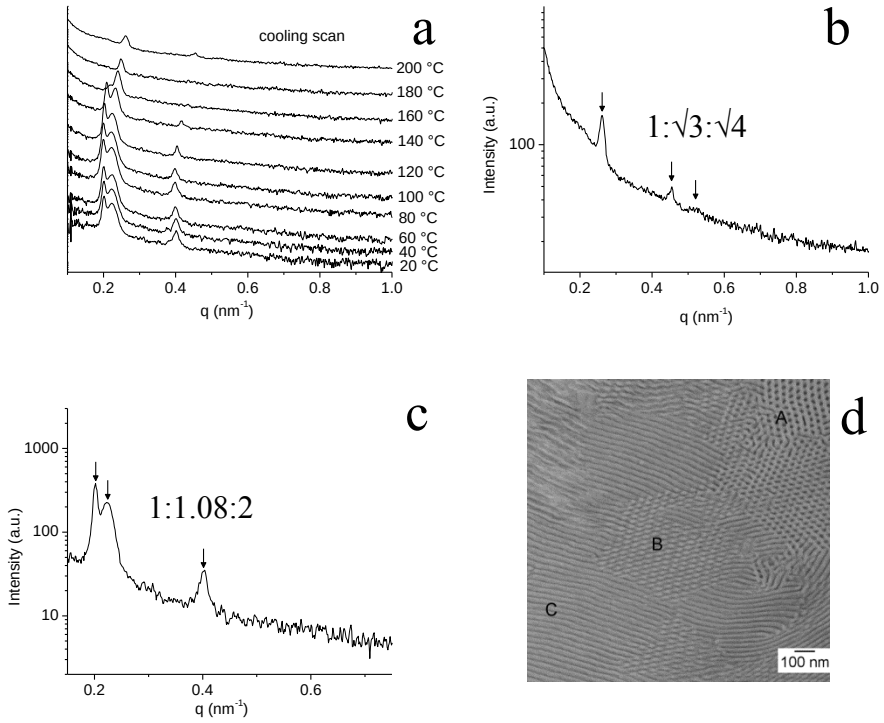

Figure 4.12. *Morphological characterization of PS-b-P4VP(PDP)$_{0.5}$, $f_{P4VP(PDP)}$ = 0.37, M_{total} = 52 600 g mol^{-1} based on S4VP-41.0k. (a) SAXS intensity patterns as a function of temperature, the sample is cooled from 200 to 20 °C with a cooling rate of 10 °C/min, (b) SAXS curve at 200 °C. The sample acquires CYL morphology at 200 °C, as evidenced by reflections positioned in the relative ratio 1:√3:√4, (c) SAXS curve at 20 °C indicating the HPL morphology of the sample at room temperature, which is further evidenced by TEM (d). Letters A, B, and C denote different projections through the HPL unit cell.*

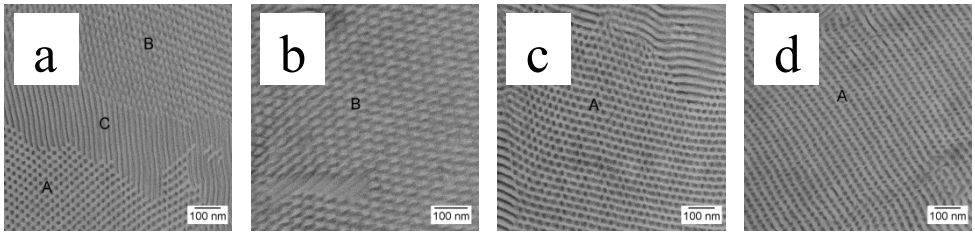

Figure 4.13. *TEM micrographs of (a, b, c) PS-b-P4VP(PDP)$_{0.5}$, $f_{P4VP(PDP)}$ = 0.37, M_{total} = 43 100 g mol^{-1} based on S4VP–33.7k, (d) PS-b-P4VP(PDP)$_{0.5}$, $f_{P4VP(PDP)}$ = 0.37, M_{total} = 52 600 g mol^{-1} based on S4VP–41.0k. Letters A, B, and C denote different projections through the HPL unit cell.*

The next series of samples is made from the block copolymer S4VP-45.6k with x = 1.0 and 1.2; thus, $f_{P4VP(PDP)}$ = 0.35 and 0.39. These compositions ($f_{P4VP(PDP)}$) are similar to that of the previously described samples, and accordingly, similar phase behavior is expected. Because the ratio between the molar mass of the PS and P4VP block in the block copolymer precursor is higher than in the previous cases, a higher amount of PDP is required to reach the same $f_{P4VP(PDP)}$. This modifies the phase behavior in such a way that at low temperatures now the LAM instead of the HPL phase is found, whereas at higher temperatures the HPL replaces the CYL phase. Figure 4.14 shows the temperature dependence of G' for the sample based on S4VP-45.6k with x = 1.0 and $f_{P4VP(PDP)}$ = 0.35. The results from the cooling and heating scan imply that the reversible order-order transition takes place between 120 and 150 °C. Below 120 °C the sample has a LAM structure, as confirmed by SAXS (Figure 4.15a) and TEM (Figure 4.15b). The SAXS peaks are positioned in the ratio 1:2:4 and the first-order reflection appears at q^* = 0.207 nm^{-1} (hence, the lamellar period is 30.3 nm). Above 150 °C, the lamellae are converted into the hexagonally perforated layers, as evidenced by SAXS (Figure 4.15c) and TEM (Figure 4.15d). The SAXS reflections at q^*, 1.08q^*, and 2q^* indicate the HPL phase, while the projections parallel (region A) and normal (region B) to the perforated layers are displayed in the TEM micrograph. Similar phase behavior is found in the complex based on S4VP-45.6k with x = 1.2 and $f_{P4VP(PDP)}$ = 0.39. The low temperature SAXS curve (Figure 4.16a) contains peaks at q^*, 2q^*, 3q^*, and 4q^* demonstrating the LAM structure, which is further confirmed by TEM (Figure 4.16b). The lamellar period of 30.8 nm follows from q^* = 0.204 nm^{-1}. The SAXS

pattern of the complex at higher temperatures (Figure 4.16c) contains the peaks in the ratio 0.92:1:1.08:2 which again is a clear signature of the HPL phase. The alternating layers of the PS and the perforated P4VP domains depicted in the TEM image (Figure 4.16d) confirm this morphological assignment.

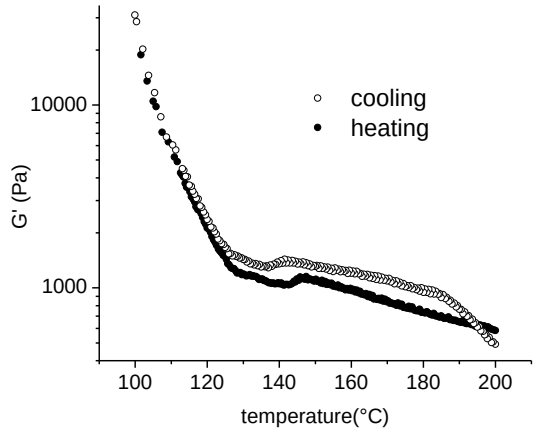

Figure 4.14. *Temperature dependence of the dynamic storage modulus (G') for PS-b-P4VP(PDP)$_{1.0}$, $f_{P4VP(PDP)}$ = 0.35, M_{total} = 61 800 g mol^{-1} based on S4VP-45.6k. The frequency of shearing is 0.1 Hz, the strain amplitude 0.1%, and the heating/cooling rate is 1 °C/min.*

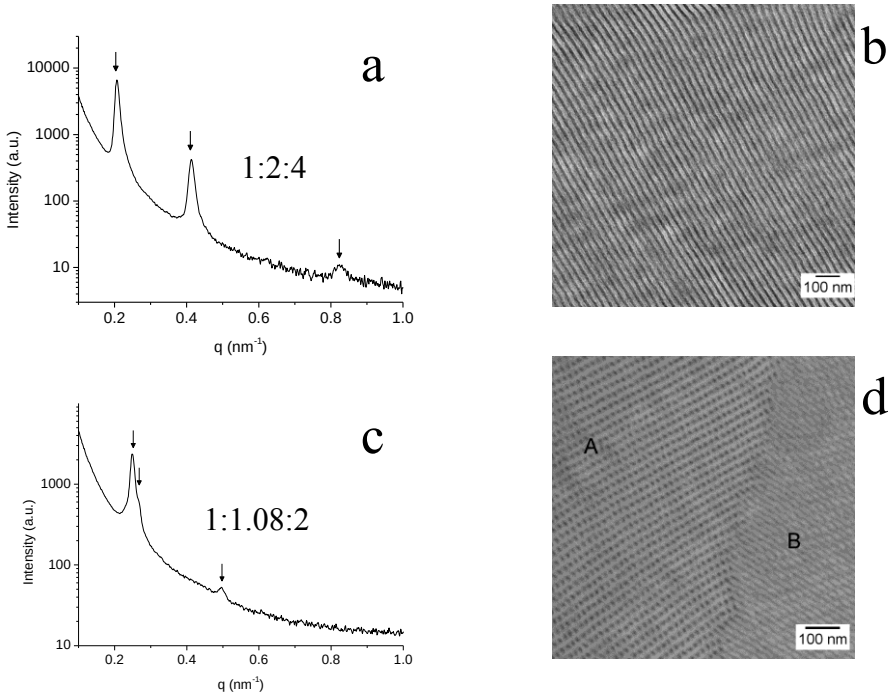

Figure 4.15. *Morphological characterization of PS-b-P4VP(PDP)$_{1.0}$, $f_{P4VP(PDP)}$ = 0.35, M_{total} = 61 800 g mol^{-1} based on S4VP-45.6k. (a) SAXS intensity pattern at 20 °C. The sample has LAM morphology at 20 °C, which is also evidenced by TEM (b). At higher temperatures the sample acquires HPL structure, and this is confirmed by SAXS (c) and TEM (d). Letters A and B denote different projections through the HPL unit cell.*

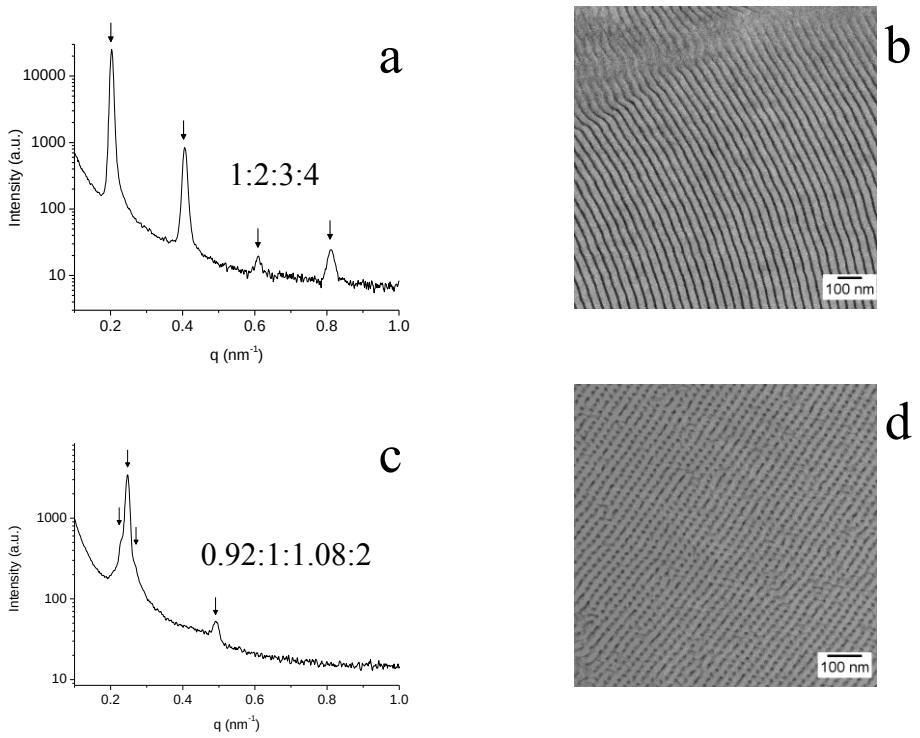

Figure 4.16. *Morphological characterization of PS-b-P4VP(PDP)$_{1.2}$, $f_{P4VP(PDP)}$ = 0.39, M_{total} = 65 050 g mol^{-1} based on S4VP-45.6k. (a) SAXS intensity pattern at 20 °C. The sample has LAM morphology at 20 °C, which is also evidenced by TEM (b). At higher temperatures the sample acquires HPL structure, and this is confirmed by SAXS (c) and TEM (d).*

Finally, supramolecular complexes PS-*b*-P4VP(PDP)$_x$ from the block copolymer S4VP-67.0k with x = 0.1, 0.2, and 0.3, hence $f_{P4VP(PDP)}$ = 0.30, 0.35, and 0.39, respectively, are prepared to examine the influence of the molar mass of the block copolymer precursor on the phase behavior of the system. The compositions ($f_{P4VP(PDP)}$) are similar to the previously described samples, but the molar mass is somewhat higher. The morphological characterization of the sample with x = 0.1 is given in Figure 4.17. The diffraction peaks in the SAXS pattern appear at q^*, $\sqrt{3}q^*$, $\sqrt{4}q^*$, and $\sqrt{7}q^*$, which is a clear signature of the CYL phase (Figure 4.17a). The

distance between the cylinders is calculated to be 55.2 nm from $q^* = 0.131$ nm^{-1}. The SAXS patterns remain identical in the whole temperature range examined and order-order transitions are not observed. The TEM micrograph (Figure 4.17b) shows the P4VP cylinders packed hexagonally in the PS matrix. The sample with $x = 0.2$ and $f_{P4VP(PDP)} = 0.35$ exhibits identical phase behavior as the $x = 0.1$ sample. It also has the CYL morphology in the whole temperature range investigated. When x is increased to 0.3, and accordingly, $f_{P4VP(PDP)}$ to 0.39, the morphology of the supramolecular complex becomes LAM. The diffraction peaks in the SAXS pattern (Figure 4.18a) at q^*, $2q^*$, $3q^*$, $4q^*$, $5q^*$, and $6q^*$ (lamellar period is calculated to be 47.9 nm) and alternating PS and P4VP(PDP)$_{0.3}$ lamellae shown in the TEM micrograph (Figure 4.18b) confirm the morphological assignment. This may imply that the HPL phase does not exist in supramolecular complexes PS-*b*-P4VP(PDP)$_x$ if the molar mass of the starting block copolymer exceeds a critical value. On the other hand, it may also be related to the composition of the parent diblock copolymer requiring only a small amount of PDP to reach the composition range of interest. This latter conclusion may well be the most likely one as it is in line with the geometric argument that a curved interface with the minority comb-shaped supramolecular block at the convex side is favored by the comblike molecular architecture (Figure 4.10).

The morphological behavior of PS-*b*-P4VP(PDP)$_x$ complexes between the LAM and CYL region with $f_{P4VP(PDP)} < 0.5$ is summarized in Table 4.2 and Figure 4.19.

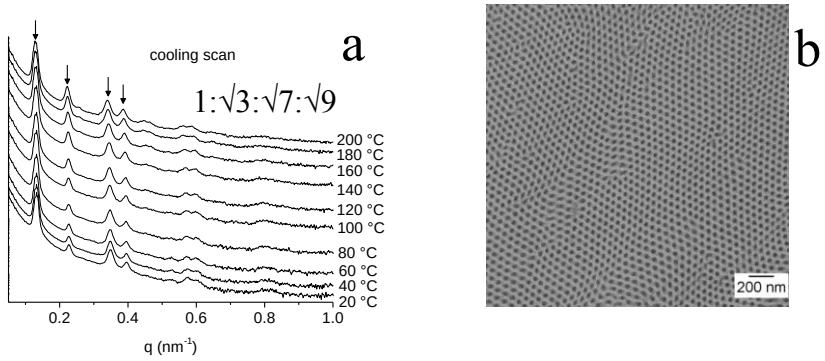

Figure 4.17. *Morphological characterization of PS-b-P4VP(PDP)$_{0.1}$, $f_{P4VP(PDP)}$ = 0.30, M_{total} = 71 900 g mol^{-1} based on S4VP-67.0k. (a) SAXS intensity pattern as a function of temperature, the sample is cooled from 200 to 20 °C with a cooling rate of 10 °C/min. In the whole temperature range, the sample exhibits CYL morphology, as evidenced by reflections positioned in the relative ratio 1:√3:√7:√9. °C. The CYL morphology of the sample is imaged by TEM (b).*

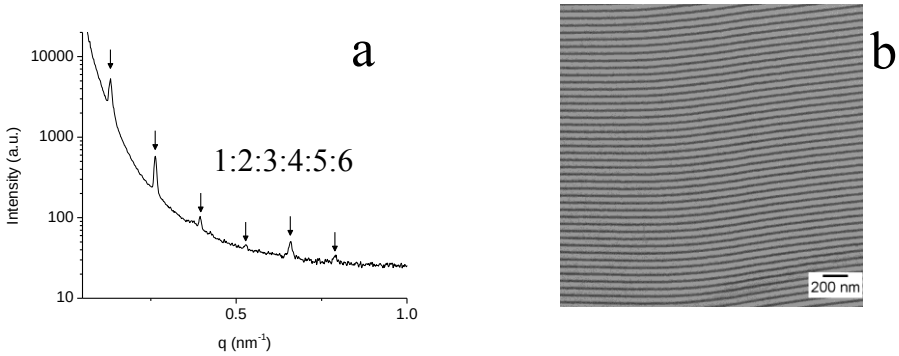

Figure 4.18. *Morphological characterization of PS-b-P4VP(PDP)$_{0.3}$, $f_{P4VP(PDP)}$ = 0.39, M_{total} = 81 800 g mol^{-1} based on S4VP-67.0k. (a) SAXS intensity pattern at 180 °C. The sample has a LAM morphology according to SAXS (a) and TEM (b) results.*

Table 4.2. *Summary of the morphological characterization of supramolecular complexes PS-b-P4VP(PDP)$_x$*

block copolymer code	***x***	$f_{P4VP(PDP)}$	**low T morphology**	**high T morphology**
S4VP-33.7k	0.3	0.31	HPL	CYL
S4VP-33.7k	0.4	0.34	HPL	CYL
S4VP-33.7k	0.5	0.37	HPL	CYL
S4VP-41.0k	0.5	0.37	HPL	CYL
S4VP-45.6k	1.0	0.35	LAM	HPL
S4VP-45.6k	1.2	0.39	LAM	HPL
S4VP-67.0k	0.1	0.30	CYL	CYL
S4VP-67.0k	0.2	0.35	CYL	CYL
S4VP-67.0k	0.3	0.39	LAM	LAM

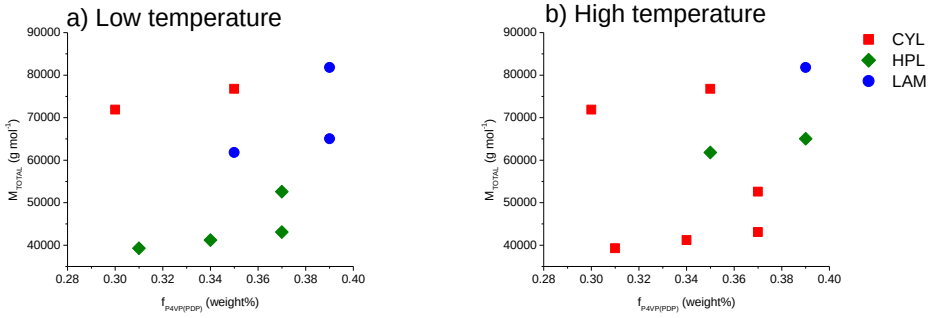

Figure 4.19. *Phase diagram of supramolecular complexes PS-b-P4VP(PDP)$_x$ at low (a) and high (b) temperature. The total molar mass of the complex is given at the y-axis while the weight fraction of P4VP(PDP) block is given at the x-axis.*

4.4 Conclusion

A comprehensive study of the phase behavior of supramolecular complexes PS-*b*-P4VP(PDP)$_x$ with P4VP(PDP)$_x$ as a minority component in the composition range between the CYL and LAM morphology is conducted. Several samples with the HPL structure as equilibrium state have been identified. The HPL phase covers a rather broad composition range. In the set of samples prepared from the block copolymer S4VP-33.7k, for instance, it extends from $f_{P4VP(PDP)} = 0.31$ to $f_{P4VP(PDP)} = 0.37$, and presumably even further. This atypical phase behavior can be explained by the presence of PDP "side chain" molecules in the minority component of the complex, where the HPL morphology reliefs the packing frustrations. Besides the composition, the total molar mass and the amount of PDP (x) are important factors that determine the phase behavior of the complexes. Finally, the HPL phase spans a considerable χN range, but above a certain value of the molar mass of the starting block copolymer, it seems to disappear from the phase diagram. This study reveals once more the exciting phase behavior of PS-*b*-P4VP(PDP)$_x$ complexes, which provides a powerful tool to design tailor-made structures for numerous practical applications.

4.5 References

1. Bates FS, Fredrickson GH. Annu Rev Phys Chem 1990;41:525-527.
2. Hamley IW. The Physics of Block Copolymers. Oxford: Oxford University Press, 1998.
3. Abetz V, Simon P. Phase Behaviour and Morphologies of Block Copolymers. Adv Polym Sci, vol. 189: Springer Berlin / Heidelberg, 2005. pp. 125-212.
4. Hamley IW. Nanotechology 2003;14:39-54.
5. Crossland EJW, Kamperman M, Nedelcu M, Ducati C, Wiesner U, Smilgies DM, et al. Nano Lett 2009;9(8):2807-2812.
6. Vignolini S, Yufa NA, Cunha PS, Guldin S, Rushkin I, Stefik M, et al. Adv Mater 2012;24(10):OP23-OP27.
7. Hajduk DA, Harper PE, Gruner SM, Honeker CC, Kim G, Thomas EL, et al. Macromolecules 1994;27(15):4063-4075.
8. Schulz MF, Bates FS, Almdal K, Mortensen K. Phys Rev Lett 1994;73(1):86-89.
9. Hamley IW, Koppi KA, Rosedale JH, Bates FS, Almdal K, Mortensen K. Macromolecules 1993;26:5959-5970.
10. Foerster S, Khandpur AK, Zhao J, Bates FS, Hamley IW, Ryan AJ, et al. Macromolecules 1994;27:6922-6935.
11. Tyler CA, Morse DC. Phys Rev Lett 2005;94:208302.
12. Ranjan A, Morse DC. Phys Rev E 2006;74:011803.
13. Kim MI, Wakada T, Akasaka S, Nishitsuji S, Saijo K, Hasegawa H, et al. Macromolecules 2008;41(20):7667-7670.
14. Matsen MW, Schick M. Phys Rev Lett 1994;72(16):2660-2663.
15. Laradji M, Shi A-C, Noolandi J, Desai RC. Macromolecules 1997;30:3242-3255.
16. Tanaka H, Hasegawa H, Hashimoto T. Macromolecules 1991;24:240-251.
17. Mayes AM, Russell TP, Satija SK, Majkrzak CF. Macromolecules 1992;25(24):6523-6531.
18. Torikai N, Takabayashi N, Noda I, Koizumi S, Morii Y, Matsushita Y. Macromolecules 1997;30(19):5698-5703.
19. Bodycomb J, Yamaguchi D, Hashimoto T. Macromolecules 2000;33(14):5187-5197.

20. Dobrosielska K, Wakao S, Suzuki J, Noda K, Takano A, Matsushita Y. Macromolecules 2009;42(18):7098-7102.
21. Chen S-C, Kuo S-W, Jeng US, Su C-J, Chang F-C. Macromolecules 2010;43(2):1083-1092.
22. Valkama S, Ruotsalainen T, Nykänen A, Laiho A, Kosonen H, ten Brinke G, et al. Macromolecules 2006;39(26):9327-9336.
23. Bondzic S, Polushkin E, Ruokolainen J, ten Brinke G. Polymer 2008;49:2669-2677.
24. Nandan B, Vyas MK, Böhme M, Stamm M. Macromolecules 2010;43(5):2463-2473.
25. Sakurai S, Kawada H, Hashimoto T, Fetters LJ. Macromolecules 1993;26(21):5796-5802.
26. Kim JK, Lee HH, Ree M, Lee K-B, Park Y. Macromol Chem Phys 1998;199(4):641-653.
27. Krishnamoorti R, Modi MA, Tse MF, Wang HC. Macromolecules 2000;33(10):3810-3817.
28. Wang C-Y, Lodge TP. Macromolecules 2002;35(18):6997-7006.
29. Lin S-H, Ho C-C, Su W-F. Soft Matter 2012;8(18):4890-4893.
30. Hajduk DA, Gruner SM, Rangarajan P, Register RA, Fetters LJ, Honeker C, et al. Macromolecules 1994;27(2):490-501.
31. Ryu DY, Lee DH, Jeong U, Yun S-H, Park S, Kwon K, et al. Macromolecules 2004;37(10):3717-3724.
32. Mäki-Ontto R, de Moel K, de Odorico W, Ruokolainen J, Stamm M, ten Brinke G, et al. Adv Mater 2001;13:117-121.
33. Ikkala O, ten Brinke G. Science 2002;295:2407-2409.
34. Hsueh H-Y, Chen H-Y, She M-S, Chen C-K, Ho R-M, Gwo S, et al. Nano Lett 2010;10(12):4994-5000.
35. Hsueh H-Y, Ho R-M. Langmuir 2012;28(22):8518-8529.
36. Ruotsalainen T, Turku J, Hiekkataipale P, Vainio U, Serimaa R, ten Brinke G, et al. Soft Matter 2007;3:978-985.
37. Matsen MW. Macromolecules 1995;28:5765-5773.
38. Matsen MW. Phys Rev Lett 1995;74:4225-4228.
39. Borsboom M, Bras W, Cerjak I, Detollenaere D, Glastra Van Loon D, Goedtkindt P, et al. J Synchrotron Radiat 1998;5:518-520.
40. Bras W, Dolbnya IP, Detollenaere D, van Tol R, Malfois M, Greaves GN, et al. J Appl Crystallogr 2003;36:791-794.

41. Khandpur AK, Foerster S, Bates FS, Hamley IW, Ryan AJ, Bras W, et al. Macromolecules 1995;28:8796-8806.
42. Ahn J-H, Zin W-C. Macromolecules 2000;33(2):641-644.
43. Ahn J-H, Zin W-C. Macromol Res 2003;11:152-156.
44. Ahn J-H, Zin W-C. Macromolecules 2002;35(27):10238-10240.
45. Lai C, Loo Y-L, Register RA, Adamson DH. Macromolecules 2005;38(16):7098-7104.
46. Hajduk DA, Takenouchi H, Hillmyer MA, Bates FS, Vigild ME, Almdal K. Macromolecules 1997;30(13):3788-3795.

Chapter 5

Supramolecular Route to Well-Ordered Metal Nanofoams

Metal nanofoams with a porosity above 50% v/v have recently attracted great interest in materials science due to their interesting properties. We demonstrate a new straightforward route to prepare such nanofoams using diblock copolymer-based PS-block-P4VP(PDP) supramolecules that self-assemble into a bicontinuous gyroid morphology, consisting of PS network channels in a P4VP(PDP) matrix. After dissolving the PDP, the P4VP collapses onto the PS struts and a free standing bicontinuous gyroid template of thickness of 50–100 μm and interconnected, uniformly sized pores is formed. The hydrophilic P4VP corona facilitates the penetration of water-based plating reagents into the porous template and enables a successful metal deposition. After plating, the polymer is simply degraded by heating, resulting in a well-ordered inverse gyroid nickel foam. Essential to this approach is the removal of only one part of the matrix (i.e., PDP). Therefore the template accounts for 50% v/v or more. The porosity characteristics (amount, size of pores) can be tuned by selecting the appropriate copolymer and by adjusting the amount of PDP.

Part of this chapter was published in: *ACS Nano 2011, 5, 6339-6348.*
Part of this chapter is submitted to: *Journal of Visualized Experiments 2013.*

5.1 Introduction

As discussed in chapter 1, nanoporous metal foams represent a new, very promising class of materials that combine the properties of metals and the properties of nanoporous materials. This unique combination allow nanoporous metal foams to be used for a large number of possible applications as, for example, high power density batteries, substitutes for platinum group catalysts, hydrogen storage materials, actuators, *etc*.[1]

In the case of actuators, charge is injected at the surfaces, resulting in the enhancement of surface stresses.[2, 3] When charge is injected, a narrow space-charge layer of atomic dimensions is formed at the surface. In this layer, the electronic density of states changes, which modifies the atomic bonding potentials. As a result, the surface layer tends to favor a lateral atomic spacing that differs from that of the bulk, creating a surface stress. Despite the limited size of space charge regions in metals due to the efficient electronic screening, it has been shown that these tunable surface stresses can be exploited in highly porous materials when the ligament (subunit) sizes are on the order of tens of nanometers.[4, 5] This has recently led to a new class of actuators: nanoporous metals.[6] When immersed in an electrolyte, nanoporous metal expands and contracts reversibly if an external bias voltage is applied. An intriguing feature of nanoporous actuator materials is that the overall behavior is not a direct result of the electromechanical behavior of the nanoscale ligaments. Instead, the macroscopic functional properties emerge as a result of the interaction of individual subunits, which is strongly dictated by the topological information of the nanostructural architecture, that is, the morphology and connectivity of the nanoscale ligaments.

In chapter 1, we described in detail several methods for the preparation of nanoporous metals, such as, dealloying,[7-9] sol−gel approaches,[1, 10] nanosmelting,[11, 12] and combustion synthesis.[13] A common characteristic of these techniques is that they render metal nanofoams with highly disordered nanocellular architecture. It is well-known from studies on the mechanical behavior of structural cellular metals and metallic foams that disordered architectures are not able to effectively transmit stresses from the ligament scale to the overall (macro) scale, resulting in poor mechanical properties.[14-16] In the present paper, we demonstrate how the unique self-assembly properties of block copolymer-based

supramolecules may be employed to synthesize nanoporous metals having a well-defined and ordered cellular architecture with porosities exceeding 50% v/v.

It has been already mentioned in previous chapters that block copolymers, depending on the number of blocks, their chain length and flexibility, volume fraction, and the extent of repulsion between the chemically connected blocks, self-assemble into a variety of structures with internal length scales ranging from tens to hundreds or more nanometers.[17-19] Furthermore, block copolymers containing selectively degradable block are versatile precursors to nanoporous materials.[20] An attractive method to eliminate the targeted block is provided by self-assembled supramolecules, where nanoporous structures may be obtained by simple dissolution. Suitable block copolymer-based supramolecules are obtained by hydrogen bonding side groups to one of the blocks of a diblock copolymer, which are then removed by a selective solvent after the self-assembly has taken place.[21, 22] That the morphology of these systems can be tailored by a simple variation of the relative volume fraction of the side groups is an important additional asset of this approach.[23] The generated nanoporous materials retain the originally ordered morphology of the precursor and, consequently, provide ample opportunities for nanotechnological applications.[24-26] This approach is conceptually similar to the generation of nanoporous structures from diblock copolymer/homopolymer blends of polystyrene-*block*-polymethylmethacrylate and polymethylmethacrylate, PS-*b*-PMMA/PMMA, *via* selective removal of homopolymer PMMA by acetic acid.[27]

The cylindrical morphology can be, for instance, used as a template for the fabrication of nanowires, provided the cylinders have a perpendicular orientation to the substrate surface.[25, 26] A way to create nanoporous structures that do not involve alignment issues is to use continuous morphologies.[24, 28] Hashimoto *et al.* were the first to exploit the bicontinuous gyroid morphology for metal plating purposes.[29] They reported the formation of a nanoporous film by the ozonolysis of the minority phase (PI) in a gyroid forming PS-PI block copolymer/PS homopolymer blend. The nanochannels were subsequently coated with nickel. Following this, a number of studies on the preparation and potential application of gyroid-forming nanoporous structures have appeared.[24, 30-37]

Here, we report a new method for a simple and robust preparation of well-ordered gyroid metallic nanofoams. Our procedure is summarized schematically in Figure 5.1. A supramolecular complex of PS-*b*-P4VP diblock copolymer and amphiphilic PDP was used as a precursor for the nanoporous template for subsequent metal

plating. PDP molecules interact *via* hydrogen bonds with the pyridine rings to form a PS-*b*-P4VP(PDP)$_x$ complex (Figure 5.1a; the subscript *x* denotes the ratio between PDP molecules and P4VP repeat units). The block lengths of the block copolymer and the amount of PDP were selected in such a way that the self-assembly gave rise to a bicontinuous gyroid morphology with a PS network in a matrix of P4VP(PDP)$_x$ (Figure 5.1b). The PDP side chains were selectively removed in ethanol (Figure 5.1c), after which the P4VP chains collapsed onto the PS, thus forming a polar corona around the PS network struts. Subsequently, electroless deposition was performed such that the metal was distributed throughout the macroscopic thickness of the template (50−100 μm; Figure 5.1d). The metal nanofoam obtained after the removal of polymer template perserved the well-defined gyroid structure with long-range order (Figure 5.1e).

The value of the Flory–Huggins interaction parameter between polystyrene (PS) and poly(4-vinylpyridine) (P4VP) is on the order of $\chi_{S,4VP} \cong 0.35$.[38, 39] This implies that a PS-*b*-P4VP diblock copolymer will be in the strong segregation limit except for small molar masses, which therefore diminishes the possibility of a bicontinuous gyroid self-assembly.[40] However, the addition of a small amphiphilic molecule, such as 3-pentadecylphenol (PDP), to PS-*b*-P4VP appears to reduce the effective interaction parameter between the two phases, PS and P4VP(PDP), respectively, as a series of lamellar self-assembled PS-b-P4VP(PDP)$_{1.0}$ systems showed a chain length dependence of the long period that is characteristic for the intermediate segregation regime.[41] This is also corroborated by the observation that a PS-*b*-P4VP(PDP)$_{1.0}$ complex, from a PS-b-P4VP diblock copolymer with block weight average molar masses of 19.3 and 5.1 kg mol^{-1}, respectively, becomes disordered above *ca.* 170 °C. The pure diblock copolymer, for which $\chi N \approx 80$, obviously remains ordered at all accessible temperatures. These complexes therefore have a higher probability for bicontinuous gyroid structure formation. Additives can as well stabilize structures that are not found in conventional diblock copolymers, such as plumber nightmare morphology,[42] but there are no indications that this also occurs in our supramolecular system.[43]

It is very important to realize that the PS(core)–P4VP(corona) (Figure 5.1c) gyroid network occupies more than 50 vol %, and consequently, the porosity of the formed nanoporous metal foam (Figure 5.1e) is high enough to fulfill the general requirement for the formation of a metal nanofoam.[1] In contrast, the removal of the matrix-forming block from a conventional bicontinuous gyroid diblock

copolymer structure would result in a highly porous template (porosity *ca.* 65 vol %) and a correspondingly far less porous (*ca.* 35 vol %) metal nanostructure.
Additionally, in a conventional diblock copolymer approach employing, for example, diblock copolymers of PS and polyethylene oxide (PEO) or polylactide (PLA),[28] the removal of the chemically degradable matrix (PLA or PEO) from the bicontinuois gyroid morphology results in a rather hydrophobic surface of PS, which usually requires surface modification for uniform metal deposition.[44] With the supramolecular approach presented here, this issue is overcome by the presence of the hydrophilic P4VP corona that facilitates the penetration of the water-based plating reagents into the porous template.

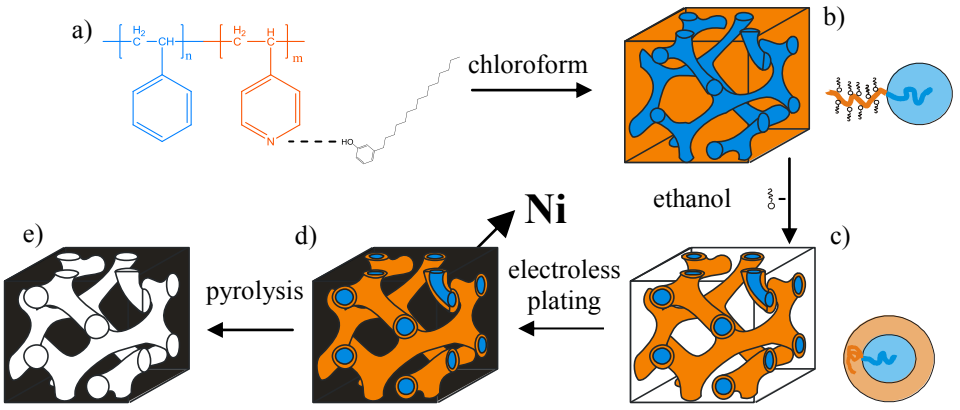

Figure 5.1. *Schematic representation of the preparation of gyroid metallic nanofoam. (a) Chemical structure of the supramolecular complex PS-b-P4VP(PDP)$_x$. (b) Bicontinuous gyroid morphology of PS-b-P4VP(PDP)$_x$. (c) Nanoporous template after the PDP removal. (d) By electroless deposition, the voids between PS struts are filled with nickel. (e) Gyroid nickel nanofoam after the polymer template removal by pyrolysis.*

5.2 Experimental section

5.2.1 Materials and sample preparation

Materials. Four different diblock copolymers of polystyrene and poly(4-vinylpyridine) were obtained from Polymer Source Inc.: S4VP-33.5k-1 (chapter 3, Table 3.1), S4VP-45.1k-1 (chapter 3, Table 3.1), S4VP-53.5k-1 (chapter 3, Table 3.1), and S4VP-59.0k (M_n(PS) = 41500 g mol^{-1}, M_n(P4VP) = 17500 g mol^{-1}, r = 2.37, M_w/M_n = 1.07). The polymers were used as received. 3-Pentadecylphenol (PDP) was acquired from Aldrich (98 wt % purity) and was recrystallized twice from petroleum ether. Tin chloride (Acros Organics, anhydrous, 98%), palladium chloride (Aldrich, 60% Pd basis), nickel sulfate (Aldrich, anhydrous, 99.99%), lactic acid (Aldrich, 85%), citric acid trisodium salt (Sigma-Aldrich, anhydrous), and borane dimethylamine complex (Aldrich, 97%) were used as received. The solvents were of analytical grade.

Preparation of nanoporous polymer films. Films of the supramolecular complexes PS-*b*-P4VP(PDP) were prepared according to the procedure described in chapter 3. The low molecular weight amphiphiles were removed by stirring a piece of the film in ethanol for three days at room temperature, resulting in the formation of the nanoporous template for metal deposition.

Electroless nickel plating. The electroless metal plating technique that involved three steps was employed for Ni deposition onto the polymer substrate.[45, 46] The sensitization, activation and nickel plating step were conducted according to the procedure described in chapter 2. Plating was done during 1 hour at room temperature and the composition of the nickel plating bath was: nickel sulfate (Ni source, 40 g L^{-1}), sodium citrate (complexant, 20 g L^{-1}), lactic acid (buffer, complexant, 10 g L^{-1}), and dimethyl amine borane (DMAB) (reductant, 1 g L^{-1}). The pH of the nickel bath was adjusted to 7.0 using ammonium hydroxide.

Formation of nickel nanofoam. The nickel-plated sample was kept in an oven (from 1 hour up to 4 days) at 350 °C. This resulted in the degradation of the polymer template and exposure of the nickel network.

5.2.2 Characterization methods

Transmission electron microscopy (TEM) was performed on a Philips CM12 transmission electron microscope operating at an accelerating voltage of 120 kV.

High-resolution transmission electron microscopy was performed on Jeol-JEM-2010F microscope. Samples were prepared according to the procedure described in chapter 2. To obtain contrast, samples without metal were stained with iodine (45 min).

^{1}H-NMR spectra in $CDCl_3$ were recorded on a 400 MHz Varian VXR operating at room temperature. The samples of the supramolecular complexes before and after PDP removal were prepared by dissolution of a piece of the film in $CDCl_3$.

Temperature-modulated differential scanning calorimetry was performed using a DSC Q1000 (TA Instruments). A modulated mode with heating/cooling rate of 1 °C min^{-1}, an oscillation amplitude of 0.5 °C, and an oscillation period of 60 s was used. Samples were first equilibrated at –30 °C, heated to 180 °C, cooled to –30 °C, and then heated again to 180 °C. Data taken from the second heating cycle were used for evaluation.

The nitrogen adsorption–desorption isotherms were determined on a Sorptomatic 1990 Thermo Finningen at 77 K. The sample was outgassed for 8 h at room temperature and for 18 h at 70 °C. The appropriate software (WinADP) and various models were used to analyze the obtained isotherms.[47-50] The specific surface area, S_{BET}, was calculated according to the Brunauer–Emmett–Teller (BET) method from the linear part of the nitrogen adsorption isotherm ($0.05 < p/p_0 < 0.25$). The pore size distribution was calculated according to the Dollimore and Heal method.

Mercury porosimetry was performed using a Carlo Erba 2000, software Milestone 200. The sample was dried at 50 ºC for 8 h and degassed at room temperature and pressure of 0.5 Pa for 2 h. The total pore volume, V_p, and the average pore diameter, D, were acquired from cumulative pore distribution curve. The specific surface area, S_{Hg}, was calculated on the basis of the cylindrical pore model.[51, 52]

Thermogravimetric analysis (TGA) was performed on a Perkin-Elmer thermogravimetric analyzer under the nitrogen atmosphere in a temperature range of 25−350 °C and with the heating rate of 20 °C min^{-1}.

Scanning electron microscopy and energy-dispersive analysis of X-rays were performed on a Philips XL-30S and XL-30 ESEM.

5.3 Results and discussion

5.3.1 Morphological characterization of PS-b-P4VP(PDP)$_x$ complexes

Different amounts of PDP ($0.5 \leq x \leq 1.5$) were added to a set of four different PS-*b*-P4VP diblock copolymers with a weight fraction of the P4VP block (f_{P4VP}) ranging from 0.28 to 0.30. The total molar mass of the supramolecular complexes did not exceed 150 kg mol^{-1}, and the weight fraction of the comb block ($f_{P4VP(PDP)}$) in the complexes varied from 0.50 to 0.69. The supramolecular complexes adopted the bicontinuous gyroid morphology, as evidenced by TEM.

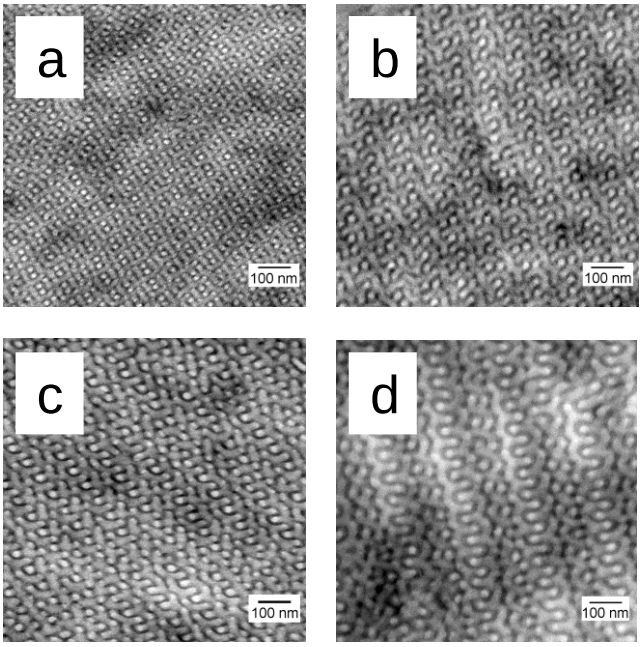

Figure 5.2. *Bright-field TEM images representing the double-wave pattern: the projection through the gyroid (211) plane. The samples are PS-b-P4VP(PDP)$_x$ supramolecular complexes with the following characteristics: a) S4VP-33.5k-1 precursor, x = 1.0, and $f_{P4VP(PDP)}$ = 0.61, b) S4VP-45.1k-1 precursor, x = 1.0, and $f_{P4VP(PDP)}$ = 0.62, c) S4VP-53.5k-1 precursor, x = 0.8, and $f_{P4VP(PDP)}$ = 0.59, and d) S4VP-59.0k precursor, x = 1.5, and $f_{P4VP(PDP)}$ = 0.69.*

Figure 5.2 shows representative bright-field TEM images of the iodine-stained ultrathin sections. The P4VP(PDP)$_x$ block domains appear dark because they are selectively stained with iodine due to the formation of a charge transfer complex. TEM images reveal the typical double-wave pattern that is known to represent the projection through the (211) plane of the gyroid unit cell. Figure 5.3 shows the wagon-wheel pattern that is characteristic for the gyroid (111) projection.

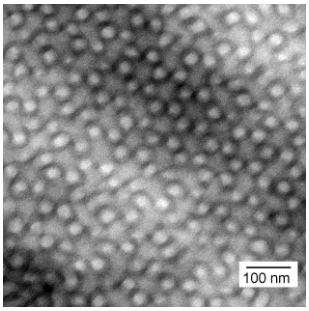

Figure 5.3. *Bright-field TEM image representing the wagon-wheel pattern: the projection through the gyroid (111) plane. The sample is PS-b-P4VP(PDP)$_{1.5}$ supramolecular complex derived from S4VP-59.0k precursor.*

5.3.2 Generation and characterization of the porous structure

By subjecting the film of the PS-*b*-P4VP(PDP)$_x$ complex to ethanol, the PDP side chains were selectively removed (Figure 5.1c).
The complete removal of PDP was proven by ^{1}H-NMR (Figure 5.4). The signals characteristic for PDP are marked in Figure 5.4a. Figure 5.4c shows the spectrum of the supramolecular complex PS-*b*-P4VP(PDP)$_x$. As expected, it is simply the sum of PDP and diblock copolymer (Figure 5.4b) spectra, and the characteristic PDP peaks are visible. However, after the ethanol treatment (Figure 5.4d), the PDP peaks are absent and the spectrum of the diblock copolymer is recovered. This confirms that the ethanol washing provides the complete removal of PDP from the sample.

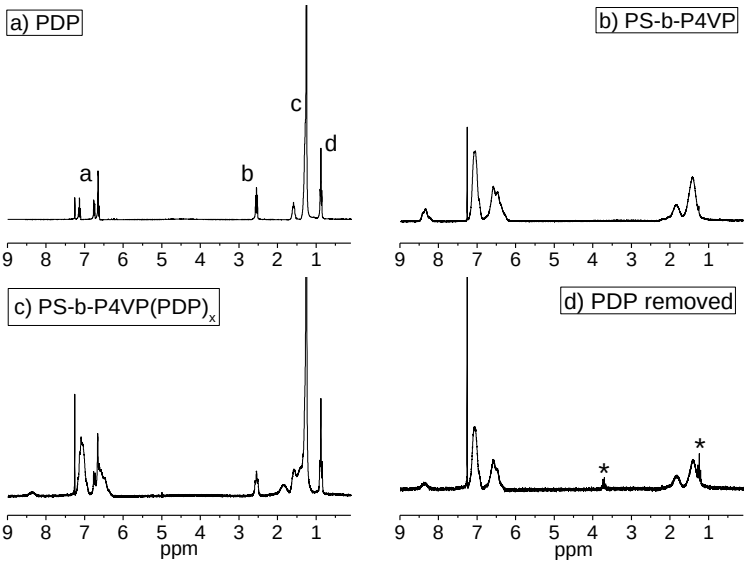

Figure 5.4. *^{1}H-NMR of a) PDP, b) PS-b-P4VP diblock copolymer, c) PS-b-P4VP(PDP)$_x$ supramolecular complex, and d) PS-b-P4VP(PDP)$_x$ after washing with ethanol; the peaks marked with an asterisk are due to residual ethanol.*

The absence of PDP after the ethanol treatment was verified using DSC as well (Figure 5.5). The DSC thermogram of pure diblock copolymer contains a T_g at 105 °C, corresponding to the PS phase, and a T_g at 146 °C, corresponding to the P4VP phase (Figure 5.5a). The thermal behavior of the supramolecular complex is significantly altered (Figure 5.5b). Due to the presence of the PDP side chains, the T_g of P4VP is strongly suppressed and it is expected to be located under the PDP melting peak situated below *ca.* 20 °C. The ethanol treated sample was found to exhibit the identical thermal behavior as the pure diblock copolymer (Figure 5.5c). The DSC data furthermore indicate that the temperature of the subsequent nickel plating step should not exceed 105 °C because higher temperatures will most likely destroy the gyroid morphology.

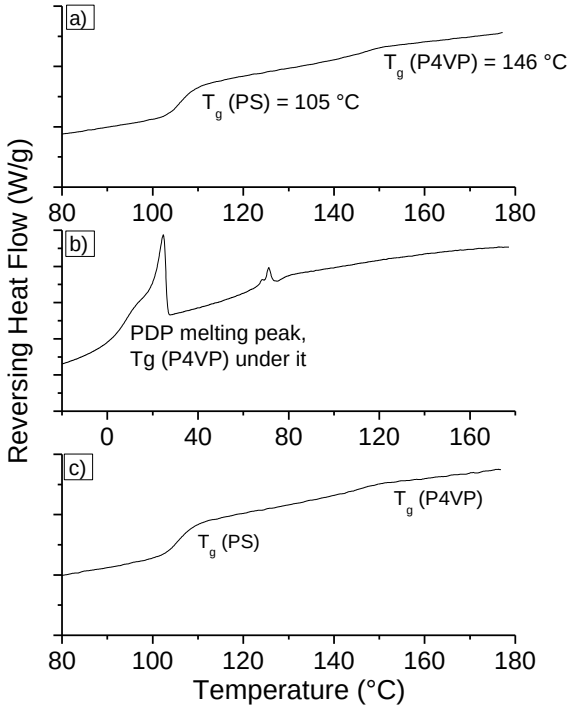

Figure 5.5. *DSC curves of a) PS-b-P4VP diblock copolymer, b) PS-b-P4VP(PDP)$_x$ supramolecular complex (the peak at ca. 70 °C is due to the order-disorder transition of the P4VP(PDP) domains, and the T_g of PS is decreased to ca. 76 °C due to the presence of a small amount of PDP in the PS phase), and c) PS-b-P4VP(PDP)$_x$ after washing with ethanol. The reversing heat flows are shown because the T_g positions are more pronounced in these curves.*

By the complete PDP removal, the matrix of the complexes is emptied and a double PS (core)–P4VP (corona) network is exposed. A formation of large defects in the structure, a presence of closed or disconnected pores or even a complete collapse of the network are some of the apparent possibilities which can consequently disqualify this system as a precursor to nanoporous metal foams. Therefore, the textural properties of the porous PS-*b*-P4VP(PDP)$_{1.0}$ film (S4VP-

45.1k-1 precursor and $f_{P4VP(PDP)}$ = 0.62 before the ethanol treatment) after the ethanol treatment were determined using the nitrogen adsorption–desorption isotherm. The nitrogen adsorption–desorption isotherm corresponds to the type IV isotherms according to the IUPAC classification (Figure 5.6). The initial part of the isotherm (at low relative pressure) is reversible, and it is attributed to a monolayer–multilayer adsorption of nitrogen onto the sample surface. At higher relative pressure, there is a hysteresis loop of the H1 type, which is associated with the capillary condensation in the mesopores and indicates cylindrical pore geometry and high degree of pore size uniformity. The shape of the adsoprtion isotherm at relative pressure near to the unity offers the possibility to determine the total pore volume, $V_{p,0.99}$, using the method given by Gurvitsch.[47, 48] From the adsorption branch of the nitrogen isotherm, the distribution of the pore volume according to their size is calculated. The calculation is based on the Kelvin equation that correlates the relative equilibrium pressure to the pore diameter (allowance for the thickness of the adsorbed layer is made, and a cylindrical shape of the pores is assumed). The derivative of the cumulative pore volume with respect to the pore diameter for the porous PS-*b*-P4VP(PDP)$_{1.0}$ film after the ethanol treatment is shown in Figure 5.7. The data obtained are summarized in Table 5.1. The textural properties of the porous film were also determined by mercury porosimetry (Figure 5.8 and Table 5.2). Excellent agreement between the nitrogen adsorption and mercury porosimetry results is found.

The data confirm the formation of a mesoporous structure with a very narrow pore size distribution. The average pore diameter of 40 nm is comparable to the size of the P4VP(PDP)$_{1.0}$ domain. The BET specific surface area is rather high and is determined to be 104 $m^2\ g^{-1}$. The expected porosity of the PS-*b*-P4VP(PDP)$_{1.0}$ film after the ethanol treatment is calculated to be 46 vol % on the basis of the amount of PDP originally present using the approximation of equal bulk densities. From $V_{p,0.99}$ and $V_{p,total}$ determined using the nitrogen adsorption–desorption isotherm, the porosity of the template was evaluated to be 44.3 and 41.7 vol %, respectively, well below the 50% v/v as required for a template for the production of metal nanofoams.

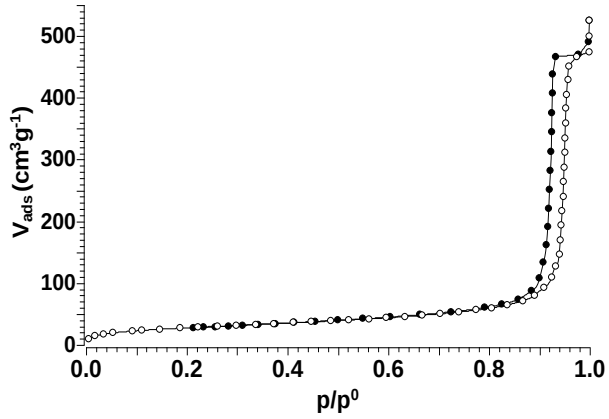

Figure 5.6. *Nitrogen adsorption–desorption isotherm of the porous PS-b-P4VP(PDP)$_{1.0}$ film (S4VP-45.1k-1 precursor and $f_{P4VP(PDP)}$ = 0.62 before the ethanol treatment) after the ethanol treatment.*

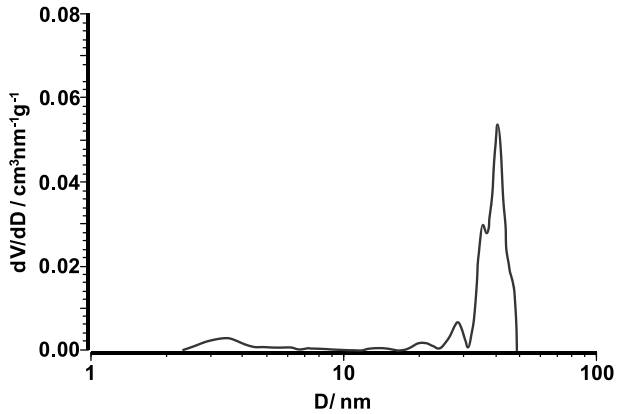

Figure 5.7. *Pore size distribution of the porous PS-b-P4VP(PDP)$_{1.0}$ film (S4VP-45.1k-1 precursor and $f_{P4VP(PDP)}$ = 0.62 before the ethanol treatment) after the ethanol treatment; the derivative of the cumulative pore volume curve vs. pore diameter.*

Table 5.1. *Textural properties of the porous PS-b-P4VP(PDP)$_{1.0}$ film (S4VP-45.1k-1 precursor and $f_{P4VP(PDP)}$ = 0.62 before the ethanol treatment) after the ethanol treatment obtained from the nitrogen adsorption–desorption isotherm.*

S_{BET}, $m^2\ g^{-1}$	$V_{p,0.99}$, $mm^3\ g^{-1}$	$V_{p,total}$[a], $mm^3\ g^{-1}$	D_{med}[a], nm	D_{max}[a], nm
104	795	715	39.8	40.8

[a]*Cumulative pore volume, $V_{p,total}$, median pore diameter, D_{med}, and maximum pore diameter, D_{max}, are determined using the Dollimore and Heal method.*

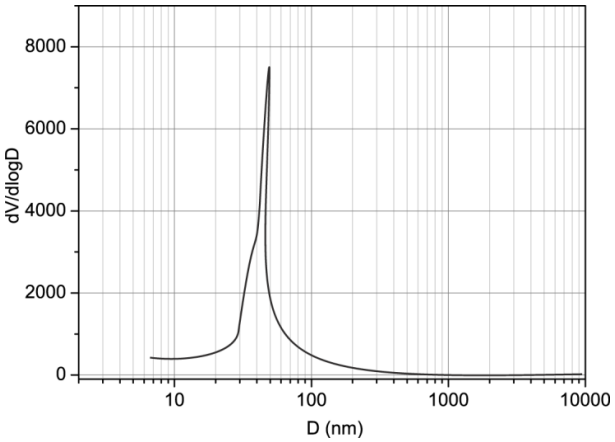

Figure 5.8. *The pore size distribution of the porous film PS-b-P4VP(PDP)$_{1.0}$ (S4VP-45.1k-1 precursor and $f_{P4VP(PDP)}$ = 0.62 before the ethanol treatment) after the ethanol treatment determined by mercury porosimetry.*

Table 5.2. *Textural properties of the porous films PS-b-P4VP(PDP)$_x$ film (S4VP-45.1k-1 precursor and $f_{P4VP(PDP)}$ = 0.62 before the ethanol treatment) after the ethanol treatment obtained from mercury porosimetry.*

S_{Hg}, $m^2\ g^{-1}$	V_p, $mm^3\ g^{-1}$	D, nm
112	775	50

5.3.3 Inserting nickel in the polymer template

Electroless plating is employed to insert nickel in the pores of the gyroid polymer template (Figure 5.1d). This technique offers the possibility to create uniform coatings over complicated surfaces or to insert metal in complex-shaped nanochannels.[53, 54] Another advantage over conventional electrochemical plating is that the surface of the template does not necessarily have to be conductive. The water-based plating reagents diffuse through the interconnected channels and influence sensitization and activation of their surface followed by nickel deposition onto the activated areas. The affinity between the aqueous plating solutions and the surface of the template is a very important factor for the successful nickel deposition.
In the pretreatment step, the catalyst Pd is deposited onto the surface of the gyroid network: PS core/P4VP corona. It directs selective nickel ion reduction at the activated surfaces. During the successive metal deposition, nickel fills the pores of the polymer template. Figure 5.9 shows the bright-field TEM images of ultrathin sections of the nickel-plated samples. The samples are not stained, and therefore, the contrast in the TEM images results from nickel deposited in the nanochannels. The observed TEM images are in good agreement with the TEM images of the supramolecular complexes: the dark nickel domains in Figure 5.9 correspond to the dark P4VP(PDP)$_x$ domains stained with iodine in Figure 5.2. Figure 5.9a represents an area located near the surface of the plated film, while the middle of the plated film is shown in Figure 5.9b. Both pictures confirm the homogenuous distribution of nickel throughout the film. The characteristic wagon-wheel pattern of the (111) gyroid projection is shown in Figure 5.10a and further confirms the preservation of the double gyroid morphology during the PDP removal and the electroless nickel plating. HR TEM micrographs (Figure 5.10b, c) show relatively large, interconnected Ni crystallites, and the EDX analysis (Figure 5.10d) reveal the chemical composition of the plated sample. As expected, prominent carbon and nickel peaks are observed, together with the oxygen peak that indicates the oxidation of the nickel nanofoam when stored in air.

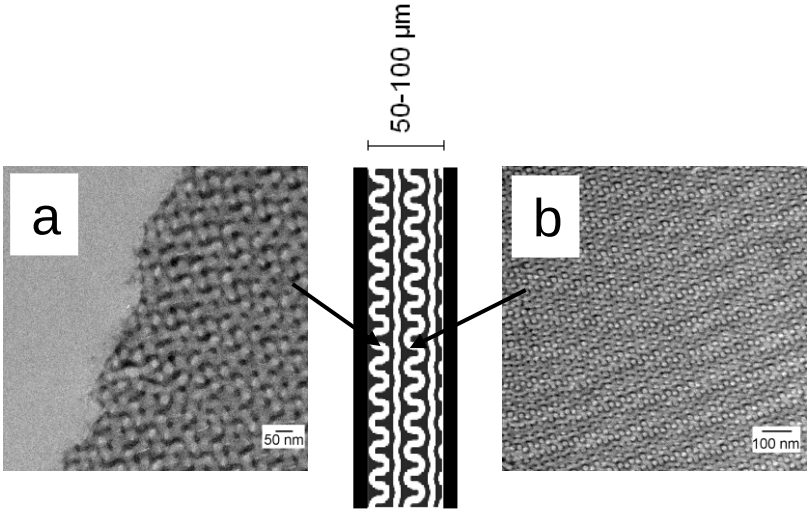

Figure 5.9. *Bright-field TEM images of the unstained ultrathin-sectioned nickel-plated gyroid polymer template. The nickel-plated domains appear dark. The starting supramolecular complex PS-b-P4VP(PDP)$_{1.5}$ is derived from S4VP-59.0k. A schematic representation of the nickel-plated film is shown, as well. a) Area located near the surface of the plated film; the epoxy resin used for embedding is visible in the left part of the image. b) Area located in the middle of the plated film.*

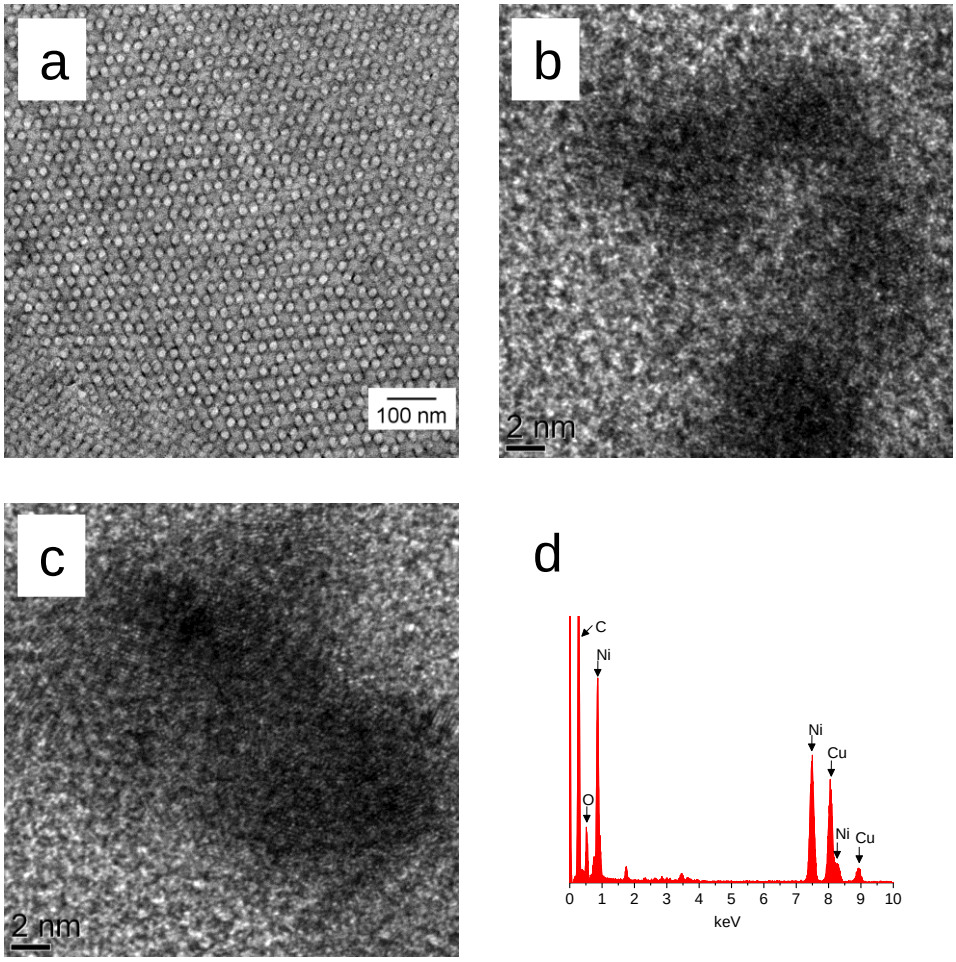

Figure 5.10. *(a) TEM image of the unstained nickel-plated gyroid polymer template derived from the PS-b-P4VP(PDP)$_{1.0}$ (S4VP-45.1k-1 precursor). The image represents the (111) gyroid projection. (b, c) HR TEM images showing relatively large and interconnected Ni crystallites. (d) EDX pattern of the nickel plated sample showing prominent carbon and nickel peaks, together with the oxygen peak that indicates the oxidation of the nickel nanofoam when stored in air. The copper peak originates from the grid used as a support. The nickel plated sample (b, c, d) is derived from the PS-b-P4VP(PDP)$_{0.8}$ complex (S4VP-53.5k-1 precursor).*

5.3.4 Exposure of the inverse gyroid nickel foam

Subsequently, the polymer template is decomposed by heating isothermally at 350 °C (Figure 5.1e), while leaving the nickel network intact. Thermogravimetric analyses of the porous PS-*b*-P4VP(PDP)$_x$ films following the PDP removal (Figure 5.11) suggest a minimal pyrolysis time of 30 min. The nickel replica remains stable after the thermal treatment and retains the inverse gyroid morphology imposed by the structure of the porous polymer template, as evidenced by SEM images (Figures 5.12 and 5.13). Longer pyrolysis time, up to 4 days, does not affect the stability of nickel nanofoam (Figures 5.12 and 5.13a). Figures 5.13a and 5.13b reveal the typical gyroid double-wave pattern. A micrometer-sized area of the gyroid ordering is displayed in Figures 5.12 and 5.13c.
The chemical composition of the sample before and after pyrolysis is analysed with energy-dispersive analysis of X-rays (EDX), and the result is shown in Figure 5.14. The dominant carbon peak in Figure 5.14a disappears after the thermal treatment of the sample (Figure 5.14b), which indicates the efficiency of the thermal treatment. In Figure 5.14b, the two prominent peaks correspond to nickel. An oxygen peak around 0.5 keV indicates the oxidation of the nickel nanofoam when stored in air.

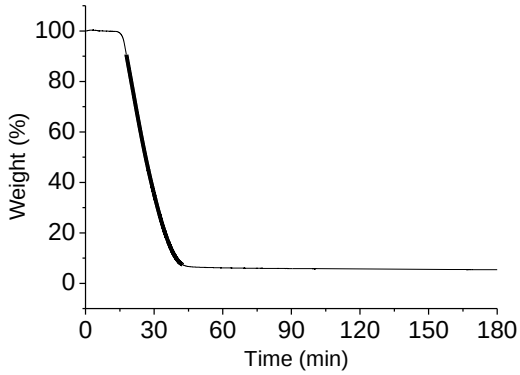

Figure 5.11. *TGA curve for the porous polymer template - PS-b-P4VP(PDP)x after the PDP removal. The sample is heated from 25 °C to 350 °C with a heating rate of 20 °C/min and then kept at 350 °C for 3h. The bold segment of the curve represents the continuous weight loss of the sample at 350 °C with only negligible residue (ca. 5 % of the initial weight).*

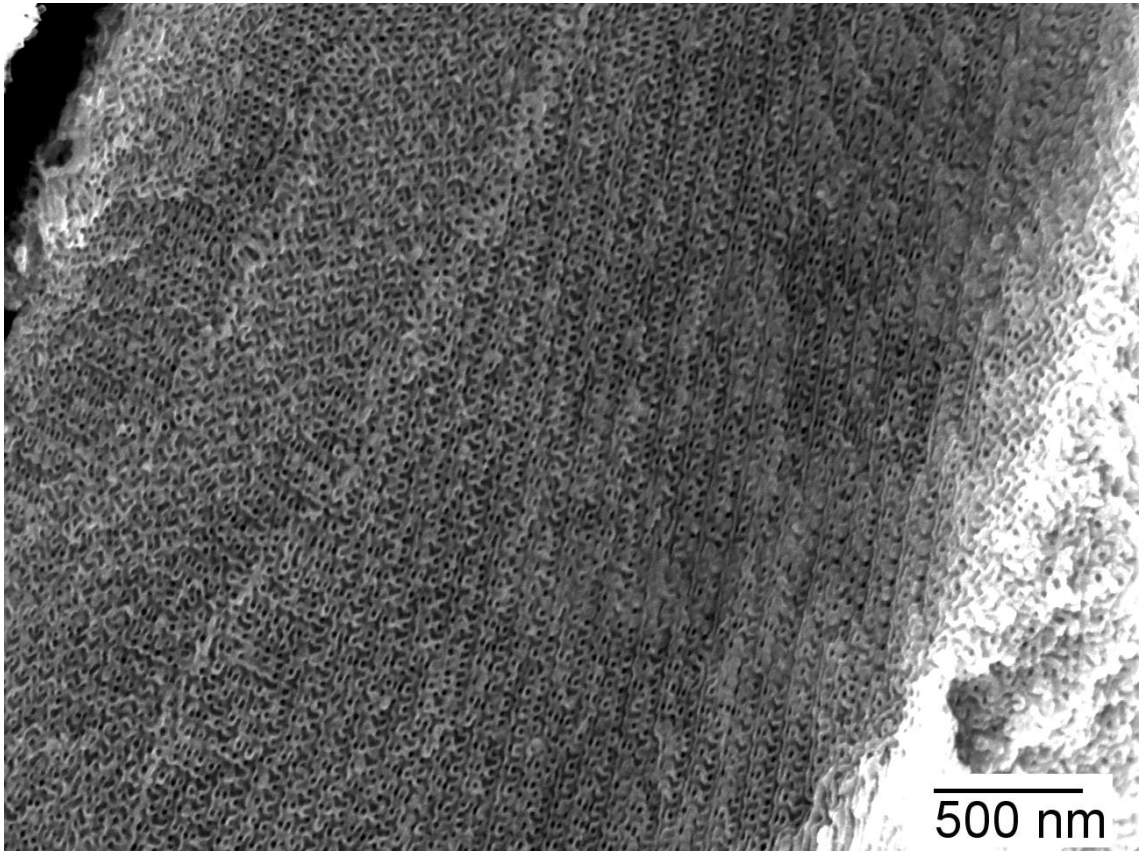

Figure 5.12. *SEM image of the inverse gyroid nickel replica obtained after the polymer template removal by pyrolysis during 4 days. The starting supramolecular complex PS-b-P4VP(PDP)$_x$ is derived from S4VP-59.0k precursor and has x = 1.5.*

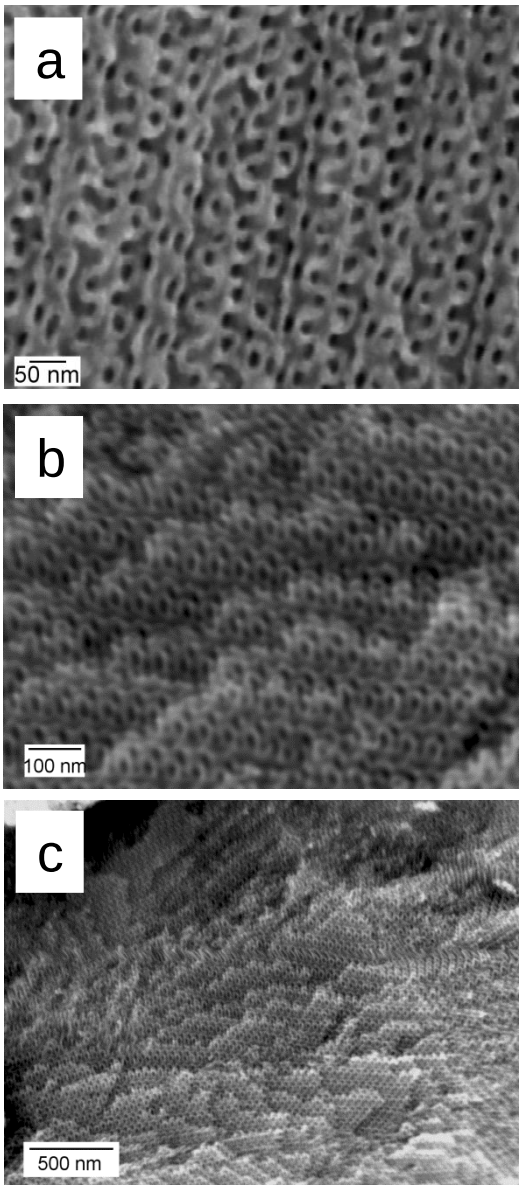

Figure 5.13. *SEM images of the inverse gyroid nickel replicas obtained after the polymer template removal by pyrolysis (pyrolysis time = a) 4 days, b) and c) 3 hours). A 3D network structure composed of the interconnected nickel struts is clearly visible. The starting supramolecular complexes PS-b-P4VP(PDP)$_x$ have the following characteristics: a) S4VP-59.0k precursor and x = 1.5, b) and c) S4VP-53.5k-1 precursor and x = 0.8.*

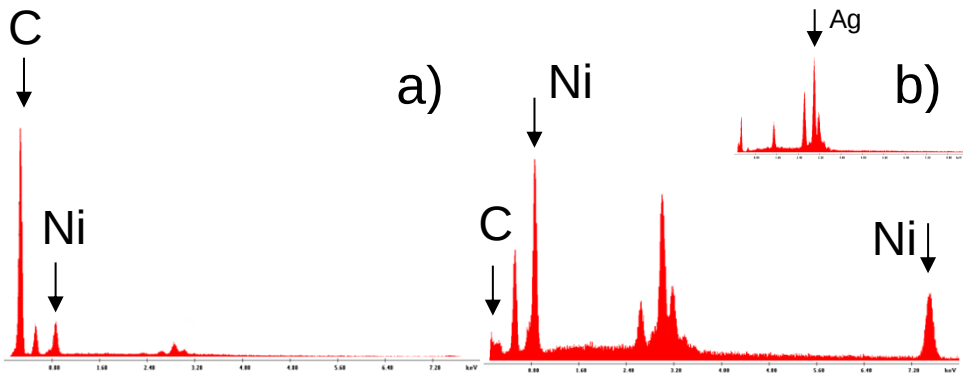

Figure 5.14. *EDX analysis of the nickel-plated sample before (a) and after the polymer template removal (b). The starting supramolecular complex is PS-b-P4VP(PDP)$_{1.5}$ derived from S4VP-59.0k. The peaks in the region of 2.40−4.00 keV originate from the silver paste that is used to attach the sample to the sample holder. EDX analysis of the silver paste is displayed in the inset of (b).*

5.4 Conclusion

Supramolecular PS-*b*-P4VP(PDP) complexes with a bicontinuous gyroid morphology were used as templates to produce metallic nickel nanofoams. The complete dissolution of PDP from the complex with the major P4VP(PDP) component forming the matrix results in an open network structure with struts consisting of a PS core and a P4VP corona. The high specific surface area and the narrow pore size distribution of the structure formed are evidenced by nitrogen adsorption and mercury porosimetry. The open nature of the pores allows for electroless deposition of metal. During the processing, the symmetry and the size of the nanopattern are conserved. The subsequent removal of the polymer template by pyrolysis leads to the formation of an inverse gyroid nickel nanofoam with porosity exceeding 50% v/v. The use of polymer templates with different compositions and sizes of the domains enabled us to further tune the porosity characteristics.

5.5 Appendix

5.5.1 Properties of the inverse gyroid nickel foam

The investigation of the inverse gyroid nickel foam properties is in the scope of the PhD thesis of my collaborator Sergey Punzhin, a PhD student from Materials Science Group, Zernike Institute for Advanced Materials, University of Groningen, who provided the following results and explanations.

The development of ordered nanoporous metals allows the question to be asked whether this ordering has a significant impact on the material's properties compared to those of a disordered one, fabricated, for example, through the common dealloying process. Addressing this question is vital for the formation of a fundamental understanding of the applicability of such ordered nanofoams.

To address this question, we have implemented a manufacturing process that permits us to make to a good degree of precision features down to several hundred nanometres in size. The porous nanopillars were cut from nanoporous Ni. Non-tapering of the nanopillars sides was achieved by using a custom FIB milling technique.[55] Common milling techniques introduce tapering, during which the cross-sectional area across the length gradually becomes thicker towards its base. As we are interested in the mechanical behavior of the pillar across its entire length, we wish to ensure a uniform pillar's diameter. Our procedure ensures such a taper-free pillar's geometry. A set of fully taper-free nanoporous Ni pillars with diameter 500 nm (Figure 5.15) was fabricated by means of a dual beam FIB/SEM microscope (Lyra, Tescan). The aspect ratio of the pillars was initially chosen to be in the range of 2-3. We use this initial aspect ratio for simplicity: it is easy to ion mill the nanoporous Ni while retaining reasonable structural stability and mechanical properties for handling.

The final shape and orientation of the fabricated ordered Ni nanofoam pillars are conducive to a variety of mechanical experimental techniques, amongst them the popular picoindentation process performed in-situ inside a TEM by the means of a specialized Hysitron indenter tip and holder (Figure 5.16). This setup has a high accuracy and degree of control in the indentation direction, and yields accurate stress-strain information.

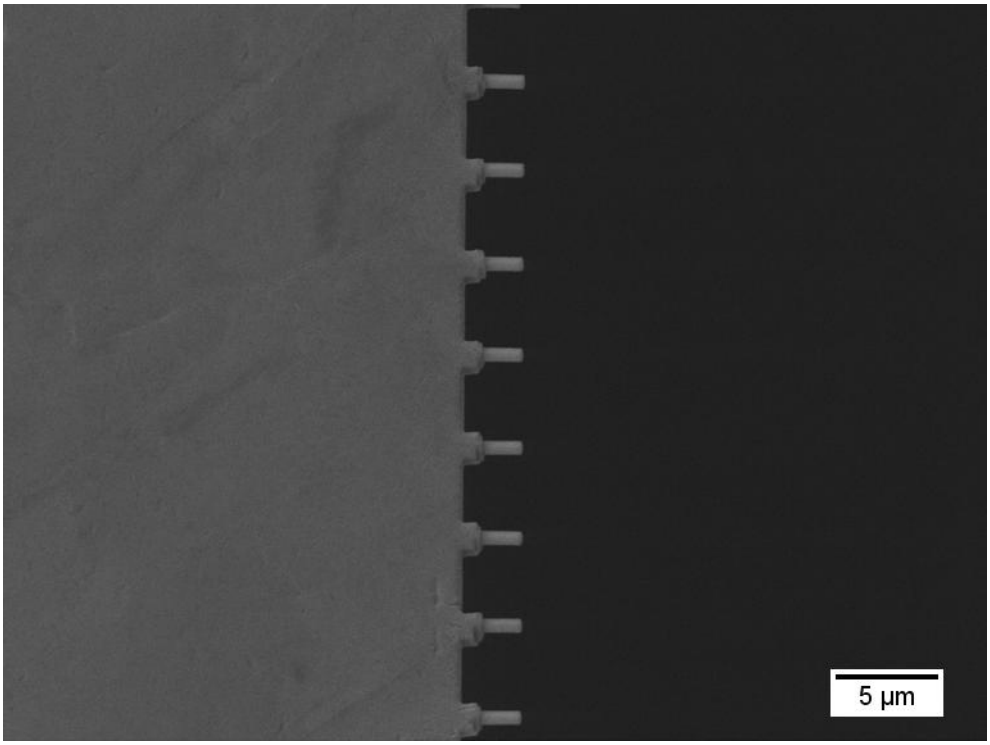

Figure 5.15. *Taper-free nanoporous Ni pillars with 500 nm diameter.*

However, a clear issue with this method is the necessity of perfect alignment of the indenter tip and the target pillar. Due to the particular construction of the picoindenter apparatus, the best results are achieved when the working area is situated exactly in the center of the holder. As the working area moves towards the sides, the indentation pressure acquires more and more of a horizontal component. As a result, a pillar in the working area no longer experiences true compression but, rather, an unpredictable bending effect.

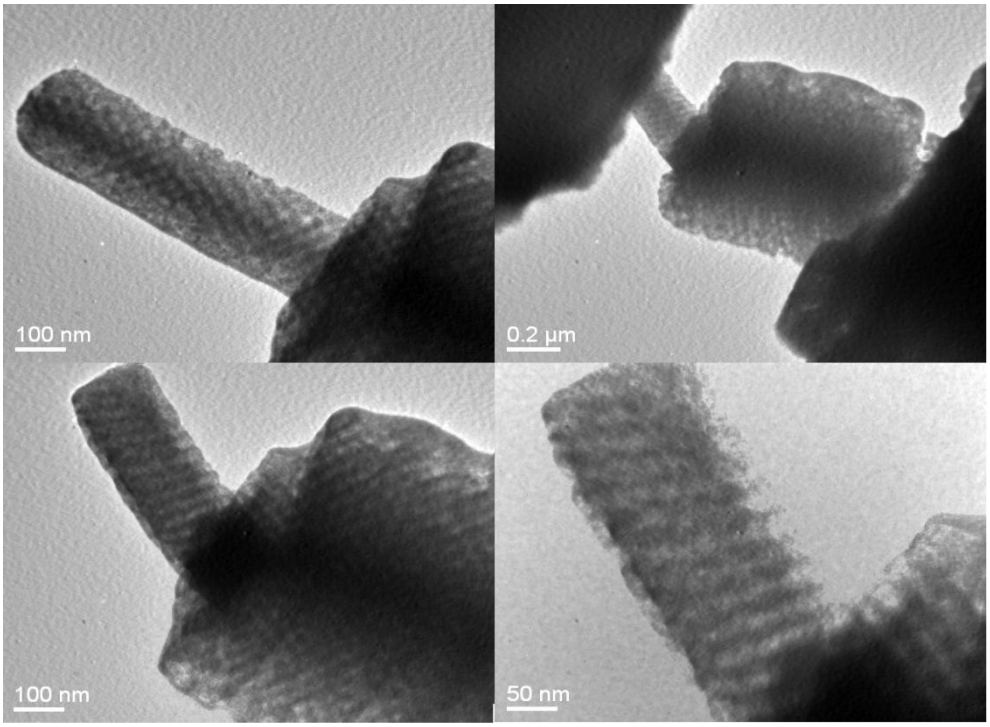

Figure 5.16. *Nanoporous Ni nanopillars before (upper left), during (upper right) and after indentation (lower left and right).*

It emerges that a method that would allow for the in-situ induction and observation of deformation behavior of submicron size nanoporous systems that does not require the precise sample arrangement of picoindentation is desirable. Ion-Beam-Induced Bending (IIB) has recently been garnering a lot of attention for its ability to finely shape nanostructured materials; in particular, studies have demonstrated the use of a Ga ion beam to bend carbon nanotubes, nanopillars and Ag cantilevers into a variety of well-controlled shapes.[56-58] IIB can be implemented as a valuable experimental method that does not require a conventional mechanical contact during deformation, such as with standard mechanical testing methods (e.g. nanoindentation and tensile testing). In IIB, the ion beam itself causes the deformation and, as such, IIB can operate on the far smaller scale that we require for our own experiments.

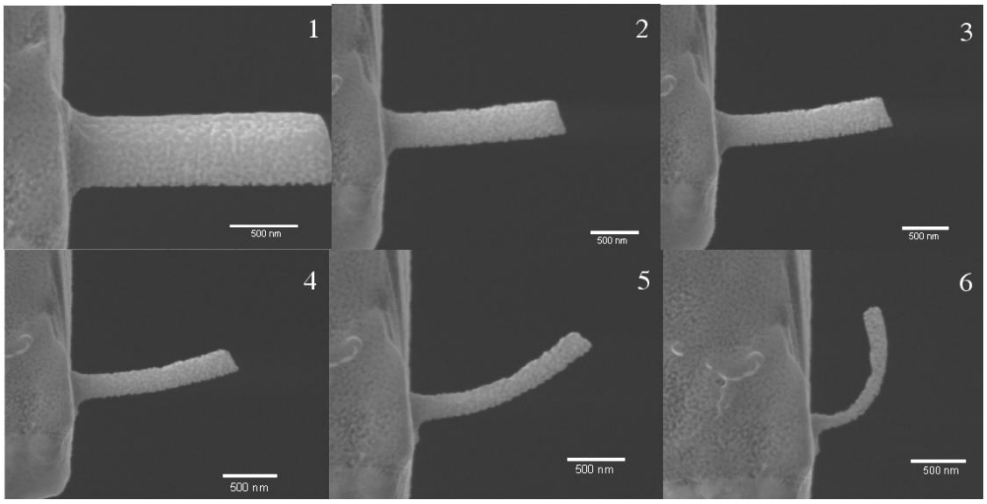

Figure 5.17. *Ion-Beam-Induced Bending (IIB) of disordered nanoporous Au.*

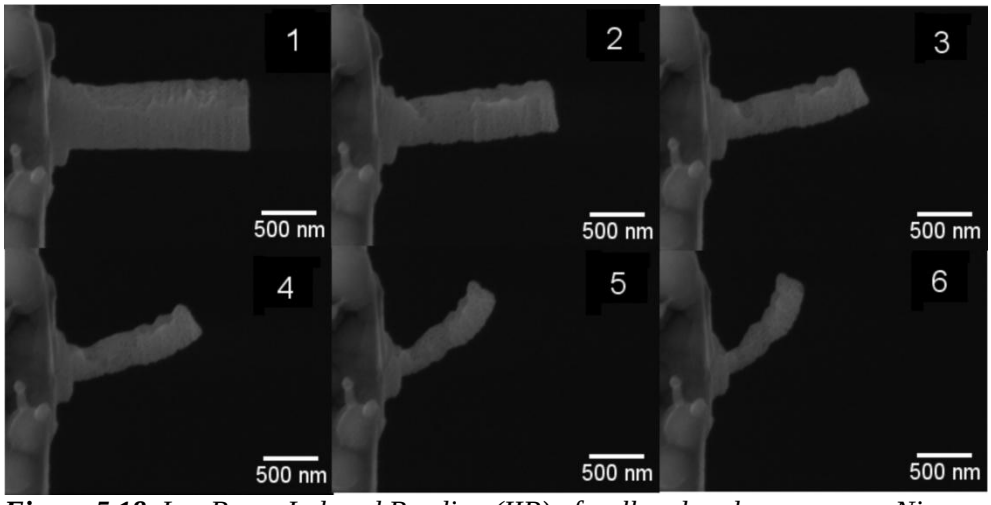

Figure 5.18. *Ion-Beam-Induced Bending (IIB) of well-ordered nanoporous Ni.*

Pillar deformation was induced using the same equipment as pillar fabrication. Each pillar was aligned perpendicular to the beam to fully expose one of its faces. This leaves the opposing face in the ion beam's shadow. Variation was possible in probe current and size of exposed area. Ion beam energy was maintained constant at 30 keV, and beam currents of 1, 10, 40 and 150 pA were selected for the experiment. We note that the presented values are software-controlled current

presets, and may vary from the actual beam current emitted by the ion beam source. In every case, true ion beam current values are used. Exposure times varied between 1 and 300 seconds, depending on ion beam current used.

We can see that ordered structures are far more susceptible to localization effects - where disordered pillars bend uniformly (Figure 5.17), ordered ones tend to bend more strongly at single points (Figure 5.18). In addition, due to the anisotropic nature of a gyroidal cross-section, the deformation behaviour of an ordered nanofoam pillar will vary depending on grain orientation and incidence angle of the ion beam.

IIB is currently a novel method, and its use in determining the physical properties of ordered and disordered metallic nanofoams is still in progress.

5.6 References

1. Tappan BC, Steiner SA, Luther EP. Angew Chem Int Ed 2010;49(27):4544-4565.
2. Cammarata RC. Prog in Surf Sci 1994;46(1):1-38.
3. Ibach H. Surf Sci Rep 1997;29:195-263.
4. Weissmüller J, Viswanath RN, Kramer D, Zimmer P, Würschum R, Gleiter H. Science 2003;300(5617):312-315.
5. Kramer D, Viswanath RN, Weissmüller J. Nano Letters 2004;4(5):793-796.
6. Baughman RH. Science 2003;300(5617):268-269.
7. Erlebacher J, Aziz MJ, Karma A, Dimitrov N, Sieradzki K. Nature 2001;410:450-453.
8. Detsi E, van de Schootbrugge M, Punzhin S, Onck PR, De Hosson JTM. Scripta Mater 2011;64(4):319-322.
9. Nyce GW, Hayes JR, Hamza AV, Satcher JH. Chem Mater 2007;19(3):344-346.
10. Gacoin T, Lahlil K, Larregaray P, Boilot JP. J Phys Chem B 2001;105(42):10228-10235.
11. Leventis N, Chandrasekaran N, Sotiriou-Leventis C, Mumtaz A. J Mater Chem 2009;19(1):63-65.
12. Leventis N, Chandrasekaran N, Sadekar AG, Sotiriou-Leventis C, Lu H. J Am Chem Soc 2009;131(13):4576-4577.
13. Tappan BC, Huynh MH, Hiskey MA, Chavez DE, Luther EP, Mang JT, et al. J Am Chem Soc 2006;128(20):6589-6594.
14. Ashby MF, Evans AG, Fleck NA, Gibson LJ, Hutchinson JW, Wadley HG. Metal Foams: a Design Guide. Oxford, UK: Butterworth-Heinemann, 2000.
15. Tekoglu C. Size Effects in Cellular Solids. University of Groningen, 2007.
16. Amsterdam E. Structural Performance and Failure Analysis of Aluminium Foams. University of Groningen, 2008.
17. Bates FS, Fredrickson GH. Annu Rev Phys Chem 1990;41:525-527.
18. Hamley IW. The Physics of Block Copolymers. Oxford: Oxford University Press, 1998.

19. Abetz V, Simon P. Phase Behaviour and Morphologies of Block Copolymers. Advances in Polymer Science: Springer Berlin / Heidelberg, 2005.
20. Hillmyer MA. Adv Polym Sci 2005;190:137-181.
21. Mäki-Ontto R, de Moel K, de Odorico W, Ruokolainen J, Stamm M, ten Brinke G, et al. Adv Mater 2001;13:117-121.
22. Ikkala O, ten Brinke G. Science 2002;295:2407-2409.
23. Nandan B, Vyas MK, Böhme M, Stamm M. Macromolecules 2010;43(5):2463-2473.
24. Crossland EJW, Kamperman M, Nedelcu M, Ducati C, Wiesner U, Smilgies DM, et al. Nano Letters 2008;9(8):2807-2812.
25. Thurn-Albrecht T, Schotter J, Kästle GA, Emley N, Shibauchi T, Krusin-Elbaum L, et al. Science 2000;290(5499):2126-2129.
26. Sidorenko A, Tokarev I, Minko S, Stamm M. J Am Chem Soc 2003;125(40):12211-12216.
27. Jeong U, Kim HC, Rodriguez RL, Tsai IY, Stafford CM, Kim JK, et al. Adv Mater 2002;14(4):274-276.
28. Mao H, Hillmyer MA. Soft Matter 2006;2(1):57-59.
29. Hashimoto T, Tsutsumi K, Funaki Y. Langmuir 1997;13(26):6869-6872.
30. Hashimoto T, Nishikawa Y, Tsutsumi K. Macromolecules 2007;40(4):1066-1072.
31. Urade VN, Wei TC, Tate MP, Kowalski JD, Hillhouse HW. Chem Mater 2007;19:768-777.
32. Warren SC, Messina LC, Slaughter LS, Kamperman M, Zhou Q, Gruner SM, et al. Science 2008;320(5884):1748-1752.
33. Crossland EJW, Ludwigs S, Hillmyer MA, Steiner U. Soft Matter 2010;6(3):670-676.
34. Hsueh H-Y, Chen H-Y, She M-S, Chen C-K, Ho R-M, Gwo S, et al. Nano Letters 2010;10(12):4994-5000.
35. Hsueh HY, Huang YC, Ho RM, Lai CH, Makida T, Hasegawa H. Adv Mater 2011;23(27):3041-3046.
36. Hsueh H-Y, Ho R-M. Langmuir 2012;28(22):8518-8529.
37. Vignolini S, Yufa NA, Cunha PS, Guldin S, Rushkin I, Stefik M, et al. Adv Mater 2012;24(10):OP23-OP27.
38. van Ekenstein AGOR, Meyboom R, ten Brinke G, Ikkala O. Macromolecules 2000;33:3752-3756.

39. Zha W, Han CD, Lee DH, Han SH, Kim JK, Kang JH, et al. Macromolecules 2007;40(6):2109-2119.
40. Matsen MW, Schick M. Phys Rev Lett 1994;72(16):2660-2663.
41. Polushkin E, van Ekenstein AGOR, Knaapila M, Ruokolainen J, Torkkeli M, Serimaa R, et al. Macromolecules 2001;34(14):4917-4922.
42. Finnefrock AC, Ulrich R, Toombes GES, Gruner SM, Wiesner U. J Am Chem Soc 2003;125(43):13084-13093.
43. Valkama S, Ruotsalainen T, Nykänen A, Laiho A, Kosonen H, ten Brinke G, et al. Macromolecules 2006;39(26):9327-9336.
44. Kobayashi Y, Tadaki Y, Nagao D, Konno M. J Phys: Conf Ser 2007;61:582-586.
45. Mallory GO, Hajdu JB. Electroless Plating: Fundamentals and Applications: American Electroplaters and Surface Finishers Society, 1992.
46. Riedel W. Electroless Nickel Plating. Finishing Publications: Metals Park, 1991.
47. Gregg SH, Sing KSW. Adsorption, Surface Area and Porosity. New York: Academic Press, 1967.
48. Rouquerol F, Rouquerol J, Sing KSW. Adsorption by Powders and Porous Solids. London: Academic Press, 1999.
49. Sing KSW, Everettt DH, Haul RAW, Moscou L, Pierotti RA, Rouquerol J, et al. Pure Appl Chem 1985;57(4):603-619.
50. Dollimore D, Heal GR. J Appl Chem 1964;14(3):109-114.
51. Webb PA, Orr C. Analytical Methods in Fine Particle Technology Norcross, GA: Micrometrics Instrument Corporation, 1997.
52. Leofanti G, Padovan M, Tozzola G, Venturelli B. Catal Today 1998;41:207-219.
53. Lee I, Hammond PT, Rubner MF. Chem Mater 2003;15(24):4583-4589.
54. Boontongkong Y, Cohen RE, Rubner MF. Chem Mater 2000;12(6):1628-1633.
55. Kuzmin OV, Pei YT, Chen CQ, De Hosson JTM. Acta Mater 2012;60(3):889-898.
56. Park BC, Jung KY, Song WY, O Bh, Ahn SJ. Adv Mater 2006;18(1):95-98.
57. Tripathi SK, Shukla N, Dhamodaran S, Kulkarni VN. Nanotechnology 2008;19(20):205302.

58. Rajput NS, Banerjee A, Verma HC. Nanotechnology 2011;22(48):485302.

Publications and Conferences

1. List of publications

1. ten Brinke, G.; Gobius du Sart, G.; **Vukovic, I.**; Polushkin, E.; Loos, K. Supramolecular Triblock Copolymer Complexes. *Contemporary Science of Polymeric Materials* **2010**, book chapter.

2. Gobius du Sart, G.; **Vukovic, I.**; Alberda van Ekenstein, G.O.R.; Polushkin, E.; Loos, K.; ten Brinke, G. Self-Assembly of Supramolecular Triblock Copolymer Complexes. *Macromolecules* **2010**, *43* (6), 2970-2980.

3. Gobius du Sart, G.; **Vukovic, I.**; Vuković, Z.; Polushkin, E.; Hiekkataipale, P.; Ruokolainen, J.; Loos, K.; ten Brinke, G. Nanoporous Network Channels from Self-Assembled Triblock Copolymer Supramolecules. *Macromol. Rapid Commun.* **2011**, *32*, 366-370.

4. ten Brinke, G.; Loos, K.; **Vukovic, I.**; Gobius du Sart, G. Hierarchical Self-Assembly of Two-Length-Scale Multiblock Copolymers. *J. Phys.: Condens. Matter.* **2011**, *23*, 284110.

5. **Vukovic, I.**; Punzhin, S.; Vuković, Z.; Onck, P.; de Hosson, J.T.M.; ten Brinke, G.; Loos, K. Supramolecular Route to Well-Ordered Metal Nanofoams. *ACS Nano* **2011**, *5* (8), 6339-6348.

6. Detsi, E.; De Jong, E.; Zinchenko, A.; Vuković, Z.; **Vukovic, I.**; Punzhin, S.; Loos, K.; ten Brinke, G.; De Raedt, H.A.; Onck, P.; De Hosson, J.T.M. On the Specific Surface Area of Nanoporous Materials. *Acta Materialia* **2011**, *59* (20), 7488-7497.

7. **Vukovic, I.**; Voortman, T.P.; Hermida Merino, D.; Portale, G.; Hiekkataipale, P.; Ruokolainen, J.; ten Brinke, G.; Loos, K. Double Gyroid Network Morphology in Supramolecular Diblock Copolymer Complexes. *Macromolecules* **2012**, *45* (8), 3503-3512.

8. Vukicevic, R.; **Vukovic, I.**; Stoyanov, H.; Korwitz, A.; Pospiech, D.; Kofod, G.; Loos, K.; ten Brinke, G.; Beuermann, S. Poly(vinylidene fluoride)–Functionalized Single–Walled Carbon Nanotubes for the Preparation of Composites with Improved Conductivity. *Polym. Chem.* **2012**, *3*, 2261-2265.

9. **Vukovic, I.**; ten Brinke, G.; Loos, K. Hexagonally Perforated Layer Morphology in PS-*b*-P4VP(PDP) Supramolecules. *Macromolecules* **2012**, *45* (23), 9409-9418.

10. Zunic, M.; Milutinovic–Nikolic, A.; Nastasovic, A.; Vukovic, Z.; Loncarevic, D.; **Vukovic, I.**; Loos, K.; ten Brinke, G.; Jovanovic D. Textural Properties of Poly(glycidyl methacrylate): Acid-Modified Bentonite Nanocomposites. *Polym. Bull.* **2013**, DOI: 10.1007/s00289-013-0924-1

11. **Vukovic, I.**; ten Brinke, G.; Loos, K. Block Copolymer Template-Directed Synthesis of Well-Ordered Metallic Nanostructures. *Polymer* **2013,** DOI: 10.1016/j.polymer.2013.03.013

12. **Vukovic, I.**; Punzhin, S.; Vukovic, Z.; de Hosson, J.T.M.; ten Brinke, G.; Loos, K. Gyroid Nickel Nanostructures from Diblock Copolymer Supramolecules, *submitted to Journal of Visualized Experiments*

13. **Vukovic, I**; Friedrich, H.; Hermida Merino, D.; Portale, G.; ten Brinke, G.; Loos, K. Shear-Induced Orientatation of Gyroid PS-*b*-P4VP(PDP) Supramolecules, *manuscript in preparation*

2. Conferences

Date and place	**Type**	**Contribution**
29-31 March, 2009 Vlieland The Netherlands	Bi-annual meeting of the Zernike Institute for Advance Materials	Poster presentation
15-16 February, 2010 Veldhoven The Netherlands	Dutch Polymer Days	Poster presentation
6-10 March, 2010 Strasbourg France	International Conference on Multifunctional, Hybrid and Nanomaterials	Audience
14-15 March, 2011 Veldhoven The Netherlands	Dutch Polymer Days	Oral & poster presentation
15-17 May, 2011 Vlieland The Netherlands	Bi-annual meeting of the Zernike Institute for Advance Materials	Oral & poster presentation
22 June, 2011 Amsterdam The Netherlands	Synchrotron and Neutron Workshop	Poster presentation
11-13 September, 2011 Bayreuth Germany	12th International Symposium on Polymeric Materials	Oral presentation
18 November, 2011 Belgrade Serbia	Serbian Chemical Society	Oral presentation, invited lecture
28-30 November, 2011 Maarssen The Netherlands	CHAINS2011	Oral & poster presentation

23-25 February, 2012 Freiburg Germany	Makromolekulares Kolloquium	Poster presentation
12-13 March, 2012 Lunteren The Netherlands	Dutch Polymer Days	Oral & poster presentation
11-13 June, 2012 Kerkrade The Netherlands	International Symposium on Polymer Analysis and Characterization	Oral presentation
24-28 September, 2012 Sant Feliu de Guixols Spain	Precision Polymer Materials Summer School	Poster presentation
7 March, 2013 Belgrade Serbia	Sebrian Chemical Society	Oral presentation, invited lecture
18-19 March, 2013 Lunteren The Netherlands	Dutch Polymer Days	Oral & poster presentation, plenary talk

Summary

The development of novel functional materials fosters the advances in medicine, technology, energy supply, and industry in general. Nowadays, an extensive attention is drawn to nanomaterials with at least one dimension in the nanoscale range. For example, nanoporous metals have appeared recently and, due to their unique properties, have the potential to outperform the existing materials in a number of applications, such as: hydrogen storage materials, actuators, novel 3D structured batteries, substitutes for platinum group catalysts, *etc*. Common approaches for the preparation of metallic nanostructures render materials with highly disordered architecture which might have an adverse effect on their mechanical properties.

Block copolymers can microphase separate and self-assemble into ordered nanostructures. The idea to apply them as templates for the preparation of well-ordered metal nanofoams is the focus of this thesis. For that purpose, we use block copolymers with poly(4-vinyl pyridine) block (P4VP) that can complex with amphiphilic pentadecylphenol molecules (PDP) through hydrogen bonding. From obtained self-assembled supramolecules, PDP can be removed by dissolution in ethanol rendering ordered nanoporous polymer structures. These can be directly used as, for instance, membranes, or can be backfilled with an inorganic material – *e.g.*, metal. The latter results in polymer/metal nanohybrids from which polymer can be removed leaving behind well-ordered metallic nanostructures.

Chapter 1 describes properties and practical applications of metal nanofoams and gives an overview of the existing approaches for their preparation.

In chapter 2, supramolecular complexes based on triblock copolymer poly(*tert*-butoxystyrene)-*block*-polystyrene-*block*-poly(4-vinylpyridine) (P_tBOS-*b*-PS-*b*-P4VP) and amphiphilic PDP are evaluated as precursors to well-ordered metal nanofoams. These complexes are found to self-assemble into the core-shell double gyroid morphology (GYR) in a relatively broad composition range. P_tBOS forms

the matrix and the gyroid network in composed out of P4VP(PDP) core and PS corona. Ethanol treatment results in the complete removal of PDP and the formation of nanoporous gyroid structure with interconnected pores of 12 nm average diameter. High- and low-temperature electroless plating procedure is used to introduce metal (nickel) in the obtained nanochannels. Nickel is deposited only in the pores located a couple of micrometers away from the surface and the middle of the sample remains empty.

Therefore, we have to search for alternative block copolymer-based templates that would allow for uniform metal deposition. In the remaining chapters, our attention is drawn to supramolecular complexes based on diblock copolymer polystyrene-*block*-poly(4-vinylpyridine) (PS-*b*-P4VP) and amphiphilic PDP. An extensive study of the phase behavior of PS-*b*-P4VP(PDP) complexes in which P4VP(PDP) represents a majority block is given in chapter 3. A number of samples are found to adopt the double gyroid morphology with various unit cell sizes and relative PDP contents. Additionally, samples with biphasic morphologies – lamellae (LAM) together with gyroids or cylinders (CYL) together with gyriods are observed. A 3D structure of gyroid samples is resolved by electron tomography indicating that samples are ordered over large areas/volumes. Furthermore, using large amplitude oscillatory shear, the representative gyroid sample can be oriented promptly as evidenced by SAXS.

The phase behavior of PS-*b*-P4VP(PDP) complexes in which P4VP(PDP) represents a minority block is described in chapter 4. Instead of a gyroid phase between the lamellar and cylindrical region in the phase diagram, a hexagonally perforated layer (HPL) structure exists as an equilibrium phase in a relatively broad composition range. This comes as a surprise mainly because the HPL is known to be a metastable phase in neat block copolymers. This unique phase behavior is influenced by the presence of PDP "side chains" in the minority P4VP block. Morphologies with curved interface and the minority block (P4VP(PDP)) located on the concave side (GYR and CYL) become unfavorable, while morphologies with straight or curved interfaces and the minority block (P4VP(PDP)) located on the convex side become favorable (LAM and HPL).

Gyriod complexes with various sizes described in chapter 3 are evaluated as precursors to well-ordered metal nanofoams in chapter 5. PDP as a part of the gyroid P4VP(PDP) matrix can be completely removed in ethanol resulting in a porous polymer network with porosity lower than 50 vol%. Via electroless plating technique nickel can be distributed throughout the whole sample thickness.

Relatively large, interconnected nickel crystallites present in the pores of the template are visualized by HR TEM. The remaining polymer is then removed by pyrolysis. The exposed inverse gyroid nickel nanofoam remains ordered over large areas. Its physical properties are examined via picoindentation and ion beam induced bending in the Material Science group of the University of Groningen. The actuating properties of the nanofoam will be studied in the near future. The catalytic properties of the inverse gyroid nickel nanofoam are evaluated at Center for Heterogeneous Catalysis and Sustainable Chemistry at Van ‘t Hoff Institute for Molecular Sciences in Amsterdam. The use of porous gyroid polymer networks as membranes in batteries is examined at the University of Münster, Germany.

Samenvatting

De fabricatie van nieuwe functionele materialen bevordert de ontwikkeling van medicijnen, technologie, energievoorziening en de industrie in het algemeen. Tegenwoordig ligt de aandacht vooral op nanotechnologie waarbij in de materialen ten minste één karakteristieke dimensie op nanoschaal aanwezig is. Nanoporeuze materialen zijn hiervan een goed voorbeeld en hebben, gezien hun unieke eigenschappen, de potentie om bestaande materialen te overtreffen als toepassing in waterstofopslag, actuatoren, nieuwe 3D-gestructureerde batterijen, vervangers voor platinumgroep katalysatoren, *etc.*

Veelgebruikte technieken voor het maken van metallische nanostructuren leveren over het algemeen materialen op met een ongeordende architectuur, wat een nadelig effect kan hebben op de mechanische eigenschappen. De spontane microfasescheiding van blokcopolymeren kan leiden tot geordende nanostructuren. De nadruk in dit proefschrift ligt op het gebruik van deze structuren als een soort mal (op nanoschaal) voor het maken van goedgeordende metallische nanoschuimen. Daarom gebruiken we blokcopolymeren met een poly(4-vinylpyridine) blok (P4VP), dat kan complexeren met amfifiele pentadecylfenol moleculen (PDP) via waterstofbindingen. PDP kan worden verwijderd uit de spontaan verkregen supramoleculen door het op te lossen in ethanol, met geordende nanoporeuze polymeerstructuren als gevolg. Deze structuren vinden toepassing in bijvoorbeeld membranen, of kunnen worden gevuld met anorganisch materiaal, zoals metaal. Dat laatste resulteert in een polymeer/metaal nanohybride. Door de verwijdering van het polymeer blijft uiteindelijk een goedgeordende metallische nanostructuur over.

Hoofdstuk 1 beschrijft de eigenschappen en praktische toepassing van metallische nanoschuimen en geeft een overzicht van de bestaande methodes om deze te fabriceren.

In hoofdstuk 2 worden supramoleculaire complexen, gebaseerd op poly(*tert*-butoxystyreen)-*blok*-polystyreen-*blok*-poly(4-vinylpyridine) (P_tBOS-*b*-PS-*b*-P4VP) triblokcopolymeren en PDP amfifielen, onderzocht als voorlopers voor goedgeordende metallische nanoschuimen. Deze complexen blijken spontaan een kern-corona dubbele gyroïd (GYR) morphologie te vormen voor een groot aantal verschillende composities. P_tBOS vormt de matrix, terwijl het gyroïd netwerk bestaat uit een kern van P4VP(PDP) en een corona van PS. Wassen met ethanol zorgt voor de complete verwijdering van PDP en resulteert in de vorming van een nanoporeuze gyroïd structuur bestaande uit poriën (door de hele structuur met elkaar verbonden) met een gemiddelde diameter van 12 nm. Metaal (nikkel) wordt in de verkregen nanokanalen geplaatst met behulp van stroomloos plateren op zowel hoge als lage temperatuur. Nikkel is echter alleen terug te vinden in de poriën binnen enkele micrometers van het oppervlak, terwijl het midden van de poreuze film ongevuld blijft.
Daarom is er gezocht naar alternatieve blokcopolymeer-gebaseerde structuren, die wel compleet kunnen worden gevuld met metaal. In de overgebleven hoofdstukken zal de aandacht uitgaan naar supramoleculaire complexen gebaseerd op polystyreen-*blok*-poly(4-vinylpyridine) (PS-*b*-P4VP) diblokcopolymeren en PDP amfifielen. Een uitgebreide studie aangaande het fasegedrag van PS-*b*-P4VP(PDP) complexen waarin P4VP(PDP) het meerderheidsblok (blok met de grootste fractie) is, wordt beschreven in hoofdstuk 3. Een aantal films laat de dubbele gyroïd morfologie zien met een variërende grootte van de eenheidscel, gerelateerd aan de hoeveelheid toegevoegd PDP. Daarnaast worden ook films met bifasische morfologiën – lamellen (LAM) samen met gyroïden of cilinders (CYL) samen met gyroïden – waargenomen. De 3D structuur van de gyroïd morfologie wordt bewezen met behulp van elektronen tomografie. Het resultaat laat zien dat de nanostructuur over een groot gebied geordend is. Bovendien kan de gyroïd structuur onmiddellijk worden georiënteerd met behulp van oscillerende afschuiving met grote amplitude, zoals wordt bewezen met SAXS experimenten.
Het fasegedrag van PS-*b*-P4VP(PDP) complexen waarin P4VP(PDP) het minderheidsblok (blok met de kleinste fractie) is, wordt beschreven in hoofdstuk 4. Dit maal wordt, in plaats van de verwachte gyroïd fase, de hexagonaal geperforeerde laag (HPL) structuur gevonden als de evenwichtstoestand voor een groot aantal verschillende composities tussen het lamellaire en cilindrische gebied in het fasediagram. Dit is verrassend omdat de HPL morfologie normaliter een metastabiele fase is voor blokcopolymeren. Dit unieke fasegedrag komt voort uit

de aanwezigheid van PDP "zijketens" in het minderheidsblok van P4VP. Morfologiën met een gebogen grensvlak en het minderheidsblok (P4VP(PDP)) gelokaliseerd aan de holle kant (GYR en CYL) zijn namelijk niet stabiel, terwijl morfologiën met een recht of gebogen grensvlak en het minderheidsblok (P4VP(PDP)) gelokaliseerd aan de bolle kant (LAM en HPL) juist wel stabiel zijn.
Gyroïd complexen met verschillende dimensies, beschreven in hoofdstuk 3, worden gebruikt voor de fabricatie voor goedgeordende metallische nanoschuimen in hoofdstuk 5. Als onderdeel van de P4VP(PDP) gyroid matrix kan PDP compleet worden verwijderd met behulp van ethanol, met als resultaat een poreus polymeer netwerk met een porositeit lager dan 50 vol%. Met stroomloos plateren kan nikkel worden ingebracht door de gehele dikte van de film. Relatief grote nikkel kristallieten zijn zichtbaar met HR TEM in de poriën van de film. Het overgebleven polymeer wordt vervolgens verwijderd door pyrolyse. Het resultaat is een inverse gyroïd nikkel nanoschuim, met een goedgeordende structuur. De fysische eigenschappen zijn onderzocht met picoindentatie en ionenbundelbuiging door de Materiaalwetenschapsgroep van de Rijksuniversiteit Groningen. De actuator eigenschappen van het nanoschuim zullen worden bestudeerd in de toekomst. De katalytische eigenschappen van het inverse gyroïd nikkel nanoschuim worden onderzocht door het Centrum van Heterogene Katalyse en Duurzame Chemie van het Van 't Hoff Instituut voor Moleculaire Wetenschappen in Amsterdam. Het gebruik van poreuze gyroïd polymeer netwerken als membranen in batterijen wordt onderzocht door de Universiteit van Münster in Duitsland.

Acknowledgements

One chapter of my life is coming to an end and if I look back, I have to say I am very satisfied. There are a lot of people who have contributed to that and I hope I will not forget to mention any of you.

First of all, I would like to express my gratitude towards my supervisors Prof. Gerrit ten Brinke and Prof. Katja Loos for giving me the opportunity to become a part of their group. Gerrit, thank you for your support and freedom I had during my research that helped me to develop into an independent scientist. Your sharp mind and enormous energy are very inspiring. Katja, your door was always open for me and you were extremely supportive and interested in my research progress. Thank you for that! It was always a pleasure to spend time with you at a number of conferences. You are a source of positive energy and always ready to help to all members of the group.

Secondly, I would like to thank the members of the reading committee: Prof. Katarina Jeremić, Prof. Alexander Böker and Prof. Janne Ruokolainen, for the evaluation of my thesis and helpful comments. Katarina, thank you as well for motivating me to do my PhD studies in the Polymer Chemistry group in Groningen.

I am very grateful to Prof. Jeff Th. M. De Hosson and Prof. Patrick R. Onck for useful discussions we had during our monthly meetings. I owe special thanks to Sergey Punzhin for writing the appendix of chapter 5 and for providing beautiful SEM images. Eric Detsi, Siva Saane and Alex Zinchenko, thank you for your contributions during our monthly meetings.

I would like to acknowledge Dr. Marc Stuart for his assistance on TEM, Dr. JianCun Rao and Mikhail Dutka for HR TEM data collection and analysis, Dr. Heiner Friedrich from the Eindhoven University for providing the electron tomography data, Dr. Ryan Chiechi for allowing me access to the microtome in his lab and Dr. J. J. L. van der Walt for giving me access to the equipment at the

Molecular Imaging and Electron Microscopy department in UMCG. A part of the SAXS results from this thesis was acquired at the Dutch-Belgian beamline (ESRF, Grenoble, France). Therefore I would like to thank Dr. Wim Bras and in particular to Dr. Daniel Hermida Merino and Dr. Giuseppe Portale for their unselfish help during the measurements at any time, even on Sunday evenings. I am also grateful to Dr. Evgeny Polushkin for his help during the SAXS measurements in Grenoble. Panu Hiekkataipale from the Aalto University is acknowledged for his assistance during the SAXS measurements and especially for being a great host in Helsinki. Porosity measurements presented in this thesis were performed under the guidance of Dr. Zorica Vuković from the Institute of Chemistry, Technology and Metallurgy (ICTM), Center for Catalysis and Chemical Engineering, University of Belgrade (financed by Ministry of Education, Science and Technological Development, Project No. III 45001), which field of expertize is determination and interpretation of porous structure. Thus I would like to express my great appreciation to Dr. Zorica Vuković for performing all the measurements and for useful discussions. I am grateful to Gert Alberda van Ekenstein for his assistance with DSC and TGA and for his valuable advices. I owe special thanks to Dr. Walter Dressick from the U.S. Naval Research Laboratory in Washington, DC for his advices considering electroless plating. I admire your tremendous knowledge and kindness. I would also like to acknowledge Nikola Davidović for designing the cover of this thesis.

I am also very grateful to Thomas Voortman for his contribution as a Master student, especially to chapter 3 of this thesis. Part of his work was published in Macromolecules in 2012 (Volume 45, pages 3503-3512). Thomas, it was a great and sometimes challenging experience to work together and I have learned a lot from it. Good luck with your PhD!

It was a pleasure having nice colleagues at the Polymer Chemistry department. Thank you for the relaxed working atmosphere, all borrels, barbecues and trips we had together. Special thanks to my darling Vincent Voet for being a fantastic colleague, for teaching me anionic polymerization, for a great time in Helsinki, Bayreuth, Girona, Grenoble, etc., for proof reading my manuscripts and translating the summary to Dutch, for helping me with NT2 and many other things. Vinnie, your enthusiasm about science is very motivating. Anton, Martin and Niels, I enjoyed being a part of the block copolymer team and I will always remember the great time we had in Grenoble. Jakob, thanks for being a great officemate. You are considerate but very straightforward which I appreciate a lot and I enjoyed very much our conversations. Ralph, my part-time office mate, it is great to have you as

a colleague and a friend. Wouter, thanks for your kindness, patience while teaching me windsurfing and Dutch and for many funny moments we had together. Gerrit Gobius, thanks for helping me at the beginning of my PhD studies. Your thesis was a valuable book to me! Nemanja, you helped me to start a new life in Groningen and you motivated me to run, hvala, doktore! In a random order I would like to thank you all for great time during and after work: Danijela, Albert, Kamlesh, Guiseppe, Laura, Vladimir, Zheng, Salomeh, Erythrina, Rachma, Lia, Quiyan, Yi, Joop, Mark, Martijn, Patrick, Nienke, Agnieszka, Jan Willem, Deepak, Minseok, Pavlo, Alessio, Diego, Alina, Kai, Steven, Nanda, Lieuwe Jan, Leendart, Jeroen, Wendy and all the others I forgot to mention here. Prof. Arend Jan Schouten, Prof. Ton Loontjens and Prof. Andreas Herrmann, thank you for keeping nice working atmosphere. Karin and Yvonne, many thanks for your help in administrative matters.

I am very grateful to my flatmates, colleagues, paranymphs and friends Jelena and Milica. Last four years we shared everything, laughs and tears, made parties, dinners, we travelled together and we were there for each other in good and bad. Jelena, you became like a sister to me! I would like to thank you for your care and love. Being such a strong, diligent, determined, energetic and lovable person, I believe you will be successful in every field of your life. Milice, thank you for being a great friend and for spreading positive energy! That beautiful smile will be adored everywhere (including Columbia!). My ladies, I wish you the best of luck!

Next, I would like to thank to our big Groningen family for their friendship, support and all the fun we had: Cobe, Višnja, Goća, Milica, Jelena, Vibor, Kaća, Dule, Jelena, Deki, Sonja, Igor, Ana, Primzi.

I would like to offer my special thanks to Radovan Vukićević for his love, limitless support and friendship. Radovane, thank you for correcting my manuscripts, for your constructive criticism and for being there for me always! Niko, niko kao Radovan!

My dear friends in Serbia: cilka Jelena, Jela Petronka, kuma Jovana, Miličica, Bašo and Feđa, thank you for your support and great time we spent together!

Dear Milena and Anita, you accepted me in your family with your arms and heart wide opened. Milena, hvala na fantastičnim večerama (posebno kolačima!), na biciklima i na brizi o meni/nama u svakom pogledu.

I am deeply grateful to my family: my sister Goga with her husband Bato and their sons Petar and Jovan, my aunt Anđa and my dear parents Jeka and Marko. Dragi moji, puno vas volim i hvala vam na bezgraničnoj ljubavi i podršci sve ove godine.

Finally, I would like to acknowledge one special person that is for sure the most responsible for my happiness in the last two years. Dear Ivan, thank you for being next to my side, for your support and encouragement. It is great that you could listen and learn (you even showed interest, I hope) about polymer science, especially about the famous PS-b-P4VP(PDP). I've learned a lot from you and thank you for that, and especially thanks for countless times you made me laugh. Ivanče, ti si naj sasvim potpuno sasvim najbolji dasa i ja te obožavam!